Doctoral Dissertation

Study on mesogenic-phthalocyanine-based bulk heterojunction solar cells with donor-acceptor phase-separated structures

液晶性フタロシアニンを用いたドナー―アセプタ相分離構造を有するバルクヘテロ接合太陽電池に関する研究

Quang-Duy Dao

January 2014

Graduate School of Engineering,
Osaka University

Abstract

A study on photovoltaic properties of octaalkylphthalocyanine ($CnPcH_2$)-based bulk heterojunction (BHJ) organic solar cells (OSCs) with donor and acceptor phase-separated structures is reported. The effects of processing additives on the donor and acceptor phase separation and crystallization of BHJ materials are investigated and the high photovoltaic performances of the OSCs are achieved with the optimum donor and acceptor phase separation and crystallization of BHJ materials. Furthermore, the optical and electronic properties, structures, and stability of $CnPcH_2$ are evaluated.

Chapter 1: Introduction

The purpose and overview of the dissertation is given. The general background of BHJ OSCs and their mechanism are also introduced. The fundamental properties, such as the optical and electronic properties, of mesogenic-phthalocyanine are briefly described.

Chapter 2: Effects of processing additives on donor and acceptor phase separation, crystallization and photovoltaic performances of solar cells

Studies on the effects of processing additives on the donor and acceptor phase separation, crystallization, and photovoltaic performance of BHJ OSCs made of 1,4,8,11,15,18,22,25-octahexylphthalocyanine ($C6PcH_2$) and [6,6]-phenyl-C_{61} butyric acid methyl ester ([60]PCBM) via spin-casting are reported. By incorporating various solvents as processing additives to a volume of a few percent, the separation of donor and acceptor phases in $C6PcH_2$:[60]PCBM thin films, which is discussed by taking the photoluminescence (PL) quenching, Davydov splitting at the Q-band of the absorbance spectra and the surface nanomorphology into consideration, is promoted, and the crystallinity of the discotic $C6PcH_2$ molecules with hexagonal structures is reinforced. The BHJ OSCs with the optimum phase-separated BHJ materials and high crystallinity of the discotic $C6PcH_2$ molecules demonstrate the high power conversion efficiency (PCE) of 4.2%.

Chapter 3: Roles of fullerene in photovoltaic properties of solar cells

The $C6PcH_2$:[60]PCBM-based BHJ OSCs demonstrated the relatively high PCE of 4.2%, and the external quantum efficiency (EQE) at Q band of phthalocyanine close to 60%, by utilizing

processing additives. However, the EQE at around 500 nm was limited due to the low absorption of both $C6PcH_2$ and [60]PCBM. By using asymmetric fullerene derivatives, [6,6]-phenyl-C_{71} butyric acid methyl ester ([70]PCBM), the EQE of the OSCs at around 500 nm is improved from 8% to 24%, and the short-circuit current density increases from 8.1 to 10.2 mA/cm^2. An open-circuit voltage of 0.96 V is achieved by a using fullerene derivative with a high lowest unoccupied molecular orbital. Furthermore, the effects of blend ratios on the photovoltaic properties of BHJ OSCs utilizing $C6PcH_2$ were also discussed.

Chapter 4: Alkyl substituent length dependence of photovoltaic performance of solar cells

Alkyl substituent length dependences of photovoltaic performance of BHJ OSCs utilizing $CnPcH_2$ mixed in [70]PCBM are studied. By shortening the alkyl substituents, stacking of the discotic $CnPcH_2$ columns is probably changed from 2-D rectangular lattices to pseudohexagonal structures, and Davydov splitting at the Q-band of $CnPcH_2$ absorbance spectra decreases, which results in the balance of hole and electron mobilities and the deeper highest occupied molecular orbital energy levels. As a result, the photovoltaic performance of $CnPcH_2$-based BHJ OSCs is improved by shortening the alky substituent length.

Chapter 5: Mechanism of degradation and improvement of stability on mesogenic-phthalocyanine-based solar cells

Mechanism of degradation and improvement of stability on mesogenic-phthalocyanine-based solar cells are studied. $C6PcH_2$-based cells demonstrate higher stability than the cells fabricated using poly(3-hexylthiophene) without any ambient dependence. Furthermore, one found that the chemical bonds of two pyrrole aza nitrogens as well as the four mesobridging aza nitrogens with neighboring carbons in the $C6PcH_2$ molecule are broken after irradiation with a solar simulator, which affected the device lifetime. On the other hand, the C_{60} thin films and the oxidized layers play an important role as blocking layers that prevent the diffusion of metal atoms into the active layer, resulting in the higher stability.

Chapter 6: Conclusion

The obtained results are summarized and the main conclusions are drawn.

***** ***** ***** ***** *****

Contents

Chapter 1

Introduction

With the recent rise in the awareness of environmental issues, renewable energy sources have attracted considerable attention. In terms of photovoltaics, since the discovery of photoluminescence (PL) quenching, photoinduced charge transfer, and photoconduction enhancement in π-conjugated polymer-fullerene composite systems, bulk-heterojunction (BHJ) organic solar cells (OSCs) have been considered to be promising candidates for a light weight, flexible, large-area, low-cost, and renewable energy source [1-4]. Furthermore, a combination of material design, morphology control, structural insight, and device engineering has led to high-photovoltaic-performance BHJ OSCs with power conversion efficiencies (PCEs) reaching the 6–10% range [5, 6].

In terms of material design, donor materials are classified into two major groups: polymer and small-molecule-based semiconductors. Despite the high PCE reported for polymer BHJ OSCs, one found that for a given polymer structure, batch-to-batch variations in solubility, molecular weight, polydispersity, and purity can lead to the different processing properties and performance [7]. On the other hand, active layers in solution-processed small-molecule BHJ OSCs consist of well-defined molecules of intermediate dimensions. The higher molecular precision, relative to the statistically determined nature of synthetic polymers, can circumvent the aforementioned batch-to-batch variations. More reproducible fabrication protocols and a better understanding of molecular structure-property relationships are therefore anticipated.

Liquid crystals have been demonstrated as a novel type of small-molecule semiconductors for solution-processed BHJ OSCs [8-10]. In general, typical structures of mesogenic molecules are of ‘‘rodlike’’ and ‘‘disklike’’ types, which are known as calamitic and discotic liquid crystals, respectively. For discotic liquid crystals, the mesogenic molecule consists of a rigid core with a π-electronic conjugation system and alkyl substituents at peripheral or nonperipheral positions. While the core parts play an important role in electronic conduction, the flexible parts definitively attribute the self-assembling nature. In addition, the flexible parts have made such alkylated π-electronic conjugation systems much more attractive for ‘‘wet processing’’ thin-film devices due to their good solubility in common organic solvents. Recently, we have demonstrated high hole and electron drift mobilities in the crystalline phase of a mesogenic phthalocyanine derivative, 1,4,8,11,15,18,22,25-octahexylphthalocyanine ($C6PcH_2$) [9]. Moreover, $C6PcH_2$ exhibits not only

excellent processability in the form of thin films but also appropriate electronic characteristics for OSCs, such as a deep highest occupied molecular orbital (HOMO) energy level, a relatively small band gap, and strong optical absorption. Despite these attractive characteristics, OSCs with an active layer composed of $C6PcH_2$ mixed with [6,6]-phenyl-C_{61} butyric acid methyl ester ([60]PCBM) showed the relatively low PCEs owing to poor BHJ-separated phases and the low external quantum efficiency (EQE) at around 500 nm [10].

In this dissertation, we mainly focused on investigating effects of processing additives and blend ratios on nanoscale phase separation, crystallization and photovoltaic performances of BHJ OSC utilizing $C6PcH_2$. Furthermore, the alkyl substituent length dependence of the photovoltaic performances of the OSCs was investigated, and the low EQE at around 500 nm was improved by employing asymmetric [6,6]-phenyl-C_{71} butyric acid methyl ester ([70]PCBM). Otherwise, the mechanism of degradation and the stability of the BHJ OSCs were studied.

The outline of this dissertation is as follows. The remainder of this chapter will be assigned to introduce the fundamental concepts used in this dissertation: namely they are categorization of the solar cell technologies, photovoltaic principles, and properties and application of phthalocyanine. Chapter 2 devotes to investigate the effects of processing additives on the donor and acceptor phase separation, crystallization, and photovoltaic performance of the BHJ OSCs utilized discotic $C6PcH_2$ mixed with [60]PCBM. The BHJ OSCs with the optimum donor and acceptor phase separation and crystallization of the BHJ materials, achieved by adding 0.2% v/v of DIO to the BHJ blend solution, exhibited the high PCE of 4.2%. By using the optimum donor and acceptor phase separation and crystallization of the BHJ materials, the roles of fullerene derivatives in the photovoltaic properties of the BHJ OSCs utilizing $C6PcH_2$ and the dependences of optical and electronic properties, structures, and photovoltaic performance of BHJ OSCs utilizing $CnPcH_2$ mixed [70]PCBM on the length of alkyl substituents will be investigated in chapters 3 and 4, respectively. In chapter 5, the high stability as well as the mechanism of degradation of $C6PcH_2$:[60]PCBM BHJ OSCs will be discussed. The main results obtained in each chapter will be summarized in chapter 6 and future prospects will be discussed.

1.1 Solar cell

New power generation and storage equipment, ranging from batteries to power plants, must be continually developed and manufactured to meet the ever increasing demand for electrical power around the globe for a wide variety of applications. Solar cells have the ability to meet some of these power demands by directly converting sunlight into electricity and can potentially generate power anywhere there is light. Since, Alexandre-Edmond Becquerel first observed the photovoltaic effect in an electrolyte solution in 1839 and the modern era of solid-state solar cells was ushered in with developments at Bell Labs in 1954, numerous solar cell technologies were developed at this point [11, 12]. In this dissertation, we will focus on the understanding and development of one of these technologies, organic solar cells.

1.2 Current solar cell technologies

Many solar technologies exist with varying degrees of development, and organic solar cells are one of the newer classes of these technologies. This section will briefly discuss the main solar cell technologies at present to help put the role of organics in context. The most commercially available solar cell technologies can be divided into two main groups: crystalline and multicrystalline silicon and inorganic thin films. After these two main groups, there are several emerging technologies that have not yet seen broad commercial availability but still been heavily investigated in the laboratory for future application, including GaAs, concentrator, dye-sensitized, and organic thin-film solar cells.

Solar cells based on crystalline and multicrystalline silicon are by far the most developed and produced of all the solar cell technologies. The development of silicon solar cells greatly benefited from the large-scale effort to understand and process silicon as a semiconductor for electronics and integrated circuits. In silicon solar cells, a photon is absorbed to generate a free hole and electron that are separated and collected to generate current [11]. PCEs, which define the percent of incoming light power converted into electrical power, up to 25% and 20.4% have been demonstrated in crystalline and multicrystalline silicon solar cells, respectively [13]. While silicon is by far the leading solar cell technology, there are still many areas for improvement either with advances in silicon or with other material systems. First, high-purity silicon is generally expensive and slow to grow. Because silicon is an indirect band-gap semiconductor and has a weaker absorption compared to other semiconductors, thicker layers of silicon are generally required compared to other materials [12]. For these and other reasons, the silicon alone accounts for nearly 50% of the cost of a completed solar module. To circumvent some of these limitations and potentially achieve lower costs

per produced power, technologies are also being developed that can use less material either by having thinner active layers based on thin films or smaller active layers with light from a large area concentrated onto the small cell.

Inorganic thin-film solar cells are the basis for nearly all of the presently available commercial solar cells that are not based on crystalline and multicrystalline silicon. Inorganic thin-film solar cells attempt to reduce the expensive cost of wafers in silicon cells by using thin films of semiconductors that are usually deposited onto a supporting substrate. The active layers are only a few microns thick but can still absorb significant amounts of light because of strong absorption in the materials. More impurities in the semiconductors can be tolerated since charges have a shorter distance to travel through the thin films [12]. Deposition and processing of thin-film materials also uses lower temperatures compared to silicon. Lower active material volume, purity, and processing temperatures can all lead to lower cost per area for thin-film solar cells, though it generally comes with a tradeoff of efficiency relative to crystalline and monocrystalline silicon. The net effect is a cost per Watt that is competitive with silicon. The leading material platforms for inorganic thin-film cells are amorphous silicon (a-Si), $Cu(InGa)Se_2$ (CIGS), and CdTe with highest efficiencies of 10.1%, 19.6%, and 19.6%, respectively [13].

Numerous other solar cell technologies exist that are still not widely available commercially. The highest efficiencies have been demonstrated in cells based on GaAs for both single and multijunction devices. Multijunction solar cells use multiple layers that are tailored to more efficiently convert different portions of the solar spectrum based on the band gap of the layers. However, GaAs solar cells have generally been limited to space applications because of their higher cost [12]. The high cost of high efficiency cells can potentially be offset by concentrating a large area of sunlight onto a solar cell with a small area. Concentration can produce a large amount of power with only a small amount of semiconductor. Furthermore, higher efficiencies can be obtained under concentrated light compared to the standard one sun illumination [14]. Efficiencies of 44% have been obtained in multijunction solar cells under concentrated sunlight [13].

Two other technologies that have been garnering significant attention are based on organic materials. Dye-sensitized solar cells use an organic dye coating a porous electrode with large surface area to absorb light. Efficiencies of up to 11.9% have been achieved for dye-sensitized solar cells [13]. Another organic technology is thin-film solar cells based on solid-state organic semiconductors. Organic semiconductors can have their chemical and electrical properties tailored in numerous ways by modifying the chemical structures and can allow for new processing methods. Organics have great potential for light-weight, flexible devices fabricated with high-throughput processes from

low-cost materials in a variety of colors. Although organic semiconductors are still a relatively young field, the high PCEs of 10.7% are achieved [13].

1.3 Organic solar cells

Thin-film solar cells based on organic semiconductors are interesting for several reasons. Firstly, the electrical and chemical properties of organic semiconductors can be tailored by modifying the chemical structure of the compounds in endless combinations. Though specific design rules are still under investigation, the potential for tailoring molecules to different applications is great. Furthermore, the organic molecules have the potential to be cheaply synthesized without significant concern on the limit of raw materials. Next, organic semiconductors can be deposited in a number of low-temperature and high-throughput ways, such as evaporation and solution processing, that can lower manufacturing costs. Because organic materials can have high absorption coefficients, a layer of only a few hundred nanometers is often enough to absorb a large fraction of light in the material's absorption spectrum. The use of such thin layers reduces the amount of active material needed and also makes light-weight and flexible devices possible. For these and other reasons, OSCs have gained significant attention.

The first modern solid-state solar cell based on organic materials with a PCE close to or higher than 1% was developed by C. W. Tang during his time at Eastman Kodak [15]. Tang stacked a layer of copper phthalocyanine that donates electrons, or a donor, and a layer of perylene tetracarboxylic derivative that accepts electrons, or an acceptor, between the electrodes. When a photon is absorbed in an organic material, a bound electron-hole pair, called an exciton, is created and must be dissociated to contribute to the current. This architecture is commonly referred to as a planar heterojunction because the deposited layers can be idealized as stacked planes of different materials, as shown in Fig. 1.1(a). Vacuum thermal evaporation is the most common method of depositing the organic layers for planar-heterojunction devices. The exciton diffusion length is the average distance that an exciton travels before recombining and is critical in planar-heterojunction devices because a photogenerated exciton must travel a distance to the interface of donor and acceptor to be separated into a hole and electron. The short exciton diffusion lengths in most organic materials (on the order of tens of nanometers) limit the thickness of the organic layers. While thick layers are desired for high absorption, layers must also be sufficiently thin to prevent the excessive recombination because of the short exciton diffusion lengths.

To overcome some limitations by the small exciton diffusion length, the donor and acceptor layers can be blended together to minimize the distance, since an exciton must travel to reach the

interface of donor and acceptor. This structure is called a bulk heterojunctions since the heterojunction is dispersed throughout the bulk of the layer, as shown in Fig. 1.1(b). Hiramoto *et al.* first demonstrated the BHJ structure with a co-deposited layer of metal-free phthalocyanine (as donor) and a perylene tetracarboxylic derivative (as acceptor) between neat layers of the donor and acceptor [16].

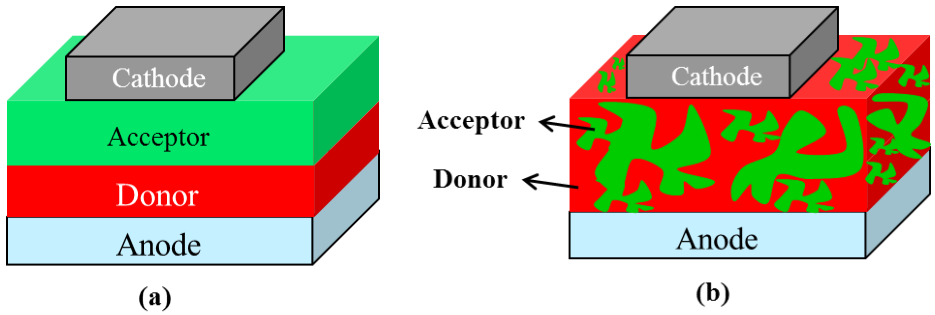

Fig. 1.1. Schematics of the basic structures for (a) planar-heterojunction OSCs and (a) BHJ OSCs.

Bulk heterojunctions also helped facilitate the transition to solution processing of the organic layers. Solution processing is attractive, because it might be more easily applied to large-scale, high-speed manufacturing processes, such as printing, compared to vacuum processing. The first solution-processed organic solar cells incorporating a blend for the active layer were demonstrated by blending the polymers MEH-PPV and cyano-PPV as donor and acceptor, respectively [17, 18]. The natural phase segregation of polymer blends was expected to create pathways to enhance carrier transport, and the work functions of the electrodes are thought to determine the extracted carrier type [17, 18]. Yu et al. showed that the acceptor polymer could be replaced with a soluble derivative of [60]PCBM, to yield devices with PCEs up to ~1.5% under low-intensity broadband illumination [4]. Much effort has been made of exploring new polymers and acceptors for BHJ OSCs to increase absorption and carrier transport. One of the most researched combinations to date is poly(3-hexylthiophene) (P3HT) blended with [60]PCBM, which reaches PCEs close to 5% [19, 20]. Recently, new donors with the absorption spectra that extend farther into the red part of the spectrum have been reported in blends with [70]PCBM yielding efficiencies greater than 5% [19].

The phase segregation in the composite thin films has become apparent as a major factor influencing overall device efficiency. Annealing of devices, changing the solvent and the drying speed of the film, and adding chemicals with selective solubility of the fullerene component to affect crystallization have been found to affect the phase segregation and the improvement of photovoltaic performance [19-21]. However, finding the optimum conditions can be very tedious and time

consuming. Researchers are taking advantage of the ability to solution process by demonstrating cells fabricated by various methods, such as screen printing, inkjet printing, gravure printing, brush painting, and even roll-to-roll printing [22-26].

1.4 Photovoltaic principles

This section will cover the basic electrical characteristics common to all solar cells. When measured in the dark, the current density–voltage (*J*–*V*) characteristics of most efficient inorganic and organic solar cells resemble the exponential response of a diode with high current in forward bias and small current in reverse bias. Under illumination, the device generates a photocurrent in the cell in addition to the diode behavior, and the *J*-*V* characteristic is ideally the superposition of the dark characteristic and the photocurrent. The *J*–*V* characteristics of an ideal device can be described by the Shockley equation with an additional photocurrent term, J_{ph}

$$J = J_0 \left[\exp\left(\frac{eV}{nkT}\right) - 1\right] - J_{ph} \tag{1.1}$$

where *J* is the current density, *V* is the applied voltage, J_0 is the reverse saturation current density of the diode, *e* is the elementary charge, *n* is the ideality factor, *k* is the Boltzmann constant, and *T* is temperature [27]. In reality, the photocurrent will have a dependence on applied voltage, and the illumination can affect the characteristics of the diode.

Figure 1.2 depicts the *J*-*V* plot for a solar cell in the region of power generation. Power density, the product of voltage and current density, versus voltage is also plotted, and negative power indicates power generation. The most discussed performance parameters that can be found from the *J*-*V* curve of a device under a known illumination source are open-circuit voltage (V_{oc}), short-circuit current density (J_{sc}), fill factor (*FF*), and PCE (or η).

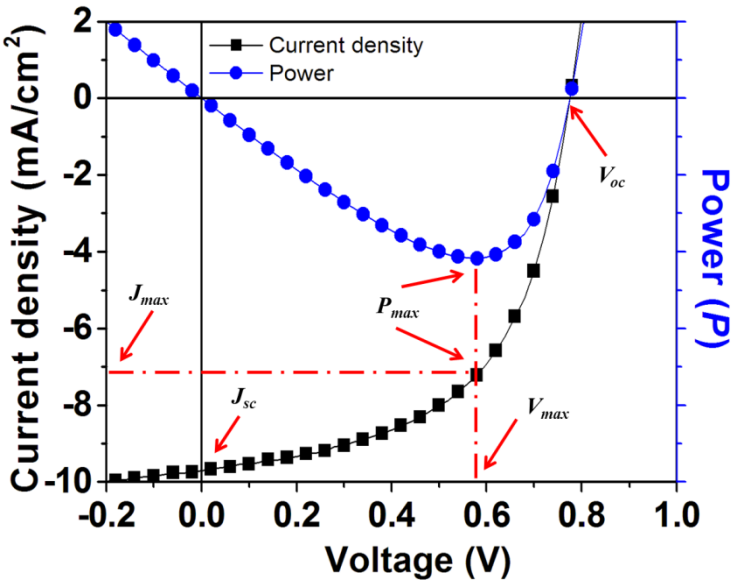

Fig. 1.2. Graphs of power and current density as a function of voltage for a solar cell along with parameters.

1.4.1 Open-circuit voltage

V_{oc} is the voltage across the solar cell when J = 0, which is the same as the device being open-circuited. Because J = 0 and power is the product of current and voltage, no power is actually produced at this voltage. However, the V_{oc} marks the boundary for voltages at which power can be produced. The V_{oc} can also be thought of as the point at which the photocurrent generation and dark current processes compensate one another.

1.4.2 Short-circuit current

J_{sc} is the current density when V = 0, which is the same conditions as the two electrodes of the cell being short-circuited together. Again, there is no power produced at this point, but the J_{sc} does mark the onset of power generation. In ideal devices, the J_{sc} will be the same as the photocurrent density J_{ph}. Although J_{sc} is technically a negative number with the conventions used here, discussions of different J_{sc} values will focus primarily on the magnitude of the value and treat it as a positive number, *e.g.*, a higher J_{sc} corresponds to a higher J_{ph}.

1.4.3 Fill-factor

While V_{oc} and J_{sc} mark the boundaries of power production in a solar cell, the maximum power density produced P_{max} occurs at the voltage V_{max} and current-density J_{max} where the product of J and

V is at a minimum (or maximum in absolute value), as shown in Fig. 1.2. Because of the diode behavior and additional resistance and recombination losses, $|J_{max}|$ and V_{max} are always less than $|J_{sc}|$ and V_{oc}, respectively. The fill factor FF describes these differences and is defined as

$$\mathrm{FF} = \frac{J_{max} \times V_{max}}{J_{sc} \times V_{oc}} \tag{1.2}$$

FF is an indication of how close J_{max} and V_{max} come to the boundaries of power production of J_{sc} and V_{oc}, and also an indication of the sharpness of the bend in the exponential *J-V* curve that connects J_{sc} and V_{oc}. Since higher *FF* is related to higher maximum power, high *FF* is desired; however, the diode-like behavior of solar cells results in *FF* always being less than one. Devices with high $|J_{sc}|$ and V_{oc} can still have low *FF*, suggesting that something must be done to improve device quality.

1.4.4 Power conversion efficiency

The most discussed performance parameter of a solar cell is the PCE, and is defined as the percentage of incident irradiance I_L (light power per unit area) that is converted into output power. Because the point where the cell operates on the *J-V* curve changes depending on the load, the output power depends on the load. For consistency, the maximum output power is used for calculating efficiency. In equation form, the PCE, η is written

$$\eta = \frac{|J_{max}| \times V_{max}}{I_L} \times 100\% = \frac{FF \times |J_{sc}| \times V_{oc}}{I_L} \times 100\% \tag{1.3}$$

This form clearly shows that FF, J_{sc}, and V_{oc} all have direct effects on PCE. Furthermore, the area used to calculate *J* can affect PCE and should include inactive areas that are integral to the solar cell, such as grids and interconnects, when calculating efficiency for large area devices or modules.

PCE is important since it determines how effectively the space occupied by a solar cell is being used and how much area must be covered with solar cells to produce a given amount of power. Since larger areas require more resources to cover with solar cells, higher PCE is often desirable. However, there are tradeoffs between PCE and cost for each solar cell technology that must be balanced.

PCE is also very dependent on the power and spectrum of the light source since solar cells do not absorb and convert photons to electrons at all wavelengths with the same efficiency. To draw comparisons between various solar cells, a standard spectrum must be chosen for the calculation of PCE. Although the spectrum of the sunlight at the earth's surface varies with location, cloud coverage, and other factors, the AM1.5 G spectrum in Fig. 1.3 is the most commonly used standard spectrum for measuring and comparing the photovoltaic performance that are intended for outdoor use. Because of difficulties recreating this exact spectrum in the laboratory with standard lamps, PCE

measurements must often be corrected based on the EQE.

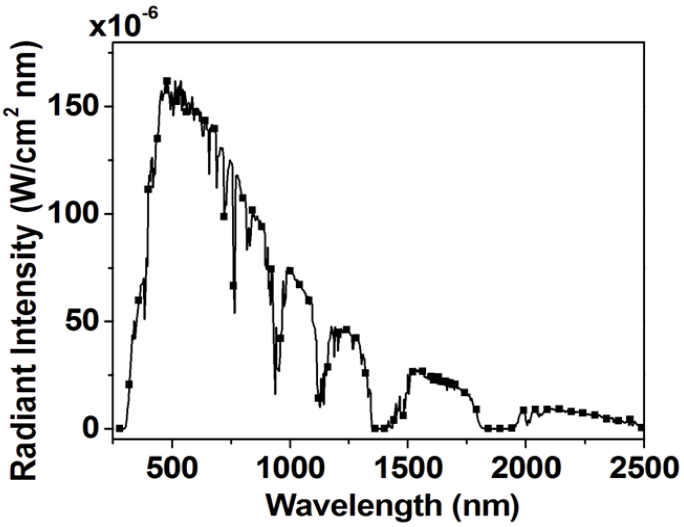

Fig. 1.3. Solar radiant spectra (AM1.5, 100 mW/cm^2).

1.4.5 External quantum efficiency

EQE of a device is the fraction of incident photons converted into current and depends on wavelength. One reason for the wavelength dependence is that the absorption in the active layers is a function of wavelength. Another reason, especially in inorganic solar cells, is that the location where a photon is absorbed in a device can also affect the probability of the resulting charges being collected or being lost.

J_{sc} can be estimated from the EQE and the spectral irradiance of the light source by integrating the product of the EQE and the photon flux density. For the standard AM1.5 G spectrum, the calculation is

$$J_{sc} = \int_0^\infty eEQE(\lambda)\frac{\lambda}{hc}E_\lambda^{AM1.5G}(\lambda)d\lambda \qquad (1.4)$$

where $E_\lambda^{AM1.5G}$ is the spectral irradiance of the AM1.5 G spectrum, λ is the wavelength, h is Planck's constant, c is the speed of light, and e is the elementary charge. If the EQE was measured at low light intensities, then this calculation will only be accurate if the J_{sc} is a linear function of irradiance, as is expected for ideal devices. Otherwise, EQE must be measured with a dc bias light source that generates a photocurrent in the device similar to what is expected under AM1.5 G.

1.5 Introduction to phthalocyanine: Properties and application

Phthalocyanines possess great chemical and thermal stability, with the unsubstituted derivatives

being able to withstand temperatures of up to ca. 400 ºC without decomposing and are also resistant to strong acid and alkaline conditions [28]. These main properties rendered phthalocyanines as popular pigments and colourants [28]. They are very versatile compounds and most of their applications derive from the exploitation of their molecular and bulk properties. A more detailed description of the properties relevant to this project will be discussed.

1.5.1 Optical properties

Phthalocyanines are widely known for their intense blue-green colour as a result of the aromatic 18 π-electron system which they possess. The extended conjugation in the ring produces low energy π-π* transitions which are detected in two main regions of the UV-Vis spectrum. These are denominated Q and Soret bands (or B band), with the main absorption occurring in the Q-band region. Metallated phthalocyanines exhibit a characteristic single Q-band which appears in the red/near-infrared region of the spectrum (670-720 nm) giving the phthalocyanines their characteristic blue/green colour. Metal-free phthalocyanines are usually characterised on the other hand by a split Q-band signal, arising from the reduced symmetry in the molecular structure compared to the metallated phthalocyanines (D_{2h} for metal-free phthalocyanines and D_{4h} for the metallated phthalocyanines). The split signals are usually designated as Q_x and Q_y. Vibrational overtones can also be detected in the visible region and appear as minor absorptions near the main Q band.

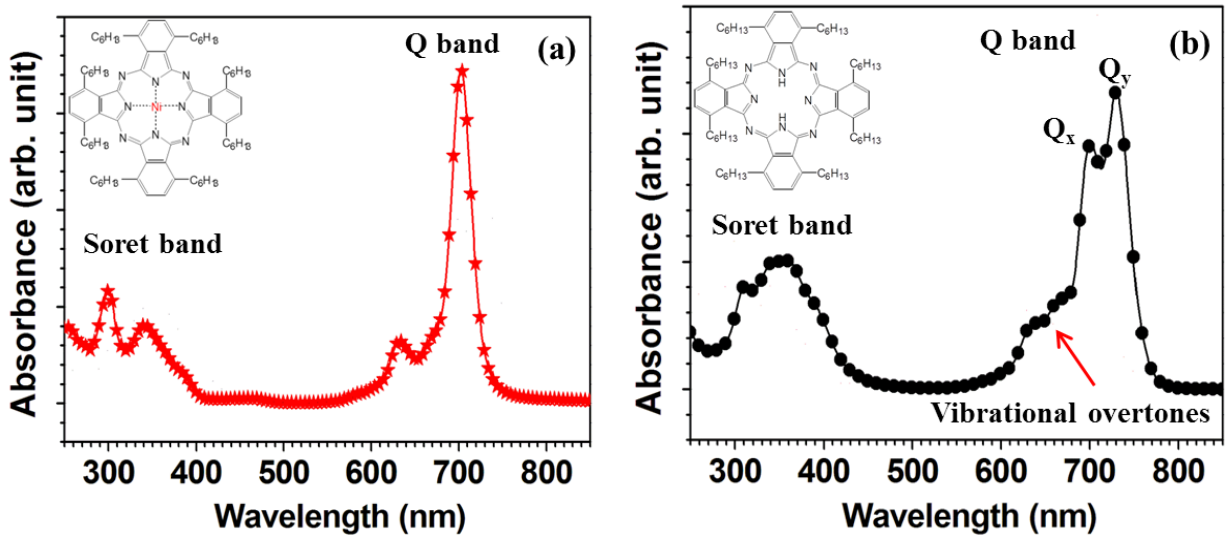

Fig. 1.4. Absorbance spectra of (a) metallated phthalocyanines and (b) metal-free phthalocyanines in solution.

The molar extinction coefficient of these compounds is also uniquely high, rendering them ideal compounds for inks and dyes [29]. Their first use after their discovery was as blue and green

light-resistant pigments and dyes in the paper and textile industries because of their high thermal, chemical, and photochemical stabilities [30]. Currently they are still being manufactured worldwide on a large scale as inks, textile dyes, and plastic colorants provide the basis for most blue-green paints in the automotive industry [28].

The absorption peak in the Q-band region can undergo a bathochromic or hyspochromic shift due to several factors such as the metal ion inserted into the cavity of the phthalocyanine, the addition of substituents at peripheral or non-peripheral positions of the molecule and the type of solvent used. The insertion of a metal in the phthalocyanine macrocycle may result in an excitation transfer between the metal's d-orbitals and the phthalocyanine ligands [31].

On the other hand, the structural modifications in the macrocycle are the main contributors that give rise to the wide range of colours of phthalocyanines that have been synthesised up until now [29, 32]. The functionalization of the phthalocyanine periphery usually produces a bathochromic shift of the Q-band with respect to the Q-band of the unsubstituted phthalocyanine, with the peripheral and non-peripheral positions having different effects [33]. Different substituents also affect the degree of shifting, due to electron-donating effects raising the energy levels of the HOMO orbitals. Also, by extending the π-system, it is even possible to induce a shift of the Q-band well into the near-IR region [33, 34].

Historically, phthalocyanines found themselves known primarily as materials that excelled as dyes and pigments due to their optical properties but their use was limited due to their poor solubility. Once the chemistry of phthalocyanines evolved, it was possible to functionalize these materials to give organic-solvent soluble derivatives that enable exploitation of their other properties and expand the scope of their applications into the novel field of optoelectronics.

The intense absorption in the visible region, the Q band, results from the a_{1u}-e_g, π-π* transition, generating an orbitally doubly degenerate state, ^1E_u, in metal phthalocyanines of D_{4h} symmetry. In the metal-free phthalocyanines, the symmetry is lowered to D_{2h} and the excited state is split into two components usually termed Q_x and Q_y. These then are the two principal 670-720-nm-region absorptions in the mononuclear species.

The theory of interaction between phthalocyanine and between porphyrin molecules has been discussed in the literature, especially in the context of cofacial diporphyrins and chlorophyll dimers, aggregated porphyrins, and oxo-bridged porphyrins, and is generally based on exciton coupling [35].

The exciton coupling is proportional to the magnitudes of the transition moments, inversely proportional to the cube of their separation, and has angular dependence. In D_{4h} symmetry, two pairs of doubly degenerate states will then arise, with transitions to the two upper, in-phase coupled states

allowed (these will be blue-shifted relative to the mononuclear case), and transitions to the lower out-of-phase combinations being forbidden. In the D_{2h} symmetry of the metal-free derivatives, the Q_x and Q_y states will split and the coupling will result in a pair of nondegenerate in-phase higher energy combinations (Q_{y+},Q_{x+}) and a pair of lower energy outof-phase combinations (Q_{y-},Q_{x-}) (Fig. 1.5). This theory specifically precludes any overlap between the molecular orbitals of each component. The ground state of the binuclear system corresponds with that of the mononuclear unit but may be stabilized by van der Waals's interaction energy.

In the low symmetry of the real binuclear molecules (tilted and slipped conformations etc.), transitions to both the higher and the lower energy combinations can be expected, yielding intensity both blue- and redshifted with respect to the mononuclear case. A range of energies is anticipated for the in-phase and out-of-phase combinations, arising from the various conformations. At room temperature a Franck-Condon electronic excitation will see a summation of all the dynamic conformations which exist in solution. Without discussing the added complexities of solvent effects varying from mononuclear to binuclear species, a broad absorption is predicted, shifted to the blue of the mononuclear absorption and possessing a broad weak tail to the red. Superimposed on this envelope will be the two *Q* peaks of species in which the two halves of the molecule are sufficiently uncoupled to be regarded simply as two independent mononuclear species tied together.

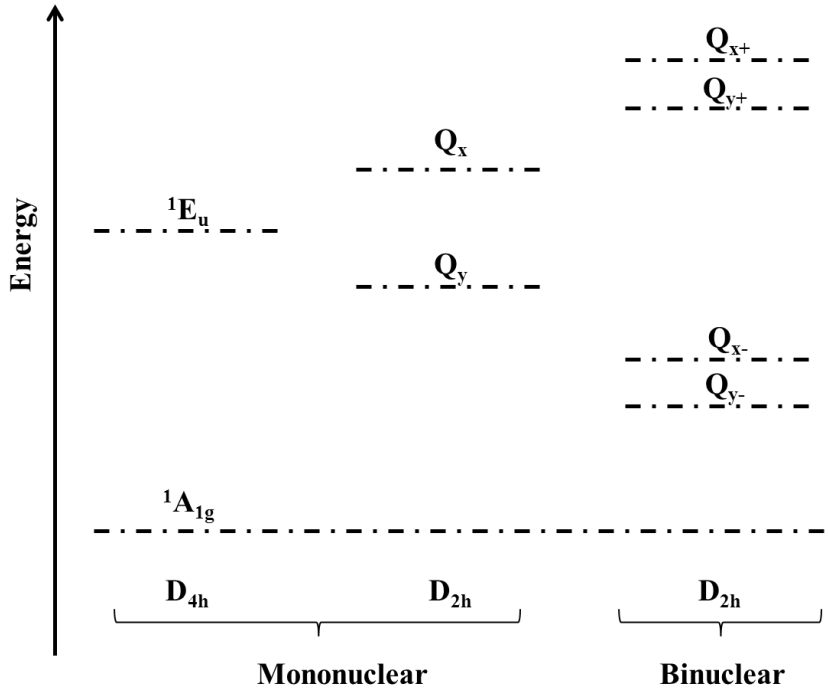

Fig. 1.5. A qualitative orbital energy diagram for exciton coupling.

1.5.2 Semiconductive properties

A semiconductor can be defined as a material that presents electrical conductivity due to either electron flow or "hole" transfer at a magnitude between that of a conductive and an insulating material. This conductivity is roughly established between 10^3 and 10^{-8} S/cm. In simple terms, the conductivity present in these materials arises from the transfer of electrons across the electronic structure of the materials. In a conductive material the electron transfer occurs when the electrons are excited from the ground-state valence band to the conduction band. The energy needed to provide this excitation depends on the energy gap present between these two bands. The size of this gap, as shown in Fig. 1.6, is what determines if a material is a conductor, semiconductor or insulator.

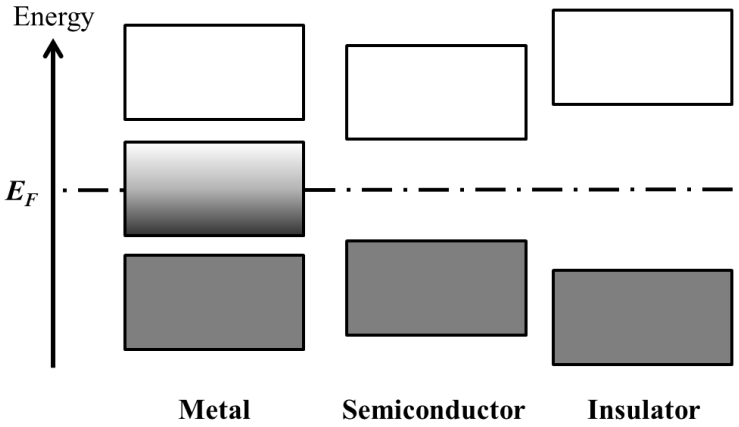

Fig. 1.6. Diagram of the electronic band structure of metals, semiconductors and insulators.

There are two types of semiconductor materials due to the fact that the electron flow can be carried out in two different ways. In the case of n-type semiconductors free-electrons are considered to "move" across covalent bonds through the conduction band. On the other hand, when an electron is excited to the conduction band it will leave a "hole" in the valence band. In this case a neighboring electron can move into this space and subsequently leave another void in its place and so on, making it appear as if the "hole" is moving, behaving like a positive-charged particle.

Most of organic compounds in the solid state have no conductive properties. However, this does not hold for those with conjugated π-electron systems that pack in the solid state in a manner that allows for interaction of the other π clouds of adjacent molecules. Phthalocyanines often meet those requirements and exhibit some levels of conductivity that provide the basis for their use in organic semiconductor devices.

Phthalocyanines were some of the first reported organic semiconductors, and together with other

polycyclic aromatic hydrocarbons they make up a large part of the charge-transfer complexes that present semiconductive properties.

The modifiable nature of phthalocyanines makes them excellent candidates for their use in optoelectronic devices as they can be easily processed as thin films. Unsubstituted phthalocyanines have been made into films by means of vacuum deposition. This technique is not considered to be efficient, as most of the material is wasted. The problem can be overcome by modifying the phthalocyanine structure to make it more soluble and thus rendering it ideal for creating thin films using methods such as spin-coating, drop casting and ink jet printing.

Functionalized-phthalocyanine-based thin films are currently being used as the conductive layers in a wide range of optoelectronic devices, such as organic light-emitting diodes, OSCs, and organic field-effect transistors [36, 37].

1.5.3 Liquid crystal properties

Also known as the "fourth state of matter", the liquid crystal phase (mesophase) is present between the solid and liquid phases and shares some properties of both states of matter. In liquids, the molecules exist in a highly disordered state in which all molecular directions are equivalent, therefore, no order is detected (isotropic). As we move towards the highly ordered crystal lattice, the molecules become completely anisotropic and arrange themselves in a fixed order and/or position.

In a liquid crystal, the molecules will arrange themselves due to anisotropic interactions to give a phase that presents some degrees of order either positional or orientational whilst preserving its fluidity (Fig. 1.7).

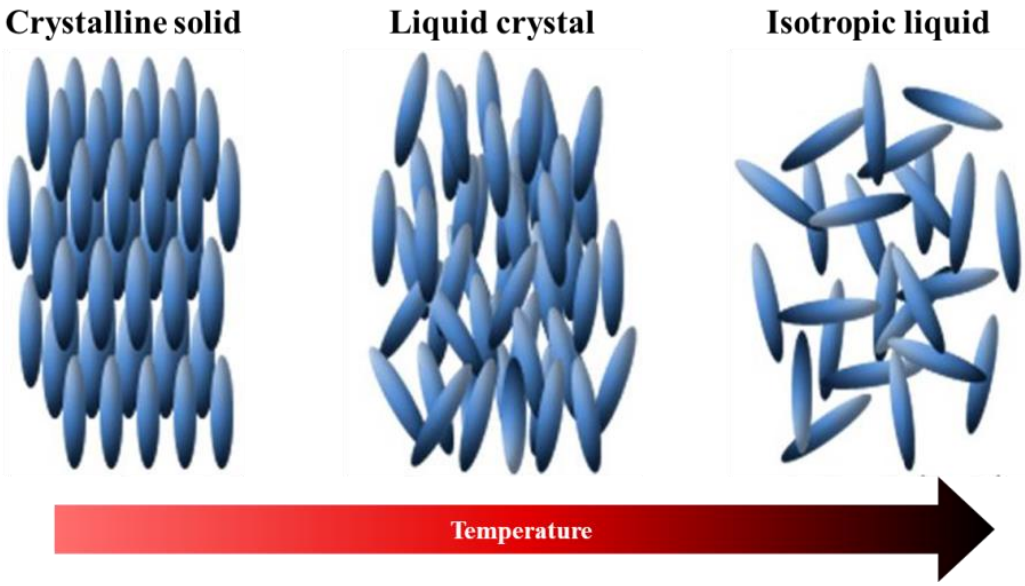

Fig. 1.7. Simplified diagrams of states of mater.

Molecular anisotropy is the main origin for the mesophase. This is due to the intermolecular interactions present in the material, which gives the molecules a preferred orientation or affinity to arrange in a certain direction. Particularly, each molecule presents a predominant axis that provides the direction in which the molecules will tend to arrange themselves by, with the shape of the molecule determining the predominant axis/directional order of the liquid crystal phase.

Liquid crystals can be divided into two main groups: thermotropic and lyotropic. While thermotropic liquid crystal has a stable mesophase at a specific temperature range, whilst lyotropic mesophases only occur upon the addition of a solvent to the liquid crystal material. The thermotropic liquid crystal can be sub-classified into calamitic and discotic liquid crystals. For the purpose of this research, we will focus solely on discotic-type liquid crystals.

The first discotic liquid crystalline materials were discovered in 1977 by Chandrasekhar and other examples were later reported in 1982. This sub-class is formed by disk-shaped molecules in which either one of its molecular axes is shorter than the other. These disk-shaped materials can form different types of liquid crystal phases according to their position and ordering as shown in the diagram below, Fig. 1.8.

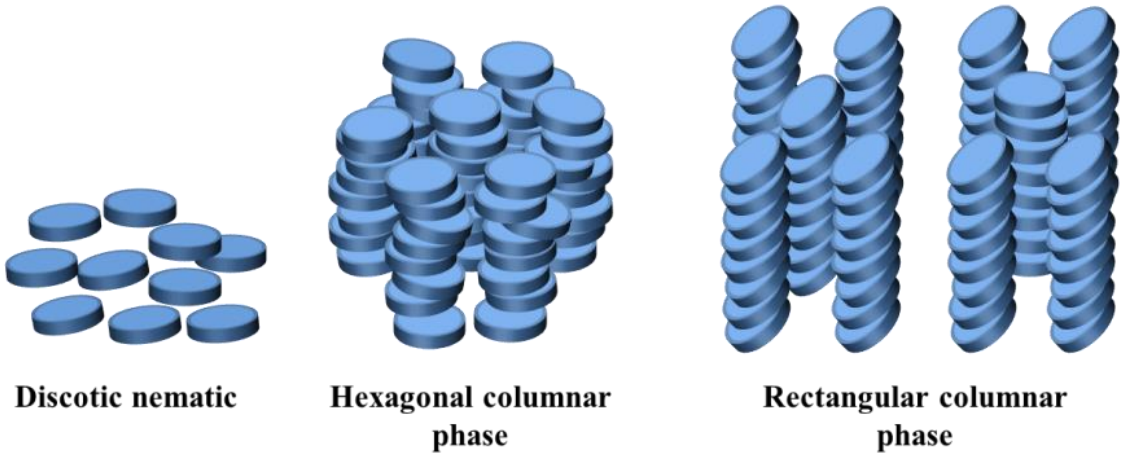

Fig. 1.8. Discotic liquid crystal classification.

The nematic mesophase arises when the molecules are arranged in a similar orientation in line with their longest axes. This arrangement lacks positional order, and therefore provides a high degree of fluidity in the system. When positional order is present however, the molecules will have a tendency to arrange themselves into columns and adopt a bi-directional lattice structure in either a rectangular or hexagonal form.

Phthalocyanines are known to be discotic mesogens. The most commonly known liquid crystalline materials are composed of an electron-rich aromatic core with aliphatic chains attached to

the periphery. Thus addition of aliphatic chains to the phthalocyanine nucleus was first investigated in the 1980's, when it was discovered that these flexible chains led to enhanced solubility in most organic solvents and most importantly promoted the columnar liquid crystal formation. Several groups investigated the effect that different substituents in the peripheral positions had on the formation of discotic mesophases. It was established that alkoxymethyl, alkoxy and alkyl chains led to columnar phase formation. The discotic liquid crystal behaviour was also investigated in the non-peripherally substituted phthalocyanines.

The study led by Cook *et al.* of the non-peripherally substituted macrocycles provided an in-depth understanding of the effect of the substituents on the mesogenic properties. Compounds with linear aliphatic chains of up to 18 carbons and a range of metals such as Cu, Co, Zn, Ni and Pd were investigated, but focus was set on chains of 5-10 carbons. These materials were found to display remarkable properties such as polymesomorphism in which some materials presented up to four different mesophases [38]. Further, examination of the properties of these liquid crystalline materials showed that the derivatives gave an excellent conductiometric response to NO_2 whilst a different group used a thin-film of the octahexyl analogue for the development of a gas sensor.

1.5.4 Phthalocyanines for organic solar cells

In terms of OSC, the synthesis of stable low band gap polymers for efficient light-to-electricity conversion is a major challenge. OSCs employing polymer–fullerene heterojunctions have been shown to have the high PCEs [6]. However, most of the available conjugated polymers exhibit band gaps of ca. 2 eV. Therefore, there is a clear mismatch between the absorption spectrum of these macromolecules and the terrestrial solar spectrum, which extends to the near IR.

Phthalocyanines exhibit the high extinction coefficients around 700 nm where the maximum of the solar photon flux occurs for efficient photon harvesting, and many other features, that make them especially suitable for integration in light energy conversion systems. Phthalocyanines have the excellent stability, rich redox chemistry, *p*-type and also *n*-type semiconducting properties, and relative high charge carrier mobility. Therefore, phthalocyanines are among the most intensively studied dyes in this field. They are incorporated as antennas into photovoltaic devices usually in blends together with semiconducting polymers and/or acceptor counter partners such as fullerenes [15, 39].

Thus, a planar-heterojunction structured copper phthalocyanine (CuPc)/C_{60} thin-film solar cell with Ag as the metal cathode with PCE of 3.5% has been described. Moreover, the PCEs exceeding 5.5% have been obtained by stacking in series two of these cells [40, 41]. The control of V_{oc} in

organic PV cells with multicharge separation interfaces (CuPc or ZnPc/$_{C60}$ and pentacene/C_{60}) by inserting an ultrathin metallated phthalocyanines layers, has been reported with PCEs reaching 2.04% [42]. OSCs using hexadecafluorophthalocyaninatocopper (CuF16Pc) as electron acceptor material and para-sexiphenyl as electron donor have been reported recently [43]. Doping-induced efficiency enhancement in organic photovoltaic devices has been described recently. By doping rubrene into CuPc/C_{60}-based solar cell, an exceptionally high PCE of 5.58% was achieved [44]. The performance improvement is mainly attributed to efficient light absorption by rubrene in the range of 460–530 nm, where two hosts have low absorbance, leading to more effective exciton formation. These findings motivate the use of fluorescent dyes for maximizing absorption spectral coverage, as well as increasing photon harvesting. Recently, Miyake has reported the high hole and electron drift mobilities in the crystalline phase of a mesogenic phthalocyanine derivative, C6PcH_2 and the BHJ OSCs utilizing the soluble phthalocyanine have reported with the PCEs exceeding 3.1% [9, 10].

Chapter 2

Effects of processing additives on donor and acceptor phase separation, crystallization and photovoltaic performances of solar cells

2.1 Introduction

In terms of BHJ OSCs, by intermixing donors with methanofullerene derivatives, the efficient exciton dissociation is achieved with a large interfacial area, overcoming the limited exciton diffusion length in the BHJ materials, and the high photovoltaic performance is demonstrated. However, continuous pathways for the selective transportation of both electrons and holes to electrodes are essential, and must be controlled to allow maximum absorption of thick films without significant recombination loss [45]. The optimum separation of donor and acceptor phases must have a balance between a large interfacial area and continuous pathways for carrier transportation [46]. Recently, significant progress to control the separation of donor and acceptor phases in BHJ OSCs has been made by optimization of device preparation conditions, including the application of the adjustment of the volume fractions of the components, thermal annealing treatment, and processing additives [19, 21, 47].

Postproduction heat treatment is one approach toward controlling separation of donor and acceptor phases, which resulted in improvement of both J_{sc} and *FF*. Recent studies have demonstrated improved PCE after thermally annealing polymer-fullerene composite OSCs at elevated temperatures [19, 48-50]. In 2003, F. Padinger et al. reported the high PCE of 3.5% for P3HT:PCBM composite OSCs after postproduction thermal annealing at 75 °C [48]. This demonstration led to extensive studies on the “thermal annealing” approach, and PCE values up to 5% were demonstrated [19]. The higher PCE was attributed to thermally induced morphology modification, thermally induced crystallization, and improved transport across the interface between the BHJ material and the Al electrode.

The thermal annealing approach has been utilized to control the nanoscale morphology of BHJ thin films made of $C6PcH_2$ and [60]PCBM via spin-casting for photovoltaic applications. Although the improved photovoltaic performance of $C6PcH_2$:[60]PCBM BHJ OSCs was observed after 10 minute postproduction thermal annealing at 60 °C, the photovoltaic performances of the OSCs were strongly degraded for all parameters after 15 minute of thermal annealing at 125 °C [51]. After thermal annealing, the surface of the thin films, which was observed by optical microscopy, revealed

the presence of defects and holes within the active layer, which might have caused the diffusion of aluminum atoms through the active layer and probably contributed to the lower performances of the OSCs.

Recently, the addition of an alkanedithiol to the main solvent has been shown to markedly improve the photovoltaic performance of BHJ OSCs [21, 52-54]. Although evidences of the formation of phase-separated BHJ materials were clearly observed from AFM images of the surface composite films, there was no alkanedithiol in the thoroughly dried films [21]. It was suggested that the alkanedithiol functioned as a processing additive that improved the nanoscale morphology of the BHJ materials. Moreover, one found that there is no indication of improving crystallization in composite thin films either with or without dithiol processing.

Herein, we clarify two effects of processing additives on BHJ thin films made of $C6PcH_2$ and [60]PCBM via spin-casting that are used for photovoltaic applications. By adding various solvents as processing additives to a volume of a few percent, i) nanoscale phase separation was promoted and ii) the crystallinity of the discotic $C6PcH_2$ molecules with the hexagonal structures was reinforced. The photovoltaic cells in the structure of indium tin oxide (ITO)/MoO_x/BHJ/LiF/Al (Fig. 2.1), with the optimum phase-separated BHJ materials and high crystallinity of the discotic $C6PcH_2$ molecules, had a PCE of 4.2%.

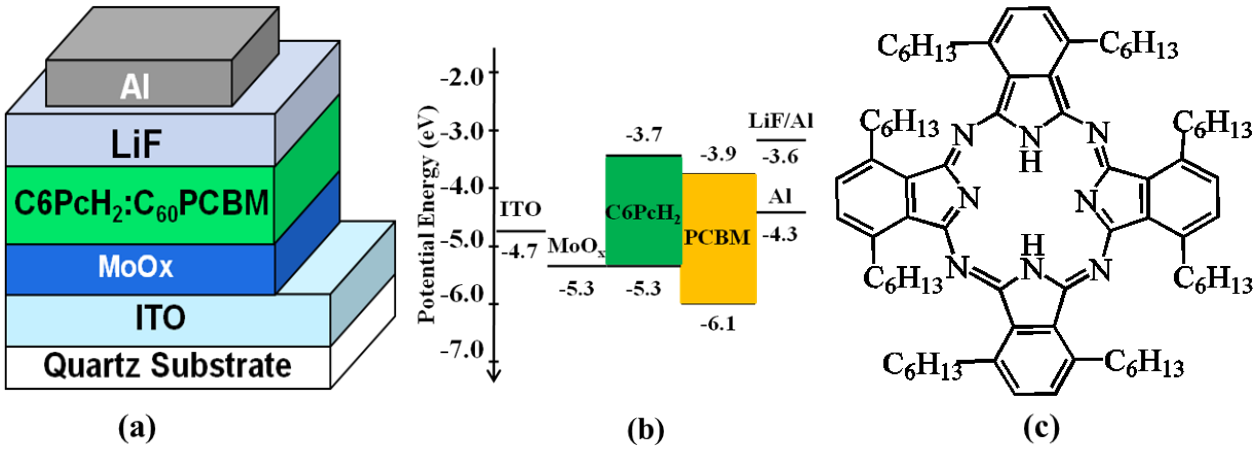

Fig. 2.1. (a) device architecture, (b) energy levels.liquid crystal classification, and (c) Chemical structure of $C6PcH_2$ molecule.

2.2 Experimental procedure

$C6PcH_2$, as shown in Fig. 2.1(c), was synthesized as described in the literature [55], with slight modifications, and fully purified by column chromatography (using silica gel with toluene as the eluent), which was followed by repeated recrystallization from toluene-methanol (1:2) solution [9]. PCBM and the solvents used as processing additives, such as 1,8-diiodooctane (DIO), 1,8-dichlorooctane (Chlor), 1,8-dibromooctane (Brom), and 1,8-octanedithiol (Oct), were purchased from Frontier Carbon and Sigma-Aldrich, respectively.

BHJ thin films were prepared under optimized conditions in accordance with the following procedure. An ITO-coated quartz substrate was cleaned with detergent, ultrasonicated in water, chloroform, acetone, and isopropyl alcohol, and subsequently dried with UV-induced ozone. 6-nm-thick MoO_x films were thermally evaporated onto ITO at a rate of 0.1 Å/s under a vacuum of about 2×10^{-5} Pa. A solution containing a mixture of $C6PcH_2$:[60]PCBM (2:1) in different organic solvents with or without a processing additive was stirred using an ultrasonic washer, which increased the temperature of the solution to 45 ºC, and spin-cast at 2000 rpm onto a MoO_x layer. The concentration of the solution with the various primary solvents was summarized in Table 2.1 and the active layers were approximately 130 nm. Herein, the thickness of the active layers was estimated from AFM images. Finally, a 0.3-nm-thick LiF buffer layer and an 80-nm-thick aluminum layer were deposited through a shadow mask by thermal evaporation under a vacuum of about 2×10^{-5} Pa. The active area of the device was 4 mm^2.

Table 2.1. Solution concentrations in this study

	$C6PcH_2$ (mg/ml)	[60]PCBM (mg/ml)
Chloroform	14.9	7.45
Trichloroethylene	20.4	10.2
Toluene	22	11

The device characteristic was measured under irradiation intensity of 100 mW/cm^2 using an XES 301 (AM 1.5 G) full spectrum solar simulator. The current density-voltage (*J*-*V*) characteristics were measured using a source measurement unit (Keithley 2400). Otherwise, EQE spectra were measured with a programmable electrometer using Xe lamp light passed through a monochromator as a light source. The integrated EQE values always showed good agreement with the measured valued of J_{sc}. The absorbance spectra, PL spectra, and surface morphology were measured by spectrophotometry (Shimadzu UV-3150), using a fluorescence spectrophotometer (F-4500), and AFM (Keyence

VN-8000), respectively. Furthermore, the crystallinity of the $C6PcH_2$ thin films was evaluated by XRD (Rigaku RINT 2000).

2.3 Effects of processing additive on donor-acceptor phase separation and crystallization

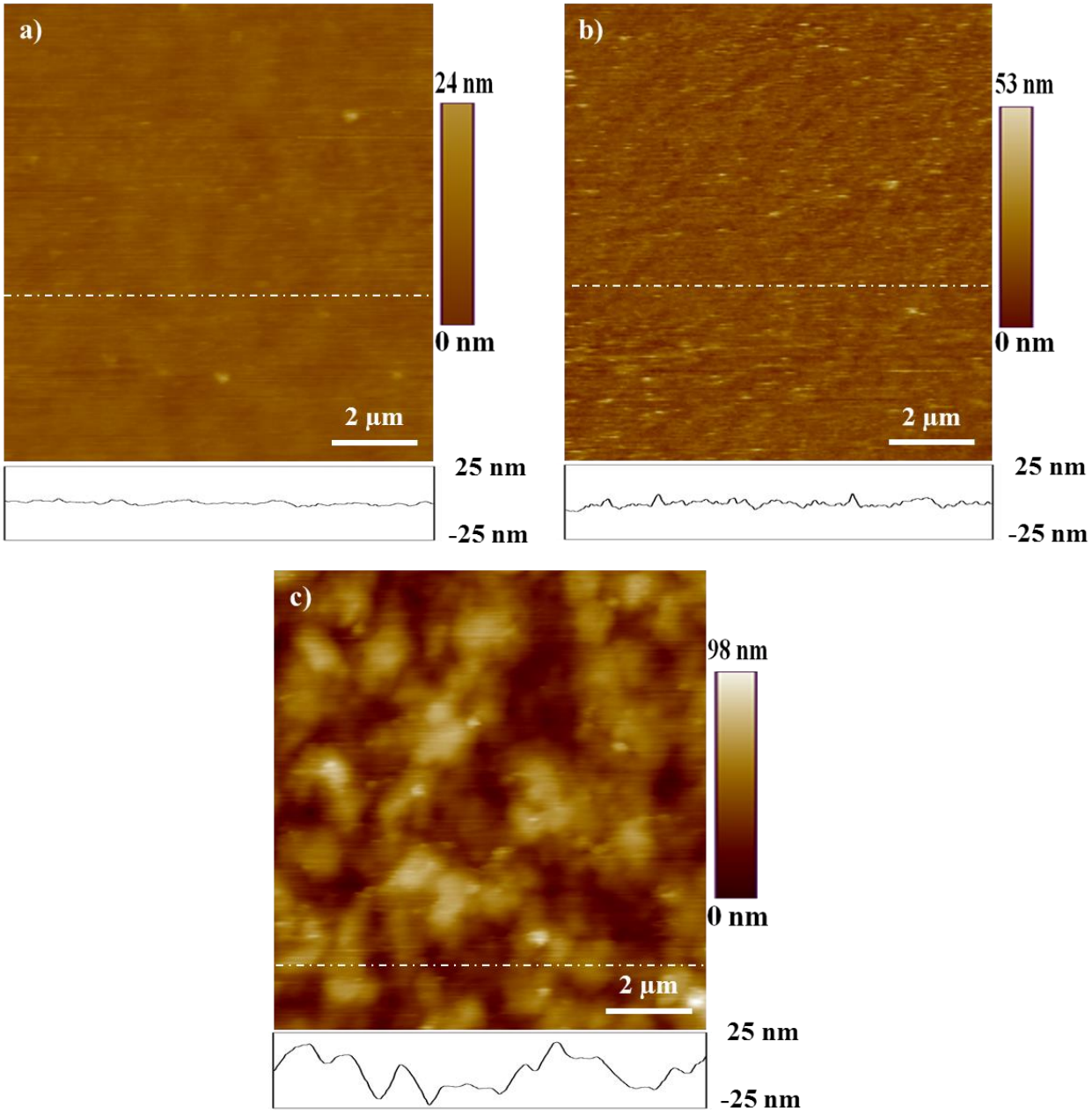

Fig. 2.2. AFM images of surface of $C6PcH_2$:[60]PCBM composite thin films: (a) without DIO, (b) with 0.2% v/v of DIO, and (c) with 0.8% v/v of DIO.

One found that the domains of BHJ materials, which observed from surfaces of composite thin films, were elongated and the donor and acceptor phases were separated by utilizing processing additives [21, 54]. Figure 2.2 shows the surface morphologies of $C6PcH_2$:[60]PCBM composite thin

films with different amounts of DIO as a processing additive in toluene solution, which were observed by AFM.

The $C6PcH_2$:[60]PCBM composite thin film, spin-cast from the blend solution in pure toluene, has a smooth surface with an average surface roughness of 1.4 nm. Upon adding 0.2% and 0.8% v/v of DIO as a processing additive, a number of islands, which considered to be $C6PcH_2$ domains and/or [60]PCBM clusters, appeared on the smooth surface of the $C6PcH_2$:[60]PCBM composite thin film, and the average surface roughness gradually increased to 3.2 nm and 13.1 nm, respectively. This result suggests that utilizing DIO as a processing additive caused the phase separation in BHJ films.

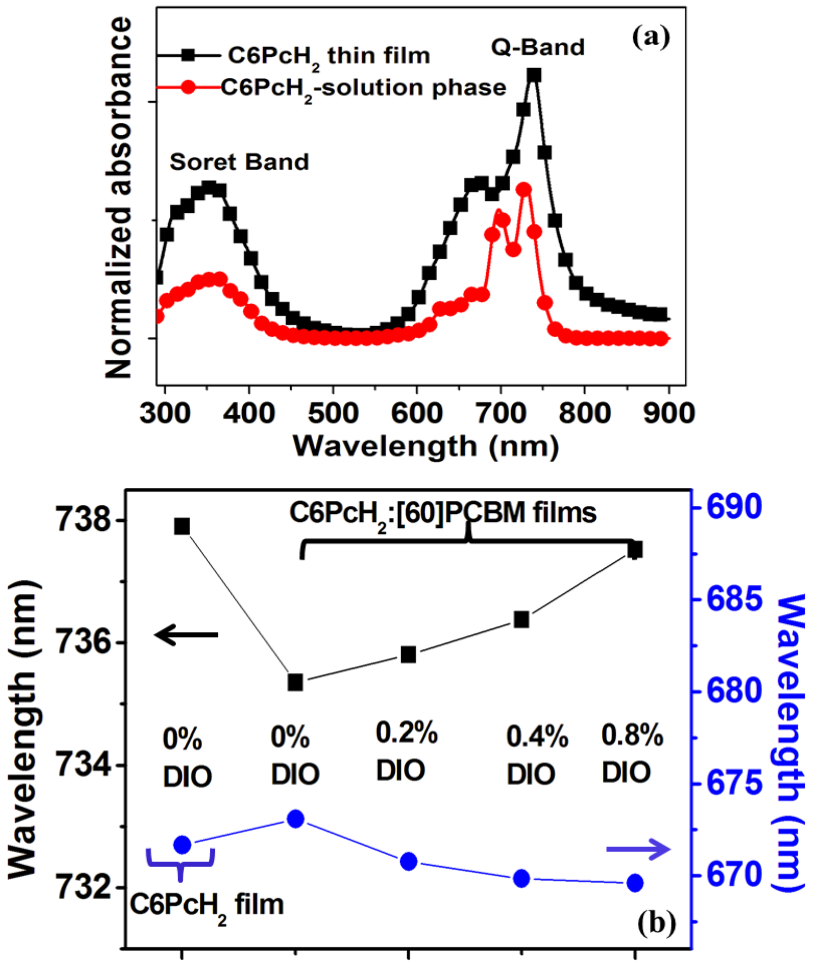

Fig. 2.3. (a) Absorbance spectra of $C6PcH_2$ in dried thin film and in toluene solution. Absorbance spectra of $C6PcH_2$ in toluene solution was normalized at 729.8 nm (b) Dependence of size of the Davydov splitting on different amounts of DIO.

Aggregates of phthalocyanine molecules generally exhibit an absorbance spectrum with a broad Q-band that is blue-shifted (H-aggregates) or red-shifted (J-aggregates) with respect to the solution

phase [56-58]. However, the $C6PcH_2$ spin-cast thin film, as depicted in Fig. 2.3(a), showed blue and red shifts of the Q-band relative to the solution phase from 697.4 nm to 671.8 nm and from 729.8 nm to 737.9 nm, respectively. Although more efforts should be made to understand the arrangement of discotic $C6PcH_2$ with hexagonal structures, it can be seen that this splitting is consistent with Davydov splitting, which occurs in a crystalline lattice containing translationally nonequivalent molecules, such as a columnar "herringbone" array [58].

Different band shapes in absorbance spectra might result from variations in the orientation and/or packing of molecules within thin films. In particular, the size of Davydov splitting in an allowed electronic transition is a direct measure of the interaction energy between molecules with differing site symmetries [59, 60]. The Davydov splittings, which are indicated by the difference of the Q-band peak wavelengths, of the absorbance spectra of $C6PcH_2$ and $C6PcH_2$:[60]PCBM spin-cast thin films fabricated on quartz substrates from toluene with and without DIO as a processing additive are shown in Fig. 2.3(b). The Davydov splitting at the Q-band of the $C6PcH_2$:[60]PCBM thin films increased gradually upon adding DIO. The increase in the Davydov splitting indicated that the discotic $C6PcH_2$ with the hexagonal structures interacted more strongly and/or that there was an improvement in the local structural order of the $C6PcH_2$ molecules compared with the case that the films were processed using pure toluene.

On the other hand, the decrease in the Davydov splitting with the addition of [60]PCBM to the $C6PcH_2$ thin films indicated that the molecular separation of the discotic $C6PcH_2$ with the hexagonal structures increased owing to the diffusion of [60]PCBM into the $C6PcH_2$ domains, which might occur in a $C6PcH_2$:[60]PCBM mixture. Combining all the above mentioned results, we suggest that donor and acceptor phases were separated by utilizing DIO as a processing additive.

Figure 2.4 shows XRD patterns of $C6PcH_2$ and $C6PcH_2$:[60]PCBM thin films fabricated on glass substrates with and without DIO in toluene solution as a processing additive. It can be seen that the diffraction peak of the $C6PcH_2$ thin film occurred at approximately 4.86º, which corresponds to the intercolumnar distance in the hexagonal structures of 18.2 Å. The increase in the full width at half maximum (FWHM) of the XRD patterns upon adding [60]PCBM, as shown in Table 2.2, indicated that the crystallinity of the discotic $C6PcH_2$ with the hexagonal structures was reduced owing to the dispersion of [60]PCBM into the $C6PcH_2$ domains. In contrast, upon incorporating DIO as a processing additive, the FWHM decreased and the crystallinity of the discotic $C6PcH_2$ with the hexagonal structures was markedly improved. The strong dependence of the crytallinity of $C6PcH_2$ molecules upon the addition of DIO is completely opposite that of low-band-gap polymers such as poly[2,6-(4,4-bis-(2-ethylhexyl)-4*H*-cyclopenta[2,1-b;3,4-b']-dithiophene)-*alt*-4,7-(2,1,3-benzothiadi

azole)], in which the absence of crystallization was reported for the both cases with and without processing additives [21].

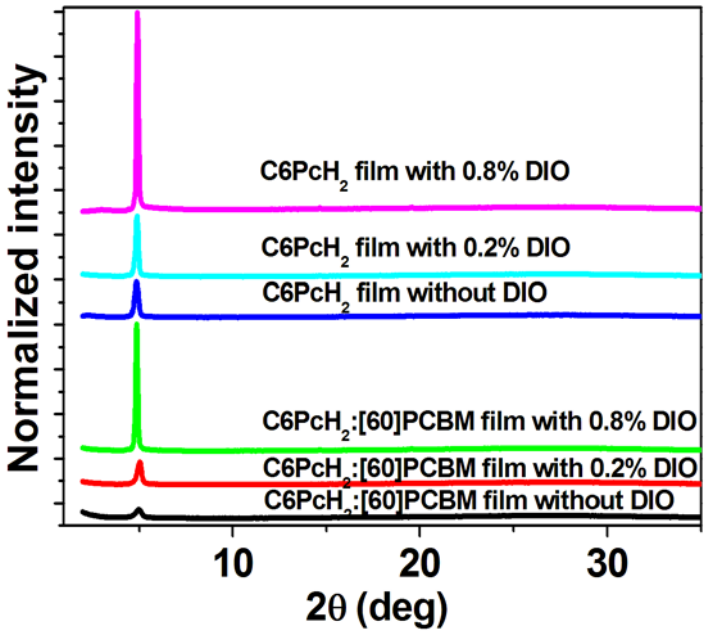

Fig. 2.4. XRD patterns of $C6PcH_2$ and $C6PcH_2$:[60]PCBM composite thin film with different amounts of DIO. All XRD patterns were normalized at 4.88º.

Table 2.2. FWHM of XRD patterns of $C6PcH_2$ and $C6PcH_2$:[60]PCBM composite thin film with and without DIO as a processing additive in toluene solution

	No DIO	0.2% DIO	0.8% DIO
$C6PcH_2$ films	0.26º	0.18º	0.13º
$C6PcH_2$:[60]PCBM films	0.56º	0.29º	0.13º

Moreover, upon adding DIO, the FWHM of the XRD patterns of the $C6PcH_2$ thin films was gradually decreased, as shown in Table 2.2, and the crystallinity of the discotic $C6PcH_2$ columns in the hexagonal structures was improved. This indicated that the addition of DIO affects not only the separation of [60]PCBM and $C6PcH_2$ phases but also the crystallization of $C6PcH_2$ molecules in the hexagonal structures.

One saw that during the stirring process using ultrasonic treatment, the temperature of the solution increased and the solubility of $C6PcH_2$ molecules in DIO was improved. These $C6PcH_2$ molecules in the DIO-solution phase recrystallized during natural cooling. It is proposed that the recrystallization of the $C6PcH_2$ in the DIO-solution phase caused the improved crystallinity of the discotic $C6PcH_2$ in the dried thin films. This process is similar to the recrystallization from

toluene-methanol solution, as reported by Miyake et al. [9]. To establish the validity of the proposal, the $C6PcH_2$ thin films were fabricated by spin-casting from the solution while stirring using a magnetic rod. It is noted that the temperature of the BHJ blend solution was remained at room temperature during the stirring process using the magnetic rods. The XRD patterns of the thin films had an FWHM of approximately 0.22º and there was no indication of the improved crystallinity of $C6PcH_2$ molecules in the dried thin films either with or without the solvents as processing additives.

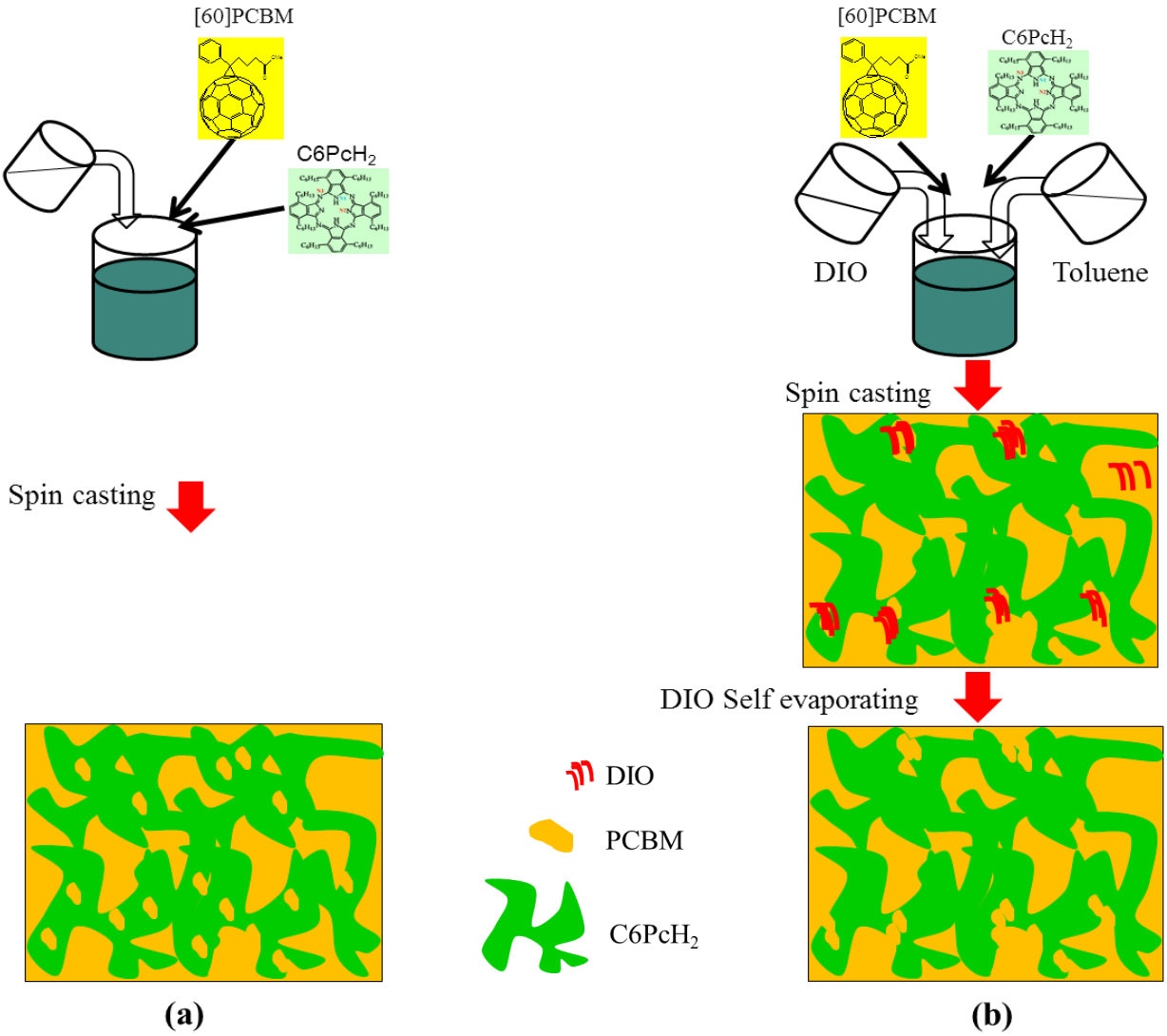

Fig. 2.5. Proposed models during spin-cast processing (a) without DIO and (b) with DIO.

Furthermore, a model described in the following is proposed and illustrated in Fig. 2.5 to explain the aforementioned effects of DIO on the separation of $C6PcH_2$ and [60]PCBM phases. One found that when $C6PcH_2$ and [60]PCBM are dissolved in toluene, $C6PcH_2$ domains extend freely in the solvent and probably do not interact with PCBM. During spin-coating, when toluene is extracted

rapidly, the whole system is quenched into a metastable state and [60]PCBM molecules are finely dispersed between $C6PcH_2$ domains, interrupting the ordering of $C6PcH_2$ molecules. This is supported by the decreases in Davydov splitting widths, smooth surface morphology, and low crystallization of discotic $C6PcH_2$ in hexagonal structures.

On the other hand, when a small amount of DIO exists in the mixture solvent, the situation is different. Because the vapor pressure of toluene (111 ºC) is lower than DIO (167 ºC), toluene evaporates faster than DIO during spin-cast processing, and the concentration of DIO gradually increases in the mixture. Due to the poor solubility of $C6PcH_2$ molecules in DIO (Fig. 2.6), [60]PCBM, which dissolved in DIO solvent, initially form clusters and precipitate. Moreover, with the smaller amount of [60]PCBM contained in toluene, the $C6PcH_2$ domains are able to self-organize. Finally, [60]PCBM and $C6PcH_2$ domains were separated. In other words, the composite active layer ‘‘intelligently’’ phase separates into the optimum morphology in one single step rather than two stages in ‘‘thermal annealing’’, and takes less time than ‘‘solvent annealing’’ [19-20].

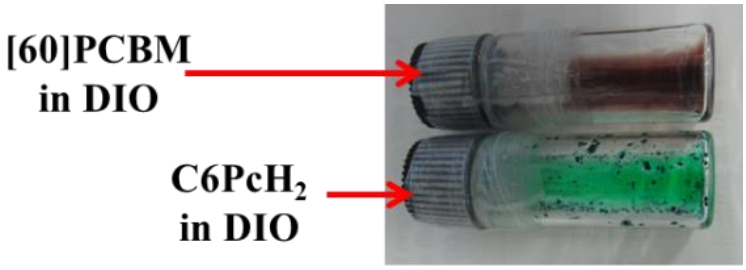

Fig. 2.6. Photos of BHJ materials in DIO solvent

2.4 Effects of processing-additive-induced donor-acceptor phase separation and crystallization on photovoltaic properties

One found that the photovoltaic performance of BHJ OSCs is strongly dependent on the donor-acceptor phase separation and crystallinity of the BHJ materials [19-21, 61, 62]. Thus, when the adding DIO to the BHJ blend solution induced the separation of $C6PcH_2$ and [60]PCBM and the crystallization of $C6PcH_2$ molecules in hexagonal structures, the improving photovoltaic performance is expected. Figure 2.7 shows the EQE and *J-V* characteristics of $C6PcH_2$:[60]PCBM devices with the different amounts of DIO mixed with toluene in an ITO/MoO_x/BHJ/LiF/Al structure under AM 1.5G illumination at an intensity of 100 mW/cm^2. The cell characteristics for all devices are summarized in Table 2.3.

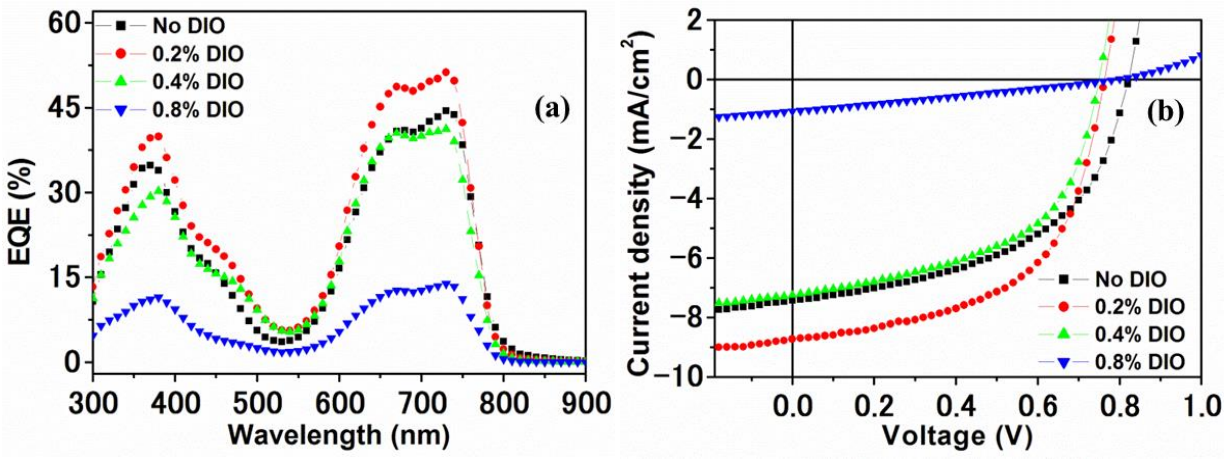

Fig. 2.7. (a) EQE spectra and (b) *J-V* characteristics of C6PcH$_2$:[60]PCBM BHJ OSCs with different amounts of DIO mixed with toluene.

Table 2.3. Cell characteristics of C6PcH$_2$:[60]PCBM BHJ OSCs with different amounts of DIO mixed with toluene under AM 1.5G illumination at an intensity of 100 mW/cm^2.

DIO	J_{sc} (mA/cm^2)	V_{oc} (V)	*FF*	η (%)
No DIO	7.4	0.82	0.51	3.1
0.2 %	8.7	0.77	0.55	3.7
0.4 %	7.3	0.75	0.53	2.9
0.8 %	1.1	0.79	0.23	0.2

The devices, the active layers of which were spin-cast from C6PcH$_2$:[60]PCBM blends in pure toluene solution, showed the EQE of 44% at the Q-band of C6PcH$_2$ molecules and the PCEs of 3.1% with J_{sc} of 7.4 mA/cm^2, V_{oc} of 0.82 V, and *FF* of 0.51. By utilizing DIO as a processing additive to modify the nanoscale phase separation and the crystallinity, the performance of the BHJ OSCs was controlled. In particular, by adding 0.2% v/v of DIO in toluene solution the EQE at the Q-band increased to 51%. As a result of the increase in EQE, the J_{sc} and PCE increased to 8.7 mA/cm^2 and 3.7%, respectively, and the *FF* was improved from 0.51 to 0.55 due to the modified nanomorphology of the C6PcH$_2$:[60]PCBM thin films. However, the photovoltaic performance of the C6PcH$_2$:[60]PCBM BHJ OSCs was reduced with the low PCE of 0.23% upon adding 0.8% v/v of DIO, as shown in Table 2.3.

To explain the effects of the donor-acceptor phase separation and crystallization of C6PcH$_2$ molecules in hexagonal structure on the photovoltaic performance of C6PcH$_2$:[60]PCBM BHJ OSCs,

we proposed the schematics in the following and illustrate it in Fig. 2.8. In the cases of no DIO, [60]PCBM molecules were probably dispersed between $C6PcH_2$ domains during spin-cast processing. Although this resulted in the large interfacial areas of donor and acceptor and the high efficient exciton dissociation, the crystallization of $C6PcH_2$ domains were reduced. The deterioration of crystallization of the BHJ materials, therefore, caused the poor transportation of both electrons and holes to electrodes. As a result, the photovoltaic performance of the BHJ OSCs was poor.

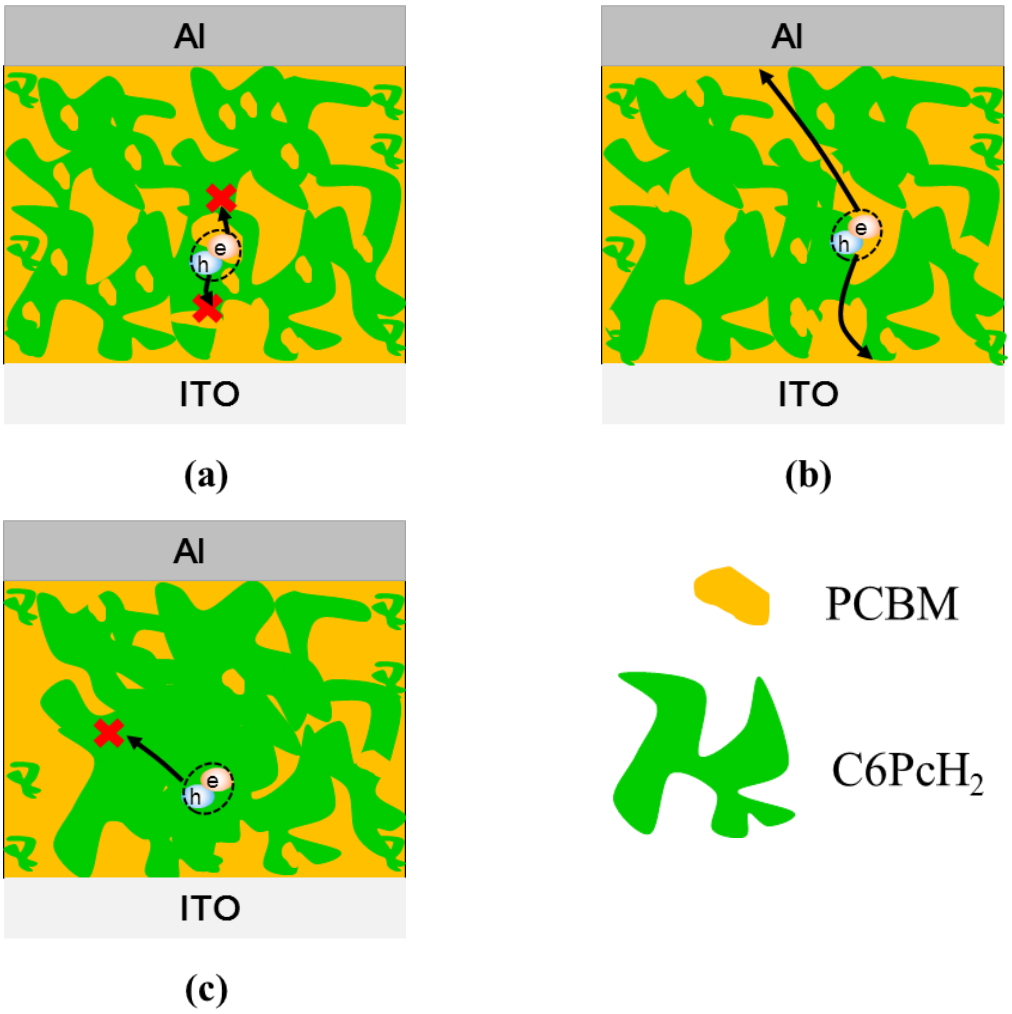

Fig. 2.8. Proposed schematics of donor-acceptor phase-separated structures of the active layers fabricated with (a) no DIO, (b) 0.2% DIO, and (c) 0.8% DIO.

By adding small amount of DIO to the BHJ blend solutions, [60]PCBM was separated from the $C6PcH_2$ domains and the crystallization of $C6PcH_2$ molecules in the hexagonal structures was improved due to the poor solubility of $C6PcH_2$ in DIO and the difference in boiling point between DIO and toluene. As a result, the continuous pathways for the transportation of charge carrier to

electrodes were improved. However, by adding 0.8% v/v of DIO to the BHJ blend solutions, the interfacial areas of donor and acceptor phases became smaller and the efficient exciton dissociation was low. This also resulted in the low photovoltaic performance of the BHJ OSCs. The optimum nanoscale phase separation and crystallization of the BHJ materials, and the high photovoltaic performance of the $C6PcH_2$:[60]PCBM BHJ OSCs was probably achieved by adding 0.2% v/v of DIO to the BHJ blend solution.

The proposed schematics was confirmed by taking the PL spectra of the $C6PcH_2$ $C6PcH_2$:[60]PCBM thin films into consideration. Figure 2.9 shows the PL spectra of the $C6PcH_2$ and $C6PcH_2$:[60]PCBM thin films fabricated on quartz substrates with the different amount of DIO and the dependence of the relative quenching efficiency (Q) on the amount of DIO. Herein, Q was calculated from the equation; Q = 1 - (total PL of BHJ sample/total PL of reference sample).

The PL spectra of $C6PcH_2$ thin films had a predominant peak at 766 nm and a shoulder around 820 nm, which relate with the Q-band of the $C6PcH_2$ absorption spectra [63]. The PL intensity of $C6PcH_2$:[60]PCBM thin films was markedly suppressed and the Q drastically increased upon adding [60]PCBM. The PL suppression and the increases in Q was due to the nonradiative decay of photogenerated-excitons through the photoinduced-electron transfer from the excited state of $C6PcH_2$ to [60]PCBM [1-4]. Furthermore, the increases in the Q indicated that the interfacial areas of donor and acceptor were enlarged, which caused the high efficiency of exciton dissociation. By adding small amount of DIO to the blend solutions, the Q was reduced. It is suggested that the interfacial areas of donor and acceptor phases was reduced, which was in good agreement with the schematics proposed above.

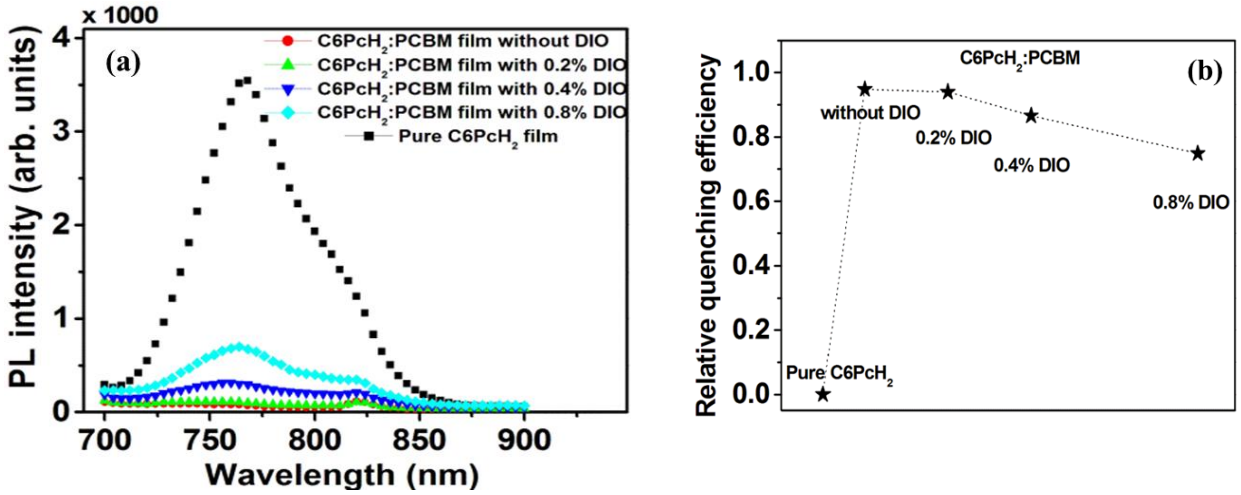

Fig. 2.9. (a) PL spectra of $C6PcH_2$ and $C6PcH_2$:[60]PCBM composite thin films with the different amount of DIO and (b) dependence of the relative quenching efficiency on the amount of DIO; the excitation wavelength is 670 nm.

2.5. Improving photovoltaic properties by optimizing donor-acceptor phase separation and crystallization

According to the proposed models, the processing additives in the mixture solvent approach should fulfill the following requirements: first, the compound must have higher boiling point than that of the primary solvent. Second, the solubility of [60]PCBM and $C6PcH_2$ in the compound must be different. Third, the compound must be miscible with the primary solvent. Based on these requirements, the new processing additives with the different boiling points were selected, as shown in Table 2.4. On the other hand, the various primary solvents, as shown in Table 2.5, were utilized. By using the various processing additives mixed with the different primary solvents, the optimum donor-acceptor phase separation and crystallization of discotic $C6PcH_2$ are expected hence the photovoltaic properties must be improved.

Table 2.4. Boiling points of the processing additives in this study.

	DIO	Oct	Brom	Chlor
Boiling point (ºC)	167	269	270	116

Table 2.5. Boiling points of the primary solvent in this study.

	Chloroform	Toluene	Trichloroethylene
Boiling point (ºC)	62	111	87

Figure 2.10 shows the surface morphologies of $C6PcH_2$:[60]PCBM composite thin films with the various primary solvents, which were observed by AFM. The $C6PcH_2$:[60]PCBM composite thin film without DIO exhibited a smooth surface, as shown in Fig. 2.10(a). By adding 0.2% v/v of DIO to the BHJ blend solutions, all of the $C6PcH_2$:[60]PCBM composite thin films showed a number of islands, which is considered to be discotic $C6PcH_2$ domains and/or [60]PCBM clusters. This result suggests that utilizing DIO mixed with all of primary solvents in this study caused the phase separation of the BHJ materials. However, the discotic $C6PcH_2$ domains and/or [60]PCBM clusters on the $C6PcH_2$:[60]PCBM composite thin films utilized trichloroethylene possessed higher uniformity than those of the composite thin films utilized chloroform or toluene.

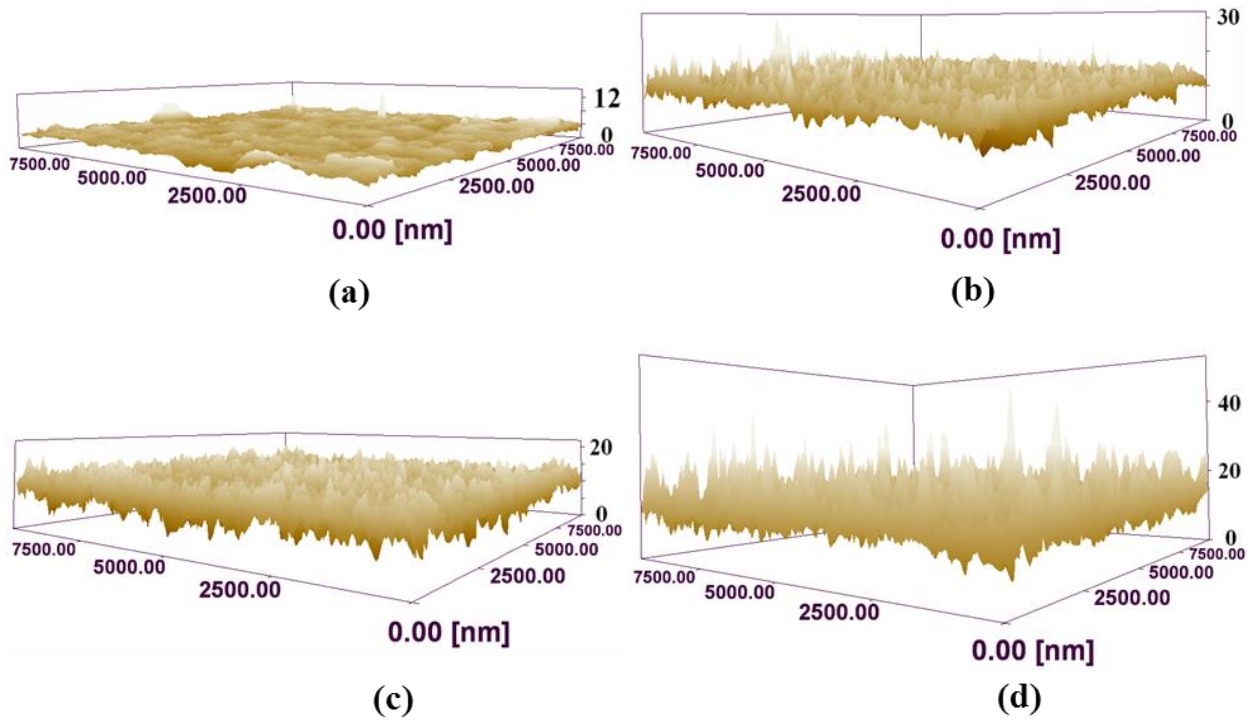

Fig. 2.10. AFM images of the $C6PcH_2$:[60]PCBM composite thin films without DIO (a) and with DIO (b, c, and d) in the various solvents: chloroform (a, b), TCE (c), and toluene (d).

Figure 2.11 shows the Davydov splitting at the Q-band of the absorbance spectra of $C6PcH_2$:[60]PCBM composite thin films utilizing 0.2% v/v of various processing additives, such as DIO, Chlor, Brom, and Oct. Herein, the $C6PcH_2$:[60]PCBM composite thin films was spin-cast on quartz substrates from the solutions containing a mixture of $C6PcH_2$:[60]PCBM in chloroform mixed with various processing additives. Although Davydov splitting at the Q-band occurred for all process additives, the addition of Oct induced less Davydov splitting than those of the other solvents.

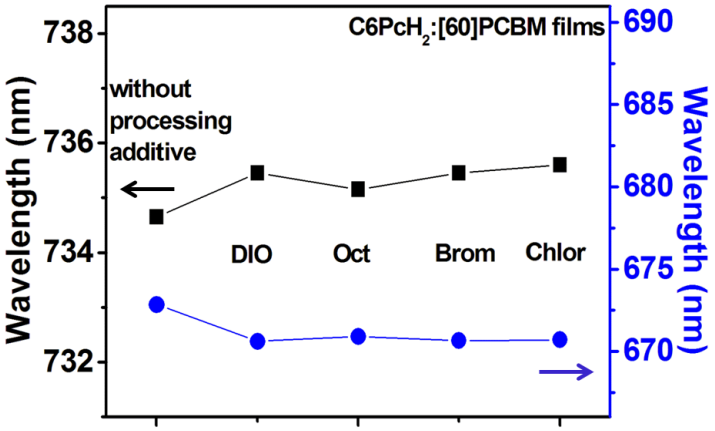

Fig. 2.11. Dependence of size of the Davydov splitting on 0.2% v/v of various processing additives.

Figure 2.12 shows XRD patterns of C6PcH$_2$:[60]PCBM thin films with 0.2% v/v of various solvents as processing additives, such as DIO, Chlor, Brom, and Oct, in chloroform solution. All the XRD patterns exhibited the similar shapes and consisted of the only diffraction peak appeared at approximately 4.88º, corresponding to Miller indices of (200)/(110) (using indices based on a rectangular cell). Furthermore, the FWHM of all XRD patterns are summarized in Table 2.6. Although decreases in the FWHM of the XRD patterns or the improved crystallinity of the discotic C6PcH$_2$ columns in the hexagonal structures occurred for all the processing-additive solvents, the addition of Oct as a processing additive resulted in the lowest crystallinity.

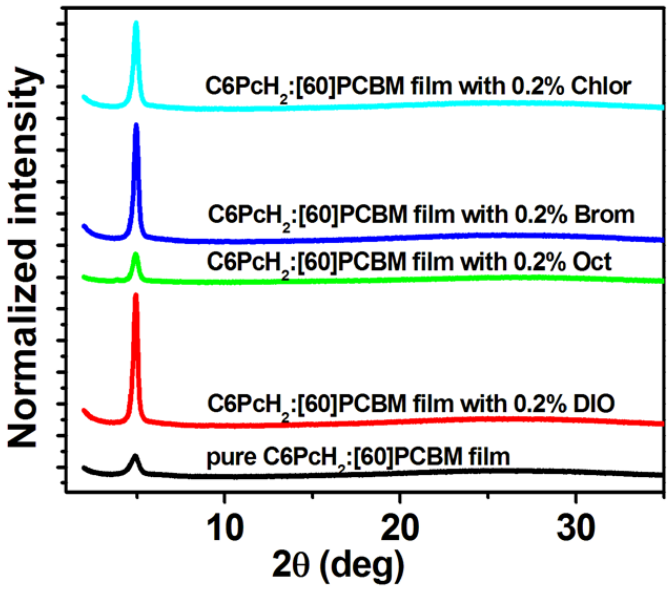

Fig. 2.12. XRD patterns of C6PcH$_2$:[60]PCBM composite thin film with 0.2% v/v of various processing additives. All XRD patterns were normalized at 4.88º.

Table 2.6. FWHM of XRD patterns of C6PcH$_2$:[60]PCBM composite thin film with and without different processing additives mixed with chloroform

	No processing additives	0.2% DIO	0.2% Oct	0.2% Brom	0.2% Chlor
C6PcH$_2$:[60]PCBM films	0.92 º	0.31 º	0.49 º	0.3 º	0.36 º

Figure 2.13 shows the EQE and J-V characteristics of C6PcH$_2$:[60]PCBM devices with the various primary solvents mixed with 0.2% v/v of DIO in an ITO/MoOx/BHJ/LiF/Al structure under AM 1.5G illumination at an intensity of 100 mW/cm^2. The cell characteristics for all devices are summarized in Table 2.7.

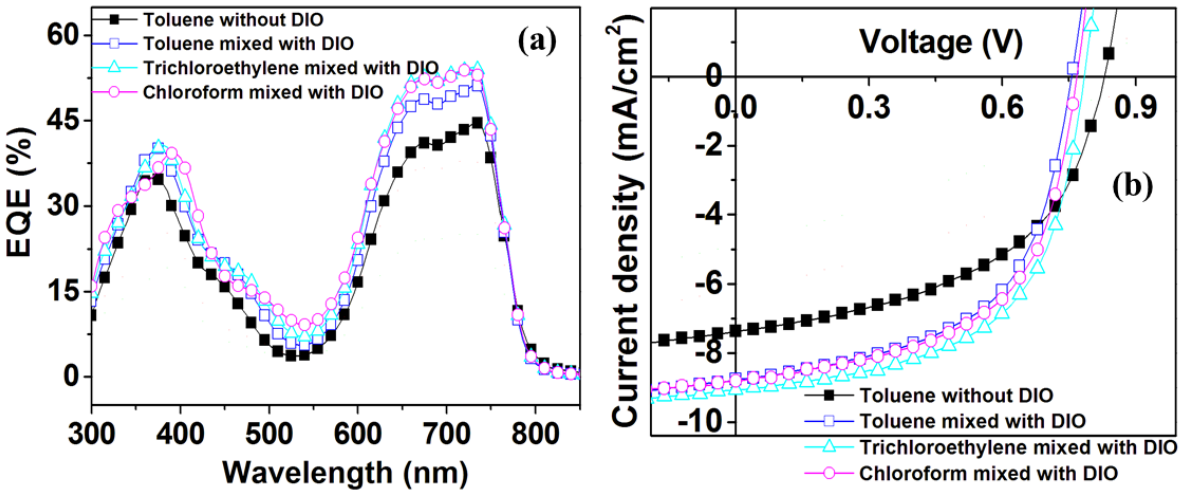

Fig. 2.13. (a) EQE spectra and (b) J-V characteristics of C6PcH$_2$:[60]PCBM BHJ OSCs with various primary solvents.

Table 2.7. Cell characteristics of the C6PcH$_2$:[60]PCBM BHJ OSCs with the different primary solvent mixed with 0.2% v/v of DIO under AM 1.5G illumination at an intensity of 100 mW/cm^2.

Primary solvents	Processing additives	J_{sc} (mA/cm^2)	V_{oc} (V)	*FF*	η (%)
Toluene	None	7.4	0.83	0.50	3.1
Toluene	0.2% DIO	8.8	0.75	0.56	3.7
Trichloroethylene	0.2% DIO	9.1	0.78	0.58	4.1
Chloroform	0.2% DIO	8.8	0.77	0.58	3.9

The $C6PcH_2$:[60]PCBM devices without DIO in toluene showed the EQE of 44% at the Q-band of $C6PcH_2$ and the PCEs of 3.1% with J_{sc} of 7.4 mA/cm^2, V_{oc} of 0.83 V, and *FF* of 0.50. The devices utilizing toluene as the primary solvents showed the higher photovoltaic performance, compared with the devices using chloroform or trichloroethylene as primary solvents (not shown here) due to the high toluene-solvent-induced crystallization of discotic $C6PcH_2$ [64]. By utilizing DIO as a processing additive to modify the nanoscale phase separation and crystallinity, the photovoltaic performance of all devices was improved. Particularly, by utilizing trichloroethylene mixed with 0.2% v/v DIO, the EQE was improved from 38% to 54% at the Q-band and the PCE increased to 4.1% with the J_{sc} of 9.1 mA/cm^2, V_{oc} of 0.78 V, and *FF* of 0.58. Although more efforts should be made to understand the roles of primary solvents on improvement of the photovoltaic properties, it is suggested that the higher photovoltaic performance of devices utilizing trichloroethylene mixed with 0.2% v/v DIO, compared with the devices utilizing chloroform or toluene mixed with 0.2% v/v DIO was probably due to the high uniformity of surface morphology as the aforementioned describe in the AFM images of surface of composite thin films [65, 66].

Figure 2.14 shows the EQE and J-V characteristics of $C6PcH_2$:[60]PCBM devices with the various processing additives in an ITO/MoOx/BHJ/LiF/Al structure under AM 1.5G illumination at an intensity of 100 mW/cm^2. The cell characteristics for all devices are summarized in Table 2.8. Herein, chloroform was utilized as the primary solvent.

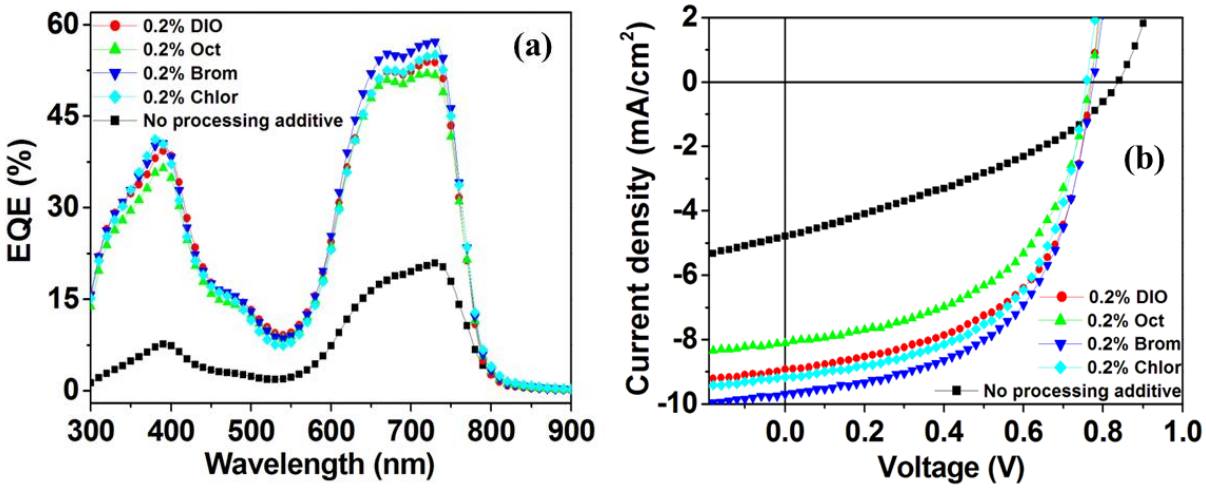

Fig. 2.14. (a) EQE spectra and (b) J-V characteristics of $C6PcH_2$:[60]PCBM BHJ OSCs with various processing additives.

Table 2.8. Cell characteristics of the $C6PcH_2$:[60]PCBM BHJ OSCs with different processing additives mixed with chloroform under AM 1.5G illumination at an intensity of 100 mW/cm^2.

Processing additives	J_{sc} (mA/cm^2)	V_{oc} (V)	*FF*	η (%)
None	4.8	0.84	0.35	1.4
0.2% DIO	8.9	0.77	0.55	3.8
0.2% Oct	8.1	0.77	0.53	3.3
0.2% Brom	9.7	0.78	0.56	4.2
0.2% Chlor	9.2	0.76	0.56	3.9

It is found that except for the Oct-containing solution, by incorporating a processing additive up to a volume of a few volume percent, the performance of the BHJ OSCs was markedly improved. In particular, by adding 0.2% v/v Brom to chloroform solution, the EQE at the Q-band was improved from 21% to 57%, and J_{sc} and PCE increased to 9.7 mA/cm^2 and 4.2%, respectively. The relatively low performance of the cell utilizing Oct solvent as a processing additive might have resulted from the slight decrease in the Davydov splitting at the Q-band of the absorbance spectrum and the low crytallinity, as shown in the XRD patterns. Obviously, the nanoscale phase separation and the crystallization of the BHJ materials were clearly optimized and the performance of the BHJ OSCs was markedly improved by utilizing various processing additives [67].

2.6 Conclusions

The effects of processing additives on the nanoscale phase separation, crystallization, and photovoltaic performance of the BHJ OSCs utilized discotic $C6PcH_2$ mixed with [60]PCBM were studied. By incorporating processing additives to a volume of a few percent, the separation of donor and acceptor phases in $C6PcH_2$:PCBM thin films, which was discussed by taking the Davydov splitting at the Q-band of the absorbance spectra and the surface nanomorphology into consideration, was improved. It was proposed that the separation of donor and acceptor phases was promoted due to the higher boiling point of the processing additives, compared with that of the primary solvents and the different solubility of [60]PCBM and $C6PcH_2$ in processing additives. Furthermore, the crystallization of discotic $C6PcH_2$ in hexagonal structures has been improved by using processing additives. It was suggested that the improved crystallization was probably due to increases in the solubility of $C6PcH_2$ in processing additives.

Moreover, the effects of the processing-additive induced donor-acceptor phase separation and the

processing-additive induced crystallization of the BHJ materials on the photovoltaic properties of the BHJ OSCs utilized discotic $C6PcH_2$ mixed with [60]PCBM were reported. Particularly, without DIO [60]PCBM molecules were dispersed between $C6PcH_2$ domains during spin-cast processing, resulted in deteriorating the crystallization of $C6PcH_2$ domains. As a result, the transportation of both electrons and holes to electrodes were degraded and the photovoltaic performance of the BHJ OSCs was poor.

By adding small amount of DIO to the BHJ blend solutions, [60]PCBM was separated from the $C6PcH_2$ domains and the crystallization of $C6PcH_2$ molecules in the hexagonal structures was improved. As a result, the continuous pathways for the transportation of charge carrier to electrodes were extended and the photovoltaic performance of the BHJ OSCs was improved. However, by adding 0.8% v/v of DIO to the BHJ blend solutions, the interfacial areas of donor and acceptor phases became smaller and the efficient exciton dissociation was low. This also resulted in the low photovoltaic performance of the BHJ OSCs. The optimum nanoscale phase separation and crystallization of the BHJ materials was probably achieved by adding 0.2% v/v of DIO to the BHJ blend solution.

Although more efforts should be made to understand the roles of primary solvents as well processing additives on the improvement of the photovoltaic properties of the BHJ OSCs utilized discotic $C6PcH_2$ mixed with [60]PCBM, the nanoscale phase separation and the crystallization of the BHJ materials were clearly optimized and the performance of the BHJ OSCs was markedly improved by utilizing various processing additives mixed with the different primary solvents. In particular, by adding 0.2% v/v of Brom to the solution containing BHJ blends in trichloroethylene, the EQE at the Q-band was improved to 57%, and the PCE increased to 4.2%, with a J_{sc} of 9.7 mA/cm^2, a V_{oc} of 0.76 V, and an *FF* of 0.56.

Chapter 3

Roles of fullerene derivatives in photovoltaic properties of solar cells

3.1 Introduction

As described in Chapter 2, by utilizing processing additives, the $C6PcH_2$:[60]PCBM based BHJ OSCs showed the relatively high PCE of 4.2% and EQE at Q band of phthalocyanine close to 60% with the optimum donor-acceptor phase separation and crystallization of the BHJ materials. However, the EQE at around 500 nm was limited due to the low absorption of both $C6PcH_2$ molecules and [60]PCBM. When J_{sc} can be estimated from the EQE, as shown in equation (1.4), the low EQE at around 500 nm will reduce the PCE. Thus, the improvement of the EQE at around 500 nm becomes one major challenge for the BHJ OSCs utilizing $C6PcH_2$.

Moreover, one found that during spin-cast processing, [60]PCBM molecules were dispersed between $C6PcH_2$ domains, resulted in the deterioration of crystallization of discotic $C6PcH_2$ in the hexagonal structures. The deterioration of crystallization of the BHJ materials caused the poor transportation of both electrons and holes to electrodes and the poor photovoltaic performance of the BHJ OSCs. In terms of BHJ OSCs, One found that the balance between a large interfacial area and continuous pathways for carrier transportation and/or the optimum nanoscale morphology are necessary for the high photovoltaic performance [46]. Recent significant progresses to control nanoscale morphology in BHJ OSCs have been made by optimization of the device preparation conditions, including the adjustment of the volume fractions of the components, thermal annealing treatment, and processing additives [19, 21, 47]. Although the application of thermal annealing treatment and processing additives to optimize the donor-acceptor phase separation and crystallization of the $C6PcH_2$:[60]PCBM BHJ materials have been described in the previous chapters, the effects of the BHJ blend ratios on photovoltaic properties of BHJ OSCs utilizing $C6PcH_2$ were not yet concerned.

In this chapter, the roles of fullerene derivatives in the photovoltaic properties of the BHJ OSCs utilizing $C6PcH_2$ were studied. By using various fullerene derivatives, the EQE at around 500 nm and the photovoltaic performance was improved. Furthermore, the effects of blend ratios on the photovoltaic properties of BHJ OSCs utilizing $C6PcH_2$ were also discussed.

3.2 Experimental Procedure

$C6PcH_2$ was synthesized as described in the literature [55], with slight modifications, and fully purified by column chromatography (using silica gel with toluene as the eluent), which was followed by repeated recrystallization from toluene-methanol (1:2) solution [9]. The fullerene derivatives, such as [60]PCBM, [70]PCBM, and bis-adduct of [60]PCBM (Bis[60]PCBM), as shown in Fig. 3.1, were purchased from Frontier Carbon Ltd.

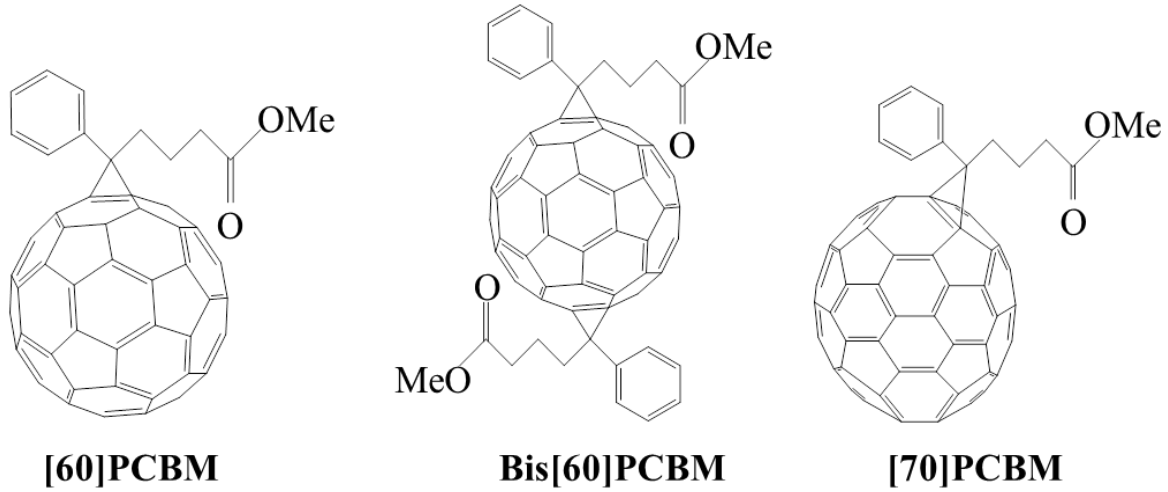

Fig. 3.1. Chemical structure of fullerene derivatives in this study.

BHJ thin films were prepared under optimized conditions in accordance with the following procedure. An ITO-coated quartz substrate was cleaned with detergent, ultrasonicated in water, chloroform, acetone, and isopropyl alcohol, and subsequently dried with UV-induced ozone. 6-nm-thick MoO_x films were thermally evaporated onto ITO at a rate of 0.1 Å/s under a vacuum of about 2×10^{-5} Pa. After transferring the films to a N_2-filled glove box, a solution containing a mixture of $C6PcH_2$ and various fullerene derivatives (3:2) in chloroform mixed with DIO was stirred using an ultrasonic washer and spin-cast at 2000 rpm onto a MoO_x layer. Herein, DIO plays a key role as a processing-additive solvent to control nanoscale morphology of BHJ active layer. Otherwise, $C6PcH_2$:[70]PCBM BHJ thin films with various blend ratios have been fabricated. The concentration of the BHJ solution was 22.35 mg/ml, and the active layer thickness was approximately 130 nm. Finally, a 0.3-nm-thick LiF buffer layer and an 80-nm-thick aluminum layer were deposited through a shadow mask by thermal evaporation under a vacuum of about 2×10^{-5} Pa. The active area of the device was 4 mm^2.

The device characteristic was measured under irradiation intensity of 100 mW/cm^2 using an XES 301 (AM 1.5 G) full spectrum solar simulator. The *J-V* characteristics were measured using a source

measurement unit (Keithley 2400). Otherwise, EQE spectra were measured with a programmable electrometer using Xe lamp light passed through a monochromator as a light source. The integrated EQE values always showed good agreement with the measured valued of J_{sc}. The absorbance spectra, PL spectra were measured by spectrophotometry (Shimadzu UV-3150), using a fluorescence spectrophotometer (F-4500). Furthermore, the crystallinity of the $C6PcH_2$ molecules in thin films was evaluated by XRD (Rigaku RINT 2000).

3.3 Improving the photovoltaic performance using various fullerene derivatives

The absorption spectra of the [70]PCBM and $C6PcH_2$:[70]PCBM composite thin films fabricated on quartz substrates are shown in Fig. 3.2, along with those of [60]PCBM. Although [60]PCBM accounts for 40% of the weight of the photoactive layers, the absorption spectrum of the $C6PcH_2$:[60]PCBM composite thin film showed strong peaks at the Q-band and B-band of $C6PcH_2$ molecules and weak absorption at around 500 nm. The low absorption of C_{60} fullerene derivatives is attributed to their high degree of symmetry, making the lowest-energy transitions formally dipole forbidden [68]. Therefore, when the C_{60} moiety of [60]PCBM is replaced by a less symmetrical fullerene, these transitions become allowed and the absorption dramatically increases [68-71]. By employing asymmetric [70]PCBM fullerene derivatives with $C6PcH_2$ instead of [60]PCBM, the absorption of the composite thin films at around 500 nm markedly increased due to the optical transitions in the visible region of C_{70} molecules.

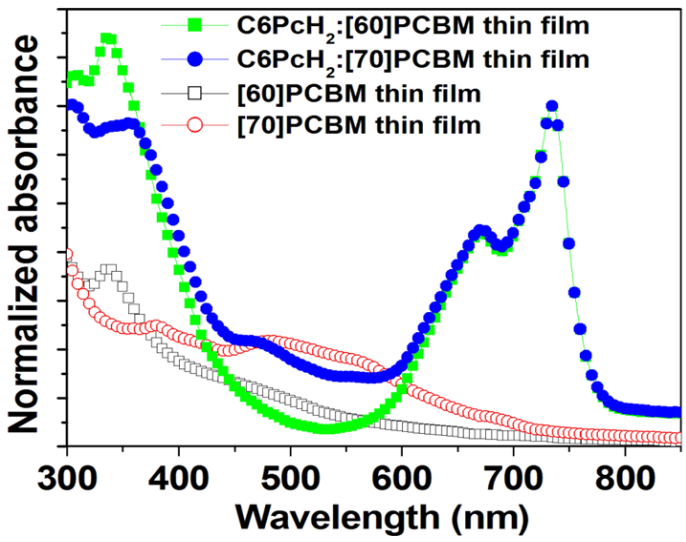

Fig. 3.2. Absorbance spectra of the $C6PcH_2$:[70]PCBM and $C6PcH_2$:[60]PCBM composite thin films. Absorbance spectra were normalized at 730 nm.

Figure 3.3 shows the XRD patterns of composite thin films with various fullerene derivatives fabricated on glass substrates. It can be seen that the diffraction peak of $C6PcH_2$ thin film appeared at approximately 4.86º, which corresponds to the intercolumnar distance in a hexagonal structure of 18.2 Å. The dependences of the FWHM of XRD peaks upon adding fullerenes are shown in Table 3.1. An increase in the FWHM upon adding fullerenes indicated that the crystallinity of the discotic $C6PcH_2$ columns in hexagonal structures was lowered owing to the dispersion of the fullerene molecules into the $C6PcH_2$ domains, which were in good agreement with the proposed models in the chapter 2 [66, 67]. Although increases in the FWHM of the XRD peaks or decreases in the crystallinity of the discotic $C6PcH_2$ columns in hexagonal structures occurred in all of the composite thin films, the addition of [70]PCBM and Bis[60]PCBM to the composite thin films resulted in the lower crystallinity than those of the [60]PCBM acceptors.

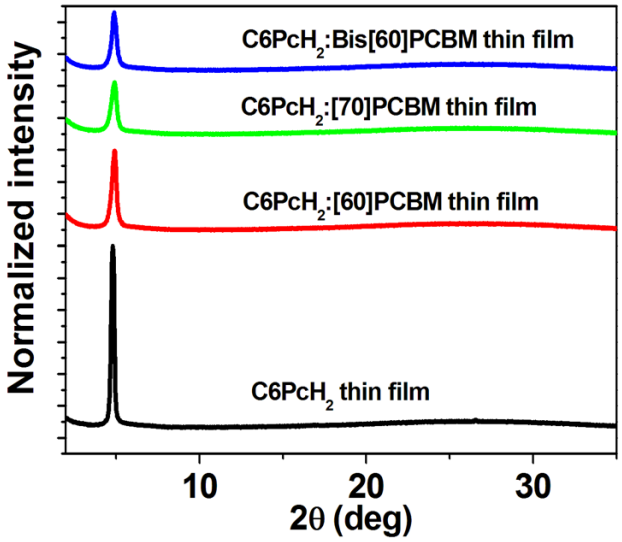

Fig. 3.3. XRD patterns of the composite thin films with various fullerene derivatives. All XRD patterns were normalized at 4.88º.

Table 3.1. FWHMs of XRD peaks of composite thin films with various fullerene derivatives.

	$C6PcH_2$ thin films	$C6PcH_2$:[60]PCBM thin films	$C6PcH_2$:[70]PCBM thin films	$C6PcH_2$:Bis[60]PCBM thin films
FWHM	0.23º	0.36º	0.45º	0.40º

Figure 3.4 shows the EQE and J-V characteristics of the BHJ OSCs utilizing $C6PcH_2$ mixed with the various fullerene derivatives in an ITO/MoO_x/BHJ/LiF/Al structure under AM 1.5G illumination at an intensity of 100 mW/cm^2. The cell characteristics for all devices are summarized in Table 3.2. The $C6PcH_2$:[60]PCBM devices showed the EQE of 53% and 8% at the Q-band and around 500 nm,

respectively. As a result of the high EQE, the J_{sc}, as shown in Fig. 3.4(b), was measured to be 8.1 mA/cm^2. The V_{oc} was 0.76 V, and the PCE was estimated to be 3.7%. By employing an asymmetric [70]PCBM fullerene derivative with $C6PcH_2$ instead of [60]PCBM, the EQE at around 500 nm was improved from 8% to 24%, which was in good agreement with the absorption spectra. Although the EQE at the Q-band was slightly decreased, which can be attributed to the relatively low crystallinity of $C6PcH_2$ in the $C6PcH_2$:[70]PCBM composite thin films, J_{sc} and the PCE were markedly improved to 10.2 mA/cm^2 and 3.9%, respectively.

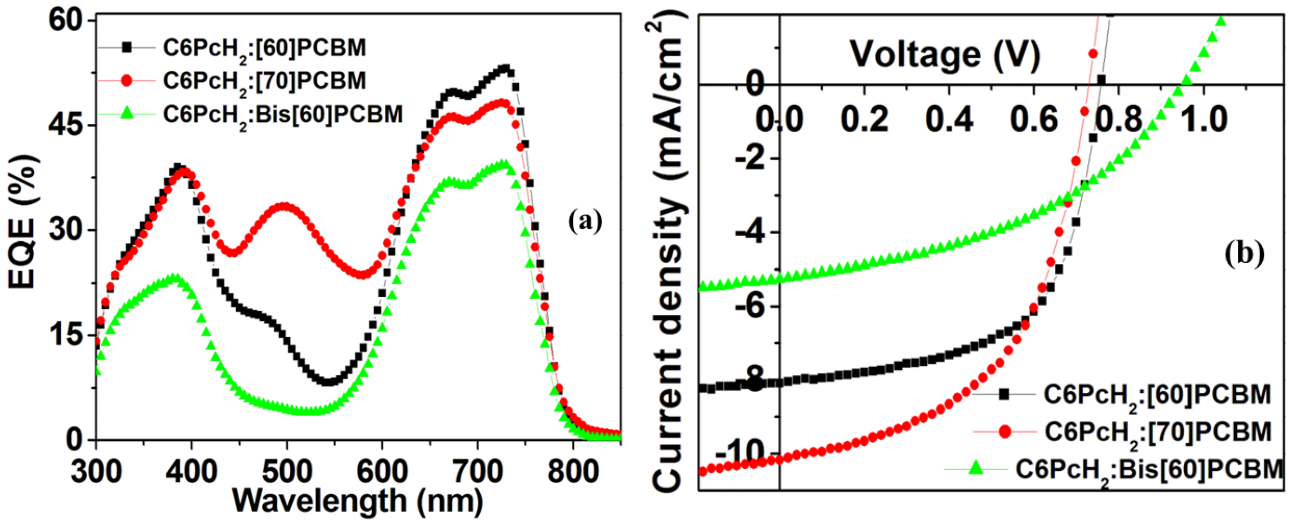

Fig. 3.4. (a) EQE spectra and (b) J-V characteristics of the BHJ OSCs with various fullerene derivatives.

Table 3.2. Cell characteristics of the BHJ OSCs utilizing $C6PcH_2$ mixed with various fullerene derivatives under AM 1.5G illumination at an intensity of 100 mW/cm^2.

	J_{sc} (mA/cm^2)	V_{oc} (V)	*FF*	η (%)
$C6PcH_2$:[60]PCBM BHJ OSCs	8.1	0.76	0.60	3.7
$C6PcH_2$:[70]PCBM BHJ OSCs	10.2	0.73	0.53	3.9
$C6PcH_2$:Bis[60]PCBM BHJ OSCs	5.3	0.96	0.42	2.1

The essential parameters that determine the PCE of BHJ OSCs are V_{oc}, *FF*, and J_{sc}. The maximum V_{oc} is considered to be limited by the work function of the metal electrodes and the energy

gap between the HOMO of the donor materials and the lowest unoccupied molecular orbital (LUMO) of the acceptor fullerenes (ΔE_{DA}) [70-73]. Although the difference between V_{oc} and ΔE_{DA} is still subject to debate, a linear relationship between V_{oc} and ΔE_{DA} has been experimentally confirmed [73]. By employing Bis[60]PCBM, the LUMO level of which is 0.1-0.2 eV higher than that of [60]PCBM, instead of [60]PCBM, V_{oc} was markedly improved from 0.76 to 0.96 V, as shown in Table 3.2 [74]. However, the Bis[60]PCBM:C6PcH$_2$ solar cells had a relatively low J_{sc} of 5.27 mA/cm^2. It was suggested that this result is attributed to the decrease in the energy gap between the LUMO levels of the donor and acceptor, which directly corresponds to the efficiency of the photoinduced charge separation [75].

Figure 3.5 shows the PL spectra of composite thin films with various fullerene derivatives fabricated on quartz substrates. The PL spectra of C6PcH$_2$ thin films exhibited a predominant peak at 766 nm and a shoulder at around 820 nm, which is related to the Q-band of the C6PcH$_2$ absorption spectrum [63]. The PL intensity was drastically suppressed upon adding fullerene derivatives, such as Bis[60]PCBM, [70]PCBM, and [60]PCBM, owing to photoinduced electron transfer from the excited state of C6PcH$_2$ to the fullerene derivative acceptor [1-4]. It was found that the PL quenching of C6PcH$_2$:[60]PCBM or C6PcH$_2$:[70]PCBM composite thin films was more marked than that of C6PcH$_2$:Bis[60]PCBM composite thin films. This result suggested that the energy gap between the LUMO levels of the donor and acceptor was reduced by employing Bis[60]PCBM with C6PcH$_2$ instead of [60]PCBM or [70]PCBM, which is consistent with the *J-V* characteristics.

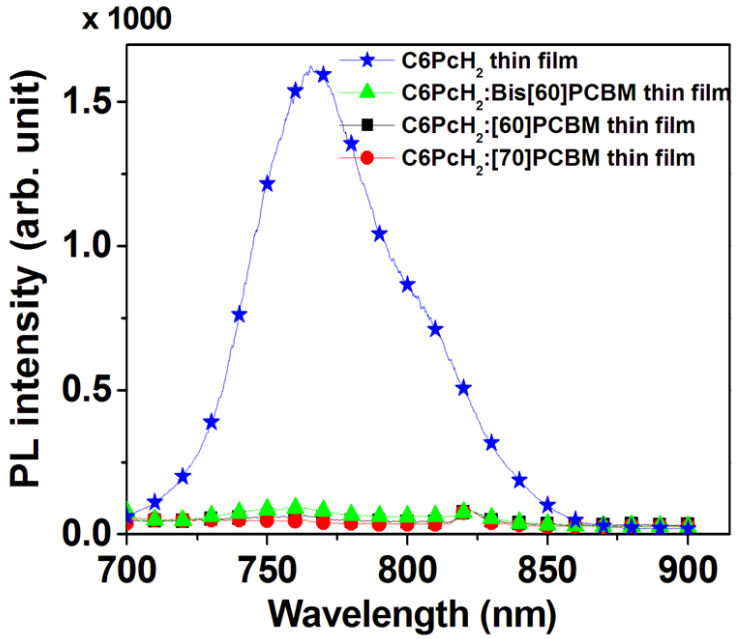

Fig. 3.5. PL spectra of the composite thin films; the excitation wavelength is 670 nm.

3.4 Blend ratio dependences of photovoltaic properties

Figure 3.6 shows the absorbance spectra of the C6PcH$_2$:[70]PCBM composite thin films with the various blend ratios fabricated on quartz substrates. Obviously, the visible-region absorption spectra consisted of a strong Q-band and a B-band of C6PcH$_2$ molecules, and a shoulder around 500 nm of [70]PCBM. By increasing the [70]PCBM volume fractions, the absorbance around 500 nm was improved, but the absorbance at the Q band of C6PcH$_2$ molecules was reduced.

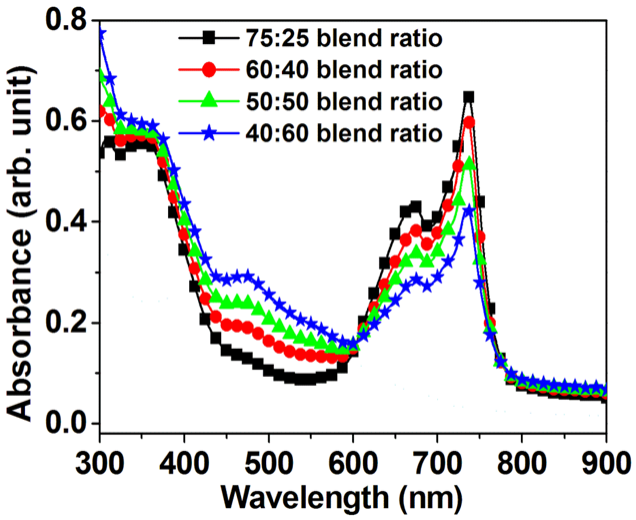

Fig. 3.6. absorbance spectra of the C6PcH$_2$:[70]PCBM composite thin films with the various blend ratios.

One found that the increases in [70]PCBM volume fractions did not only affect to the absorption intensities but also the Davydov splitting at Q-band of C6PcH$_2$ molecules and/or the molecular interaction of discotic C6PcH$_2$ in the hexagonal structures. The dependence of the Davydov splitting at Q-band of C6PcH$_2$ molecules on the blend ratios is shown in Fig. 3.7. It exhibited that the width of Davydov splitting was drastically reduced upon increasing the [70]PCBM volume fractions. When the width of Davydov splitting in an allowed electronic transition is corresponding to the interaction energy between molecules with different site symmetries [59, 60], the decreases in Davydov splitting indicated that the molecular interaction of discotic C6PcH$_2$ with the hexagonal structures was weakened owing to the dispersion of [70]PCBM into the C6PcH$_2$ domains during the spin-cast processing, which were in good agreement with the proposed models in the chapter 2.

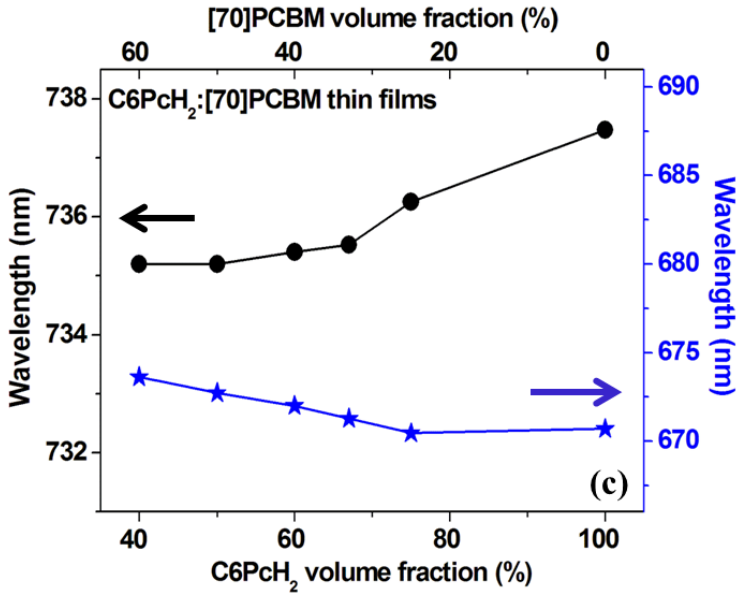

Fig. 3.7. Blend ratio dependences of the Davydov splitting at Q-band.

Figure 3.8 shows the XRD patterns of $C6PcH_2$ and $C6PcH_2$:[70]PCBM composite thin films spin-cast on glass substrates. All the XRD patterns exhibited the similar shapes and consisted of the only diffraction peak at approximately 4.88º, corresponding to Miller indices of (200)/(110) (using indices based on a rectangular cell). Moreover, the intercolumnar distance of discotic $C6PcH_2$ in the hexagonal structures was estimated to be 18.1 Å.

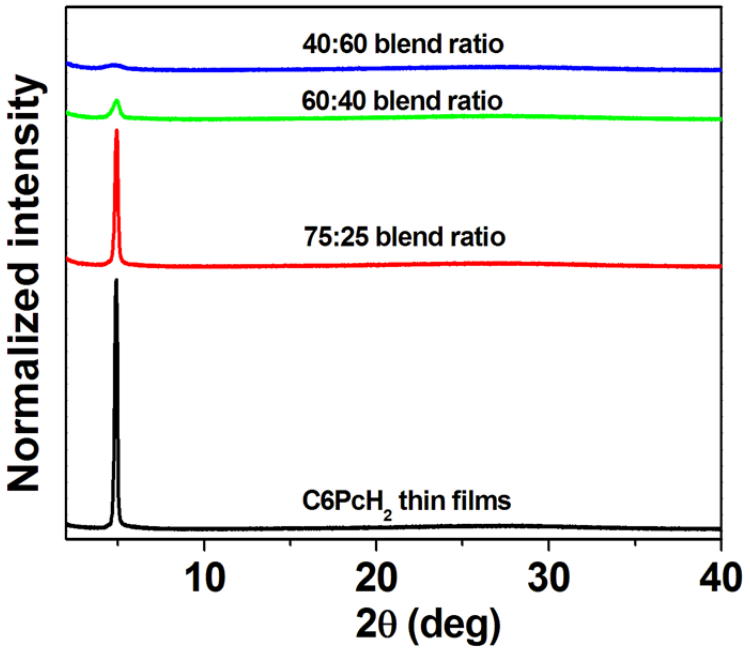

Fig. 3.8 XRD patterns of $C6PcH_2$ and $C6PcH_2$:[70]PCBM composite thin films with various the blend ratios. All XRD patterns were normalized at 4.88º.

Table 3.3. FWHM of XRD pattern of $C6PcH_2$ and $C6PcH_2$:[70]PCBM composite thin film with the various blend ratios.

	$C6PcH_2$ thin films	$C6PcH_2$:[70]PCBM thin films with various blend ratios			
		75:25	67:33	60:40	50:50
FWHM	0.18º	0.2º	0.3º	0.54º	1.16º

Furthermore, the FWHM of the XRD patterns with the different [70]PCBM volume fraction are summarized in Table 3.3. One found that the FWHM was drastically enlarged upon increasing the [70]PCBM volume fractions. Particularly, by increasing the [70]PCBM volume fraction to 50%, the FWHM of the XRD patterns were extended from 0.2 to 1.16º. When FWHM of XRD pattern is directly corresponding to crystallization of molecules, increases in the FWHM of thin film XRD patterns upon adding [70]PCBM indicated that the crystallization of discotic $C6PcH_2$ with hexagonal structures was reduced owing to the dispersion of PCBM into the $C6PcH_2$ domains, which was in good agreement with the aforementioned decreases in Davydov splitting.

Although by employing an asymmetric [70]PCBM fullerene derivative instead of [60]PCBM, EQE at around 500 nm was improved due to the strong absorption of [70]PCBM [68], the clear peaks of EQE at around 500 nm, corresponding to [70]PCBM was not yet observed. Figure 3.9 shows the EQE spectra and the J-V characteristics under AM 1.5G illumination at an intensity of 100 mW/cm^2 of $C6PcH_2$:[70]PCBM BHJ OSCs with the various blend ratios in an ITO/MoO_x/BHJ/LiF/Al structure. The cell characteristics for all devices are summarized in Table 3.4. The EQE spectra exhibited the peaks corresponding to strong Q-band and B-band of $C6PcH_2$, and a clear peak around 500 nm of [70]PCBM. The clear peak at around 500 nm, furthermore, indicated that the photogenerated excitons of both the donor materials and the acceptor materials attributed to the photovoltaic performance.

Moreover, by increasing [70]PCBM volume fraction, the EQE at Q-band was improved to be around 53%. As a result, the J_{sc} increased to 10.2 mA/cm^2, when the ratio of $C6PcH_2$ to [70]PCBM was 60 to 40. With the V_{oc} of 0.73 V, the PCE was estimated to be 3.9%. We suggested that the interfacial areas between donor and acceptor was enlarged by increasing volume fraction of [70]PCBM in composite thin films, resulting in the improved photovoltaic performance.

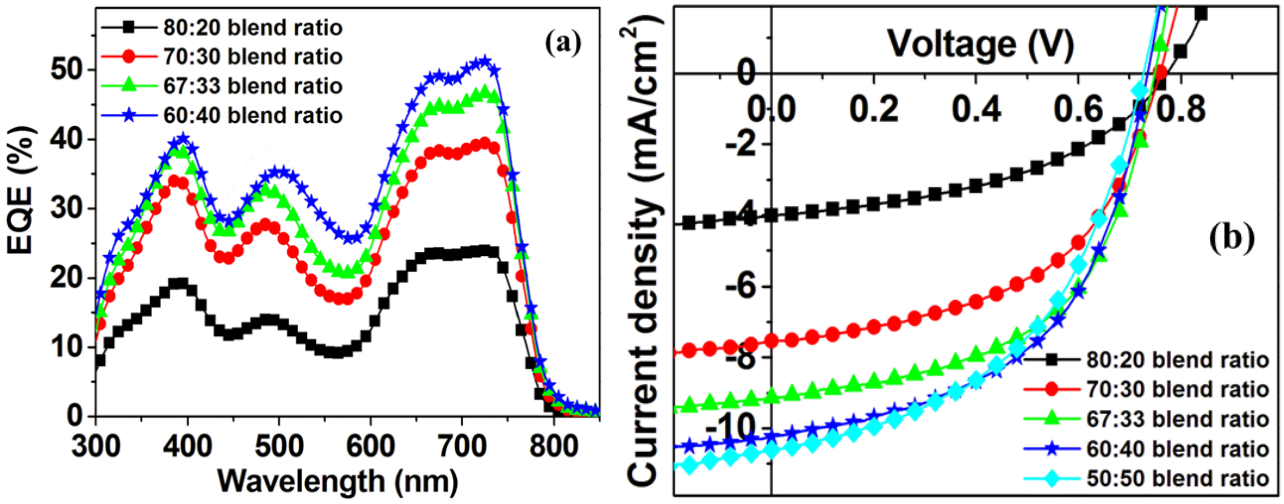

Fig. 3.9. (a) EQE spectra and (b) J-V characteristics of the C6PcH$_2$:[70]PCBM BHJ OSCs with various blend ratios.

Table 3.4. Cell characteristics of the C6PcH$_2$:[70]PCBM BHJ OSCs with various blend ratios under AM 1.5G illumination at an intensity of 100 mW/cm^2.

C6PcH$_2$:[70]PCBM blend ratios	J_{sc} (mA/cm^2)	V_{oc} (V)	*FF*	η (%)
80:20	4.0	0.77	0.45	1.4
70:30	7.5	0.76	0.51	3.0
67:33	9.1	0.75	0.54	3.7
60:40	10.2	0.73	0.52	3.9
50:50	10.6	0.73	0.48	3.7

The PL spectra of C6PcH$_2$ and C6PcH$_2$:[70]PCBM thin films fabricated on quartz substrates with the various blend ratios are shown in Fig. 3.10(a). The PL spectra of C6PcH$_2$ thin films had a predominant peak at 766 nm and a shoulder around 820 nm, which relate with the Q-band of the C6PcH$_2$ absorption spectra [63]. The PL intensity of C6PcH$_2$:[70]PCBM thin films was markedly suppressed depending on [70]PCBM blend ratio. This suppression was due to the nonradiative decay of photogenerated-excitons through the photoinduced-electron transfer from the excited state of C6PcH$_2$ to [70]PCBM [1-4]. Moreover, *Q* was strong dependent on the [70]PCBM volume fraction, as shown in Fig. 3.10(b). The increases in *Q* indicated that the interfacial areas between donor and acceptor was enlarged by increasing the [70]PCBM volume fraction, which was in good agreement with the aforementioned increases in the J_{sc} and PCE.

Although the J_{sc} and PCE of the OSCs utilizing $C6PcH_2$ mixed with [70]PCBM was improved with increasing the volume fraction of [70]PCBM, the *FF* was reduced when the [70]PCBM volume fraction was higher than 33%. As shown in Table 3.4, the *FF* decreased to 0.48, which caused the relatively low PCE of 3.7%, when the ratio of $C6PcH_2$ to [70]PCBM was 50 to 50. It was supposed that with the high volume fraction of [70]PCBM, crystallinity of $C6PcH_2$ molecules was reduced and the continuous pathways for the transportation of charge carriers to electrodes were deteriorated.

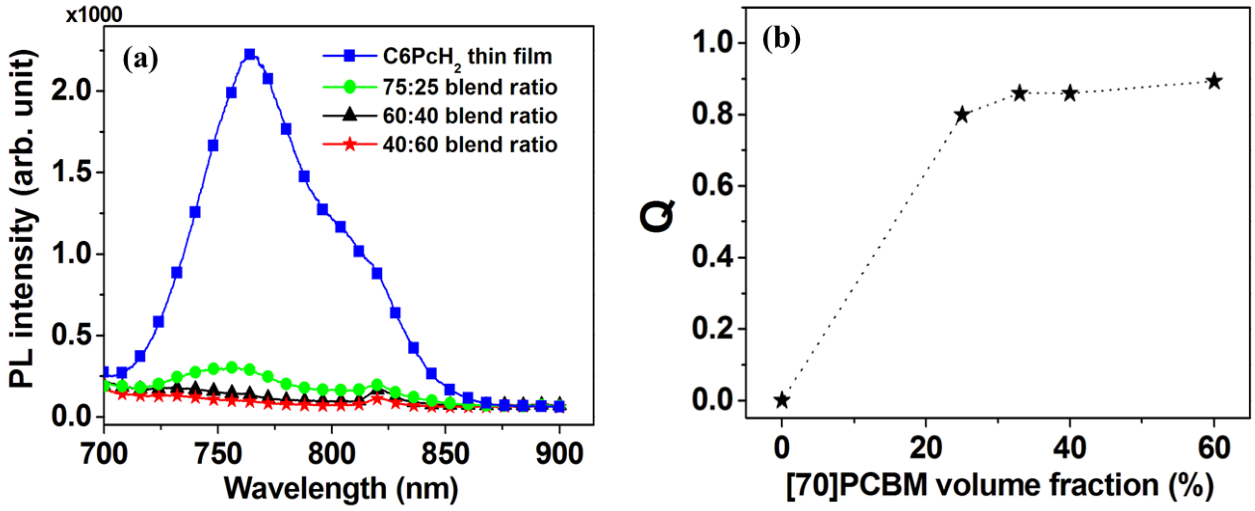

Fig. 3.10. (a) PL spectra of $C6PcH_2$ and $C6PcH_2$:[70]PCBM composite thin films with the various blend ratios and (b) Dependence of the relative quenching efficiency on the blend ratios; the excitation wavelength is 670 nm;

3.4 Conclusions

In this chapter, the roles of fullerene derivatives in the photovoltaic properties of the BHJ OSCs utilizing $C6PcH_2$ were studied. The photovoltaic performance of $C6PcH_2$-based BHJ OSCs was improved by using various fullerene derivatives, such as [60]PCBM, [70]PCBM, and Bis[60]PCBM. Particularly, by replacing the C_{60} moiety of [60]PCBM with the asymmetric C_{70}, the absorption of composite thin films at around 500 nm increased, the EQE of the solar cells at around 500 nm was improved from 8% to 24%, and J_{sc} increased to 10.2 mA/cm^2. On the other hand, a high V_{oc} of 0.96 V was attained using Bis[60]PCBM with a higher LUMO level. Although the addition of [70]PCBM or Bis[60]PCBM to the composite thin films resulted in a lower crystallinity than that in case of the [60]PCBM, the photovoltaic performance of the BHJ OSCs utilizing [70]PCBM and Bis[60]PCBM fullerene derivatives was markedly improved.

Moreover, the blend ratio dependence of the photovoltaic properties in BHJ OSCs utilizing

$C6PcH_2$ mixed with [70]PCBM was reported. With increasing the volume fraction of [70]PCBM, the J_{sc} was improved to 10.6 mA/cm^2 due to enlarging the donor and acceptor interfacial areas. On the other hand, when the [70]PCBM volume fraction was higher than 33%, the *FF* was reduced owning to deteriorating crystallization of discotic $C6PcH_2$ molecules with hexagonal structures, which was in good agreement with the results of absorption spectra and XRD patterns. The OSCs with the optimum blend ratio showed the high PCE of 3.9%.

Chapter 4

Alkyl substituent length dependence of photovoltaic performance of solar cells

4.1 Introduction

During the recent interest in organic electronic devices such as organic thin-film transistors, organic light emitting diodes and OSCs, liquid crystals have attracted much attention as a novel type of molecular semiconductors [8, 76]. Indeed, high carrier mobilities have been realized even in mesophases where the mesogenic molecules are fluctuating with orientational or/and positional order. Typical structures of mesogenic molecules are of ‘‘rod-like’’ and ‘‘disk-like’’ types which are known as calamitic and discotic liquid crystals, respectively [77].

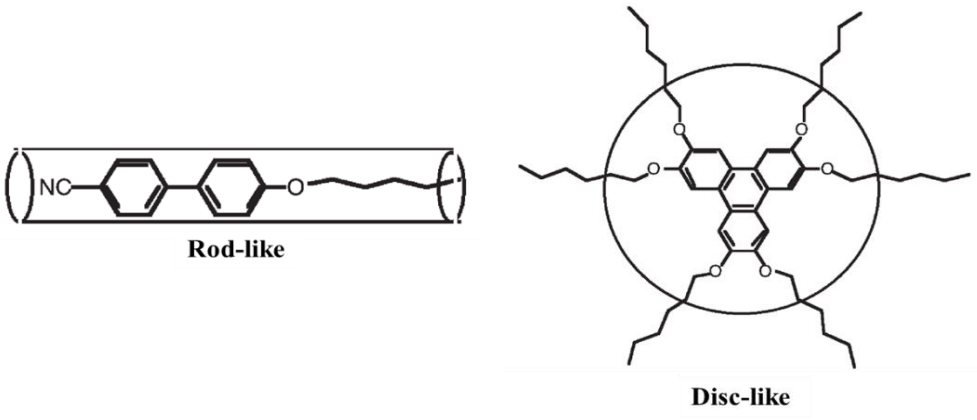

Fig. 4.1. Typical shapes of molecules for calmaitic and discotic liquid crystals.

The mesogenic molecule consists of a rigid core with, in most cases, a π-electronic conjugation system and alkyl tails/substituents in the terminal/peripheral positions for calamitic/discotic liquid crystals, respectively, as illustrated in Fig. 4.1. The π-electronic systems being core parts of the mesogenic molecules play an important role for electronic conduction. On the other hand, the flexible parts of molecules definitively play an important role for the self-assembling nature. The self-organization is reasonably expected to facilitate the easy formation of a large-area mono-domain film with uniform alignment of molecules through their characteristic orientational order. In addition, on the basis of the requirement for ‘‘wet processing’’ in thin film device fabrication, the flexible parts of molecules have made such alkylated π-electronic conjugation systems much more attractive

due to their good solubility in common organic solvents [77].

On the history of liquid crystalline semiconductors, discotic liquid crystals opened up the doors to the present status of research, and this was initiated by the collaborative works between Bayreuth and Mainz in Germany. They found that typical discotic mesogens, hexaalkylthio and hexaalkyloxy-triphenylenes, show fast mobilities of charge carriers in the columnar mesophases of 10^{-1} and 10^{-3} cm^2/Vs, respectively [78]. In particular, the former reaches the mobility range exhibited by a-silicon. Nevertheless, it is surprising to see that such a high mobility of charge carriers could be realized in a medium in which the molecules are likely to fluctuate within a limited framework (orientational/positional order). This fast mobility in mesophases is interpreted as an electronic process of charge transport by carrier hopping among the molecules and the disordered model proposed by Bassler is often used for understanding the characteristic properties observed so far [79]. Although, many reports have been published on liquid crystalline semiconductors in recent years, not so many compounds have been investigated so far as BHJ OSCs for example, and most did not exhibit the expected properties resulting from drift mobility measurements [80, 81].

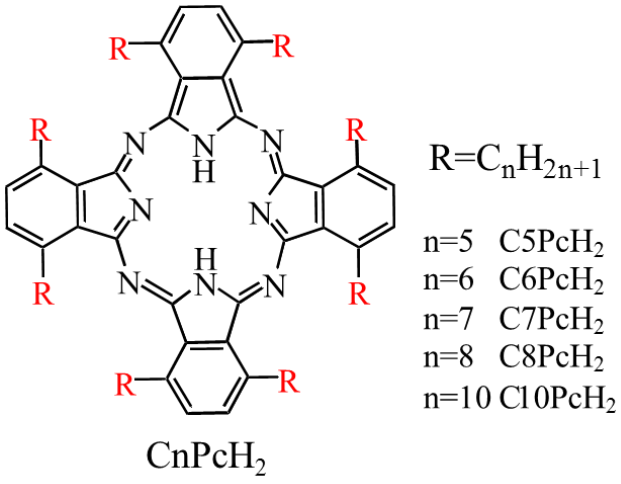

Fig. 4.2. Molecular structure of $CnPcH_2$ in this study.

As we described in the previous chapters, $C6PcH_2$ exhibits the high hole and electron drift mobilities in the crystalline phase at room temperature and the BHJ OSCs based on $C6PcH_2$ mixed in various fullerene derivatives exhibited the relatively high PCEs [67, 70]. Although, the octaalkylphthalocyanine ($CnPcH_2$) with different alkyl substituents were described as potential donors for BHJ OSCs, roles of the alkyl substituents in the self-assembling, optical and electronic properties of $CnPcH_2$ were not fully understood yet [82]. In this study, the dependences of optical and electronic properties, structures, and photovoltaic performance of BHJ OSCs utilizing $CnPcH_2$ (with n are 5, 6, 7, 8 and 10), as shown in Fig. 4.2, mixed with [70]PCBM on the length of alkyl

substituents were reported.

4.2 Experimental Procedure

$CnPcH_2$ was synthesized as described in the literature [55], with slight modifications, and fully purified by column chromatography (using silica gel with toluene as the eluent), which was followed by repeated recrystallization from toluene-methanol (1:2) solution [9]. The fullerene derivatives, [70]PCBM were purchased from Frontier Carbon Ltd.

BHJ thin films were prepared under optimized conditions in accordance with the following procedure. An ITO-coated glass substrate was cleaned with detergent, ultrasonicated in water, chloroform, acetone, and isopropyl alcohol, and subsequently dried with UV-induced ozone. 6-nm-thick MoO_x films were thermally evaporated onto ITO substrates at a rate of 0.1 Å/s under a vacuum of about 2×10^{-5} Pa. After transferring the films to a N_2-filled glove box, a solution containing a mixture of $CnPcH_2$ and [70]PCBM (3:2) in chloroform with the addition of 0.2% v/v of DIO was spin-cast onto a MoO_x layer. Herein, DIO plays a key role as a processing-additive solvent to control nanoscale morphology of BHJ active layer. The concentration of the BHJ solution was 22.35 mg/ml and the thickness of the active layers was estimated approximately to be 100 ~ 150 nm using AFM. Finally, a 0.3-nm-thick LiF buffer layers and 80-nm-thick aluminum films were deposited through a shadow mask by thermal evaporation under a vacuum of about 2×10^{-5} Pa. The active area of the device was 4 mm^2.

The *J-V* characteristics were measured using a source measurement unit (Keithley; 2400) and an XES 301 (AM 1.5 G) full spectrum solar simulator at an irradiation intensity of 100 mW/cm^2. EQE spectra were measured with a programmable electrometer using xenon lamp light passed through a monochromator as a light source. The integrated EQE values show good agreement with the measured J_{sc}.

The absorption spectra and the XRD patterns of the BHJ thin films were measured using a spectrophotometer (Shimadzu, UV-3150) and an X-ray diffractometer (Rigaku, RINT 2000), respectively. The ionization potentials of $CnPcH_2$ were measured using a photoelectron spectroscopy in air (Riken Keiki, AC-2).

The drift mobility of charge carriers of $CnPcH_2$ was determined under low vacuum by time-of-flight (TOF) technique, as shown in Fig. 4.3 [9]. A sandwich cell, consisting of two ITO-coated glass substrates and a polyimide spacer with thicknesses of a dozen of micrometers, was fabricated. The actual cell gaps were evaluated by an interference technique of light transmittance. Subsequently, $CnPcH_2$ was injected into the sandwich cell in the isotropic phase and naturally cooled

down to room temperature. A DC bias was applied between the electrodes using batteries connected in series, and the sample was irradiated using a Nd:YAG laser (λ: 355 nm, pulse width: 1 ns). Finally, the generated current transits were detected by an oscilloscope (Teledyne LeCroy, HDO4054), and the mobility was calculated according to the equation, $\mu = d^2/tE$, where d, t, and E are the sample thickness, transit time and applied field, respectively.

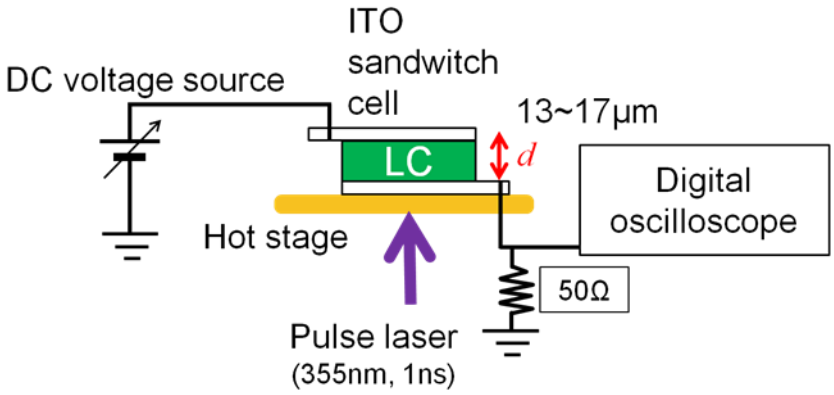

Fig. 4.3. TOF measurement diagram.

4.3 Dependence of optical and electronic properties and structures of $CnPcH_2$ on alkyl substituent length

Figure 4.4 shows absorption spectra at Q-band of $CnPcH_2$ in both solution and solid phases. The absorption spectra of solution of $CnPcH_2$ exhibited intense Q-band absorption arising from the a_{1u}-e_g (π-π^*) transition around 700 and 730 nm and the low intensity transitions to shorter wavelength arising from vibrational fine structure. The dependence of absorption in solution phase of $CnPcH_2$ on the length of alky substituents is insignificant due to the isolated states of the $CnPcH_2$-discotic molecules in solution phases.

In contrast to the solution-phase absorption spectra, the absorption spectra of $CnPcH_2$ thin films were strongly dependent on the alkyl substituent length. Although the Q band of all $CnPcH_2$ thin films was both blue- and red-shifted relative to their solution-phase absorption spectrum with clear Davydov splitting due to the exciton splitting arising from non-equivalent molecules, as in a columnar “herringbone” array of metal-free mesogenic phthalocyanines, the shape of Q-band was markedly modified by controlling the length of alkyl substituents [58]. Particularly, by lengthening the alkyl substituents, the Q-band was enlarged. Moreover, positions of the absorption peaks corresponding to Q-band of $CnPcH_2$ are summarized in Table 4.1. It indicated that by lengthening the alkyl substituents from 5 to 9, the positions of Q_x and Q_y were shifted from 671 and 744 nm to 652 and 781 nm, respectively, and the Davydov splitting increased. When the size of Davydov splitting in

an allowed electronic transition is a direct measure of the interaction energy between molecules with differing site symmetries, one indicated that the alkyl substituents affected the alignment of phthalocyanine-discotic columns in hexagonal structures.

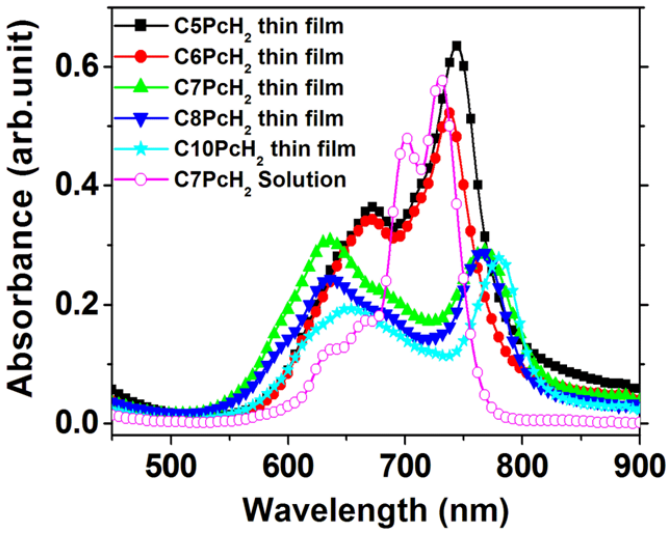

Fig. 4.4. Absorption spectra at Q-band of $C7PcH_2$ in solution phase and $CnPcH_2$ (with n being 5, 6, 7, 8 and 10) in solid.

Table 4.1. Positions of the absorption peaks corresponding to the Q-band of $CnPcH_2$.

	Q_x (nm)	Q_y (nm)
$C7PcH_2$ in solution phase	700	730
$C5PcH_2$ in solid phase	671	744
$C6PcH_2$ in solid phase	670	738
$C7PcH_2$ in solid phase	635	767
$C8PcH_2$ in solid phase	636	765
$C10PcH_2$ in solid phase	652	781

In terms of $CnPcH_2$, the ligands play an important role for electronic conduction and the alkyl substituents definitively attribute to the self-assembling nature [77]. However, when the absorptions of $CnPcH_2$ are strongly dependent on the alkyl substituent length, the electronic band structures of $CnPcH_2$ should be modified by changing the length of alkyl substituents. The photoelectron spectra of $CnPcH_2$ thin films spin-cast on ITO-coated glass substrates are shown in Fig. 4.5 and the HOMO levels of $CnPcH_2$ were estimated and summarized in Table 4.2. Herein, the photoelectron spectra of all $CnPcH_2$ thin films were measured under air ambient. It exhibited that the HOMO levels of $CnPcH_2$ drastically increased by lengthening the alkyl substituents, which was in good agreement

with the aforementioned increases in Davydov splitting. Particularly, while the HOMO levels of $C5PcH_2$ and $C6PcH_2$ were around -5.22 eV, by lengthening the alkyl substituents the HOMO levels of $C7PcH_2$ and $C8PcH_2$ increased to -5.05 and -5.08 eV, respectively.

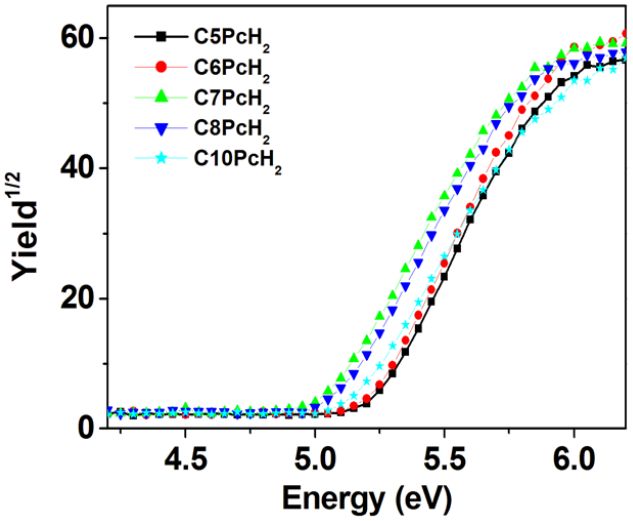

Fig. 4.5. Photoelectron spectrum of $CnPcH_2$.

Table 4.2. HOMO levels of $CnPcH_2$.

	HOMO (eV)
$C5PcH_2$	-5.22
$C6PcH_2$	-5.22
$C7PcH_2$	-5.05
$C8PcH_2$	-5.08
$C10PcH_2$	-5.15

Table 4.3. Intercolumnar distance, D of $CnPcH_2$-discotic columns.

	$C5PcH_2$	$C6PcH_2$	$C7PcH_2$	$C8PcH_2$
D (Å)	17.0	18.1	18.6	19.0

Analysis of structures of $CnPcH_2$, furthermore, was performed using X-ray diffractometer. Figure 4.6 shows the XRD patterns of $CnPcH_2$ thin films spin-cast on glass substrates. The XRD patterns of all $CnPcH_2$ exhibited only the reflections in the small angle regions from 3° to 6°, corresponding to Miller indices of (200)/(110) (using indices based on a rectangular cell). The absence of reflections in the wide-angle region indicates that stacking period of discotic $CnPcH_2$ along columnar axis is

disordered [82]. Moreover, the intercolumnar distance between the axes of neighboring $CnPcH_2$-discotic columns, D was estimated, as shown in Table 4.3. It indicated that D gradually increased from 17.0 to 19.0 Å on changing from $C5PcH_2$ to $C8PcH_2$.

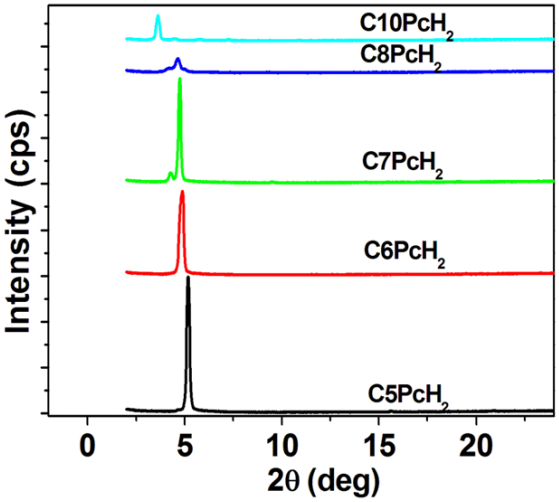

Fig. 4.6. XRD patterns of $CnPcH_2$ thin films spin-cast on glass substrates.

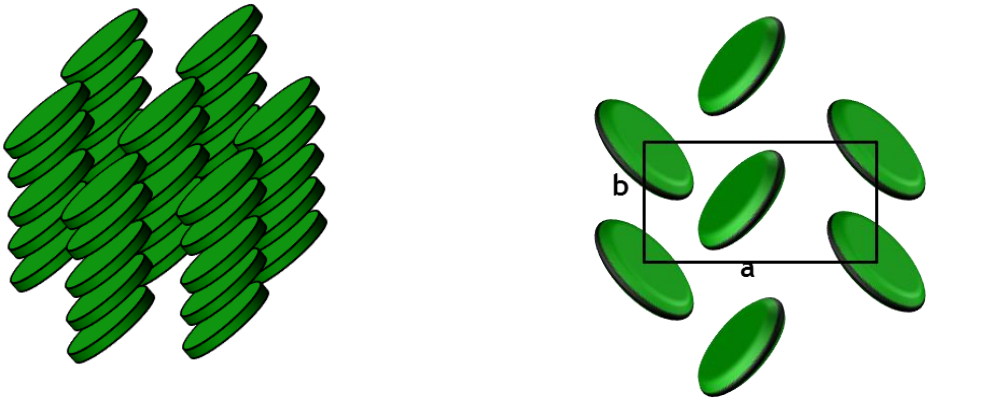

Fig. 4.7. $CnPcH_2$ structures in this study.

From a geometrical point of view, besides stacking period of molecules along columnar axis, columnar structures are also characterized by intercolumnar stacking, which was experimentally determined by small angle X-ray diffraction. In 1991, Cherodian et al. reported the structures of $CnPcH_2$ at the mesophases by using X-ray diffractometer [83]. One found that absence of a peak corresponding to the (210) plane suggests the lattice is "*c*" centered. Coincidence of (200) and (110) peaks, and absence of (210) peak further implies that the lattice constant $a = 3^{1/2} \times b$, and that the

mesogenic phthlocyanine comprises columnar stacks of co-facial molecules arranged within a classical two dimensional hexagonal lattice symmetry, which is denoted as pseudo-hexagonal structures [83]. On the other hand, symmetry of columns is likely to be 2-D rectangular lattice if diffraction arising from (210) plane and splitting of (200)/(110) or (310/020) (because $a \neq 3^{1/2} \times b$) are apparent, as shown in Fig. 4.7 [83].

As shown in Fig. 4.6, the peaks, corresponding to (200)/(110) planes, were coincident in the case of $C5PcH_2$ and $C6PcH_2$, and split when alkyl substituent was lengthened to 7, 8, or 10. Although other peaks in the small region of all $CnPcH_2$ XRD patterns in this study were absent possibly because of the finite resolution of the diffractometer and/or slenderness of spin-cast films, it was suggested that symmetry of $C5PcH_2$ and $C6PcH_2$ columns was probably pseudohexagonal structures, and that the symmetry of the long-alkyl-substituent $CnPcH_2$ (with n is 7, 8 and 10) columns was likely to be 2-D rectangular lattices.

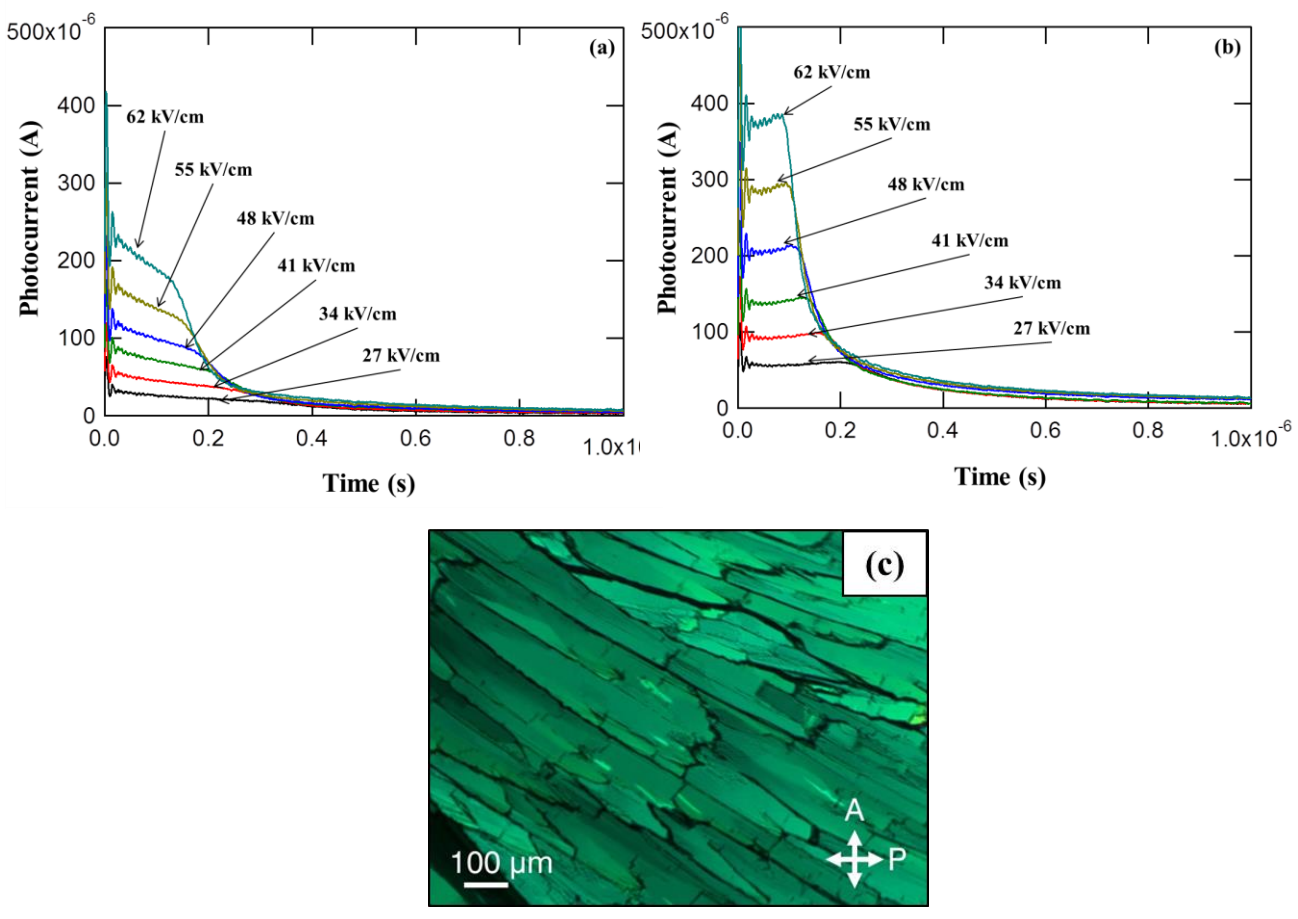

Fig. 4.8. Transient photocurrent decay curves for (a) hole and (b) electron, and (c) polarizing photomicrograph of $C5PcH_2$, in the crystal phase at 25 ºC.

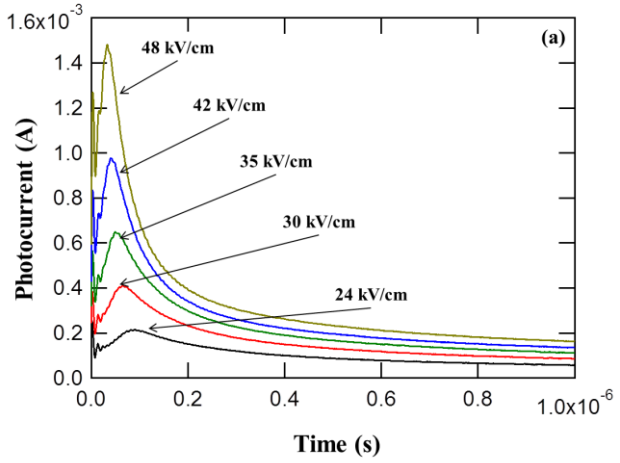

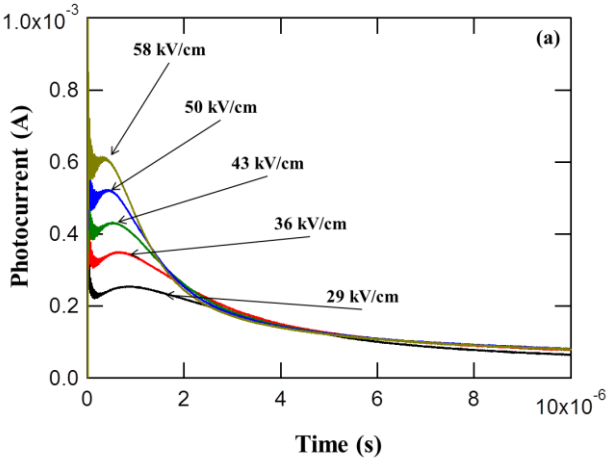

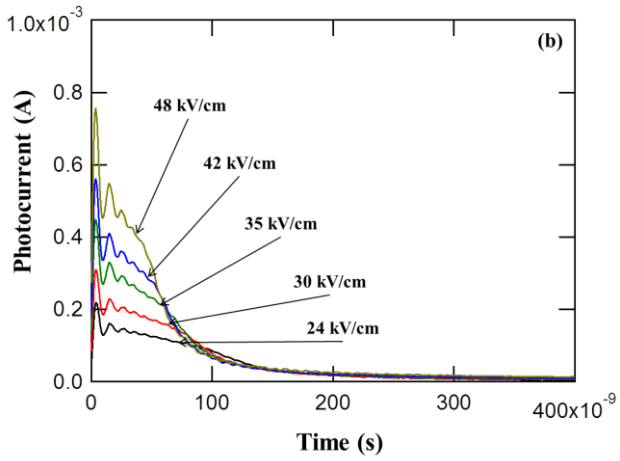

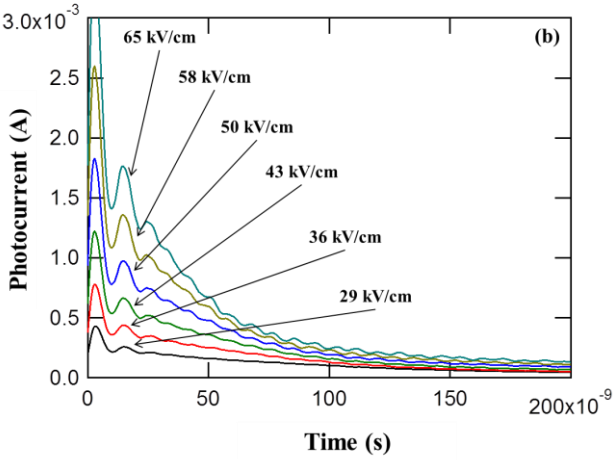

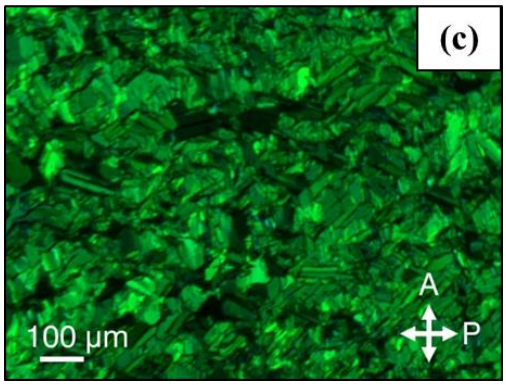

Fig. 4.9. Transient photocurrent decay curves for (a) hole and (b) electron, and (c) polarizing photomicrograph of $C6PcH_2$, in the crystal phase at 25 ºC.

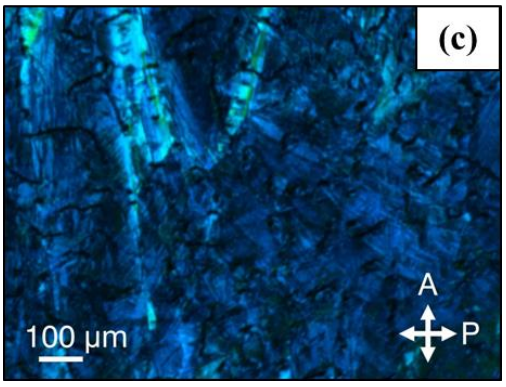

Fig. 4.10. Transient photocurrent decay curves for (a) hole and (b) electron, and (c) polarizing photomicrograph of $C8PcH_2$, in the crystal phase at 25 ºC.

When the structures of $CnPcH_2$ are modified by lengthening the alkyl substituents, the strong dependence of the charge carrier mobilities of $CnPcH_2$ on the alkyl substituents length should be expected. Figure 4.8, 4.9, and 4.10 shows the transient photocurrent decay curves for hole and

electron and the polarizing photomicrograph of $C5PcH_2$, $C6PcH_2$, and $C8PcH_2$, respectively, in the crystal phase at 25 ºC. The hole and electron mobilities of all $CnPcH_2$ were estimated and summarized in Table 4.4.

Table 4.4. Hole and electron mobilities in the crystal phase at 25 ºC of $C5PcH_2$, $C6PcH_2$, and $C8PcH_2$, measured by using TOF.

	Hole mobility (cm^2/Vs)	Electron mobility (cm^2/Vs)
$C5PcH_2$ in solid phase	0.15	0.23
$C6PcH_2$ in solid phase	0.81	0.70
$C8PcH_2$ in solid phase	0.03	0.51
$C10PcH_2$ in solid phase	0.02	---

One found that the hole mobilities of $CnPcH_2$ was strongly dependent on the length of alkyl substituents, which contributed to the crystallinity and the molecular packing. While $C5PcH_2$ and $C6PcH_2$ in the pseudohexagonal structure exhibited the high hole mobilities of 0.15 and 0.81 cm^2/Vs, the hole mobilities of $C8PcH_2$ and $C10PcH_2$ in the 2-D rectangular lattice were reduced to 0.03 and 0.02 cm^2/Vs, respectively. In contrast, the dependence of the electron mobility on the alkyl substituent length was minimal. Particularly, $C5PcH_2$, $C6PcH_2$, and $C8PcH_2$ showed the electron mobilities of 0.23, 0.70, and 0.51 cm^2/Vs, respectively. This surprisingly resulted in the balance of the electron and hole mobilities in the short-alkyl-substituent $CnPcH_2$ ($C5PcH_2$ and $C6PcH_2$), and the imbalance of the electron and hole mobilities in the long-alkyl-substituent $CnPcH_2$ ($C8PcH_2$) [84].

4.4 Dependence of photovoltaic performance on alkyl substituent length

Figure 4.11 shows the EQE and *J-V* characteristics of $CnPcH_2$:[70]PCBM devices in an ITO/MoO_x/BHJ/LiF/Al structure under AM 1.5G illumination at an intensity of 100 mW/cm^2. The cell characteristics for all devices are summarized in Table 4.5. All the EQE spectra showed the strong Q-band and B-band of $CnPcH_2$, and a shoulder around 500 nm of [70]PCBM. It is noted that the peak at around 500 nm corresponding to the absorption of [70]PCBM did not clearly appeared, which were different from the EQE of $C6PcH_2$:[70]PCBM devices in the chapter 3. This result was probably due to the absorption of glass substrates used in this experiment. Moreover, the EQE was strongly dependent on the length of alkyl substituents. Particularly, by shortening the alkyl substituents, the EQE at Q-band was improved from 22 to 49%.

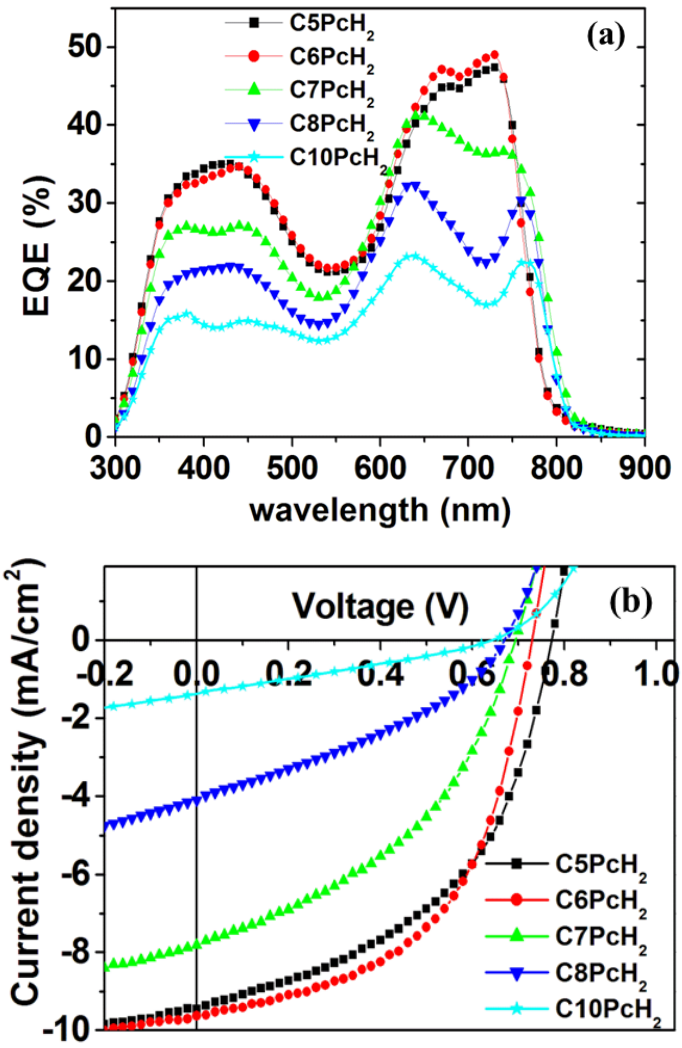

Fig. 4.11. (a) EQE spectra and (b) *J-V* characteristics of the $CnPcH_2$:[70]PCBM BHJ OSCs.

Table 4.5. Characteristics of $CnPcH_2$-based BHJ OSCs, measured under 100 mW/cm^2 light illumination.

BHJ OSCs	V_{oc} (V)	J_{sc} (mA/cm^2)	*FF*	Efficiency (%)
$C5PcH_2$	0.77	9.5	0.48	3.5
$C6PcH_2$	0.73	9.6	0.53	3.7
$C7PcH_2$	0.69	7.8	0.42	2.6
$C8PcH_2$	0.67	4.1	0.35	1.0
$C10PcH_2$	0.65	1.4	0.28	0.3

One found that J_{sc} is directly corresponding to the value of EQE, as shown in equation (1.4) and the improved EQE often causes the high J_{sc} and PCEs. As a result of the EQE, the J_{sc} of

$CnPcH_2$:[70]PCBM devices was strongly dependent on the length of alkyl substituents, as shown in Table 4.5. In particular, the J_{sc} of the BHJ OSCs utilizing $C8PcH_2$ and $C10PcH_2$ were 1.4 and 4.1 mA/cm^2, respectively. By shortening the alkyl substituent length, the J_{sc} increased to 9.5 and 9.6 mA/cm^2 for the BHJ OSCs utilizing $C5PcH_2$ and $C6PcH_2$, respectively. Furthermore, the BHJ OSCs utilizing $C5PcH_2$ and $C6PcH_2$ exhibited the higher *FF* of 0.48 and 0.53, respectively, compared with those of the devices fabricated from the long-alkyl-substituent $CnPcH_2$ ($C7PcH_2$, $C8PcH_2$, or $C10PcH_2$). It was suggested that the aforementioned balance of the hole and electron mobility of probably induced the high FF of the devices utilizing $C5PcH_2$ and $C6PcH_2$ [85].

One found that the maximum V_{oc} otherwise is considered to be limited by the work function of the metal electrodes and the energy gap between the HOMO of the donor materials and the LUMO of the acceptor fullerenes, ΔE_{DA} [70-73]. Although the difference between V_{oc} and ΔE_{DA} is still subject to debate, a linear relationship between V_{oc} and ΔE_{DA} has been experimentally confirmed [73]. Hence, with the aforementioned increases in HOMO levels, the V_{oc} of $CnPcH_2$-based BHJ OSCs exhibited the strong dependence on the length of alkyl substituents. Particularly, by shortening the alkyl substituents, the V_{oc} was improved from 0.65 to 0.77 V and the PCE of devices increased to 3.7% [84].

4.6 Conclusions

In summary, the strong dependences of optical and electronic properties, structures, and photovoltaic performance of BHJ OSCs utilizing $CnPcH_2$ mixed [70]PCBM on the length of alkyl substituents were studied. By decreasing the length of alkyl substituents, stacking of the discotic $CnPcH_2$ columns was probably changed from 2-D rectangular lattices to pseudohexagonal structures, and Davydov splitting at the Q-band of $CnPcH_2$ absorbance spectra decreased. As a result, the short-akyl-substituent $CnPcH_2$ ($C5PcH_2$ and $C6PcH_2$) exhibited the deeper HOMO energy levels and the balance of hole and electron mobility. Furthermore, the EQE at Q-band of $CnPcH_2$-based BHJ OSCs was improved from 22 to 49%, the PCE increased to 3.7% by altering the length of alky substituents.

Chapter 5

Mechanism of degradation and improvement of stability on mesogenic-phthalocyanine-based solar cells

5.1 Introduction

Research in the field of OSCs is still in an exciting phase with a rapid progression of improvements in the technique as detailed in a series of reviews [86-92]. Although, the researches were carried out with the many research areas from field of polymer to low band-gap materials, and small-molecule OSCs, from planar-heterojunction OSCs to BHJ OSCs, and from single layer OSCs to tandem OSCs, the main direction has been only towards the achievements of as the high PCEs as possible under simulated sunlight.

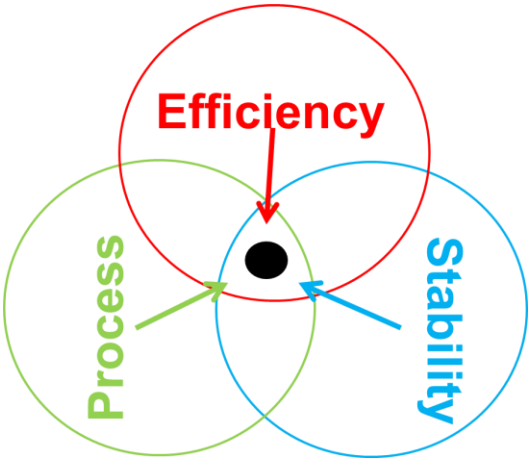

Fig. 5.1. Challenges of unifying efficiency, stability and process for BHJ OSCs.

The important aspects other than the PCEs that have been identified are the stability and the processing, as shown in Fig. 5.1 [93, 94]. However, these individual areas, especially the poor stability of OSCs, have been given relatively little consideration. Moreover, when inorganic silicon-based solar cells may last on the order of 25 years, organic devices must be improved tremendously to become technologically interesting. A number of studies have been carried out and they exhibited that the stability/degradation issue is rather complicated and certainly not yet fully understood, though progress has been made.

OSC degradation generally could be clarified from the chemical, structural, and electrical viewpoints, as illustrated in Fig. 5.2. It has been reported that environmental conditions, such as oxygen and moisture dramatically degrade the lifetime of OSCs, whereas buffer layers on the active layer play an important role in improving the stability [95, 96]. However, further detailed studies are required to allow comprehensive understanding of the degradation mechanism and hence to extend the device lifetime.

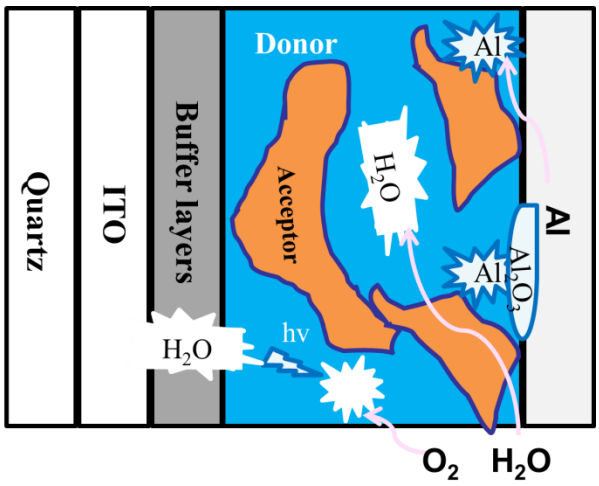

Fig. 5.2. Cross section view of OSCs with the many processes that conspire to degrade BHJ OSCs.

As described in Chapter 2, by utilizing processing additives, the C6PcH_2:[60]PCBM based BHJ OSCs showed the relatively high PCE of 4.2% and EQE at Q band of phthalocyanine close to 60% with the optimum donor-acceptor phase separation and crystallization of the BHJ materials. Furthermore, the structures, optical and electronic properties of CnPcH_2 were studied in Chapter 4. However, the stability and the mechanism of degradation of the OSCs utilizing C6PcH_2 were not yet concerned. In this chapter, the high stability as well as the mechanism of degradation of C6PcH_2-based BHJ OSCs was reported. The operation time dependence of the cell characteristics of C6PcH_2-based cells have been compared with those of the cells with a conventional donor material, P3HT, in the different ambient. Furthermore, the degradation mechanisms of the OSCs have been investigated. To improve the stability, various buffer layers have been introduced between the counter electrode and the active layer.

5.2 Experimental Procedure

$C6PcH_2$ was synthesized as described in the literature [55], with slight modifications, and fully purified by column chromatography (silica-gel with toluene as eluent) followed by repeated recrystallization from toluene–methanol (1:2) solution [9]. Regioregular P3HT and [60]PCBM were purchased from Merck and Frontier Carbon, respectively.

BHJ films were prepared under optimized conditions in accordance with the following procedures. The ITO-coated quartz substrate was cleaned with detergent, ultrasonicated in water, chloroform, acetone, and isopropyl alcohol, and subsequently dried with UV-induced ozone. 6-nm-thick MoO_x films were thermally evaporated onto ITO substrates at a rate of 0.1 Å/s under a vacuum of about 2×10^{-5} Pa. After transferring the films to a N_2-filled glove box, a solution containing a mixture of $C6PcH_2$:[60]PCBM (2:1) in toluene or chloroform was spin-cast at 500 rpm onto a MoO_x layer. The concentration of the solution with the various solvents for $C6PcH_2$:[60]PCBM BHJ OSCs was summarized in Table 5.1 and the thickness of the active layers was approximately 180 nm. Herein, the thickness of the active layers was measured using AFM. On the other hand, a similar process with the blend solution, as summarized in Table 5.2, was performed to fabricate the P3HT-based devices. Herein, the PCE of each device were optimized by adjusting the ratios of donor and acceptor. Finally, a 0.3-nm-thick LiF buffer layer and a 80-nm-thick aluminum or silver cathode were deposited through a shadow mask by thermal evaporation under a vacuum of about 2×10^{-5} Pa. In the case of the cells with a low-work-function cathode, a 25-nm-thick Ca layer was fabricated and then covered with an Al layer to protect it from oxidization. The active area of the device was 4 mm^2.

Table 5.1. Solution concentrations for $C6PcH_2$:[60]PCBM BHJ OSCs in this study

	$C6PcH_2$ (mg/ml)	[60]PCBM (mg/ml)
Chloroform	8	4
Toluene	14.2	7.1

Table 5.2. Solution concentrations for P3HT:[60]PCBM BHJ OSCs in this study

	P3HT (mg/ml)	[60]PCBM (mg/ml)
Chloroform	5	5

The devices characteristics were measured using a XES 301 (AM 1.5 G) full spectrum solar simulator at an irradiation intensity of 100 mW/cm^2, which increased the temperature of the environment of the device up to 45 ºC. The J-V characteristics were measured using a source measure unit (Keithley, 236). Otherwise, EQE spectra were measured with a programmable electrometer using xenon lamp light passing through a monochromator as a light source. The integrated EQE values always show good agreement with the measured J_{sc}. The absorbance spectra were measured by spectrophotometry (Shimadzu UV-3150). Furthermore, the chemical characteristics and crystallinity of the $C6PcH_2$ molecule in thin films were also evaluated by X-ray diffraction (Rigaku RINT 2000) and X-ray photoelectron spectroscopy (XPS; Shimadzu ESCA 850).

5.3 High stability of BHJ OSCs utilizing $C6PcH_2$

Figure 5.3 shows the cell characteristics of the P3HT:[60]PCBM BHJ OSCs and $C6PcH_2$:[60]PCBM BHJ OSCs without packaging or encapsulation as a function of time under light illumination at 100 mW/cm^2. Herein, the P3HT-based solar cells in the simple structure of ITO/MoO_x/BHJ/Al showed an initial PCE of 1.8%, with a J_{sc} of 7.2 mA/cm^2, an V_{oc} of 0.55 V, and a *FF* of 0.46, each of which was normalized by its initial value. The results indicated that the PCE of the devices fabricated using P3HT decreased by approximately 38% after 9 h of continuous illumination in air ambient owing to the rapid degradation of J_{sc}. Otherwise, V_{oc} and FF seem to be slightly degraded. This result was comparable to those in a previous report by Kawano and Adachi [96].

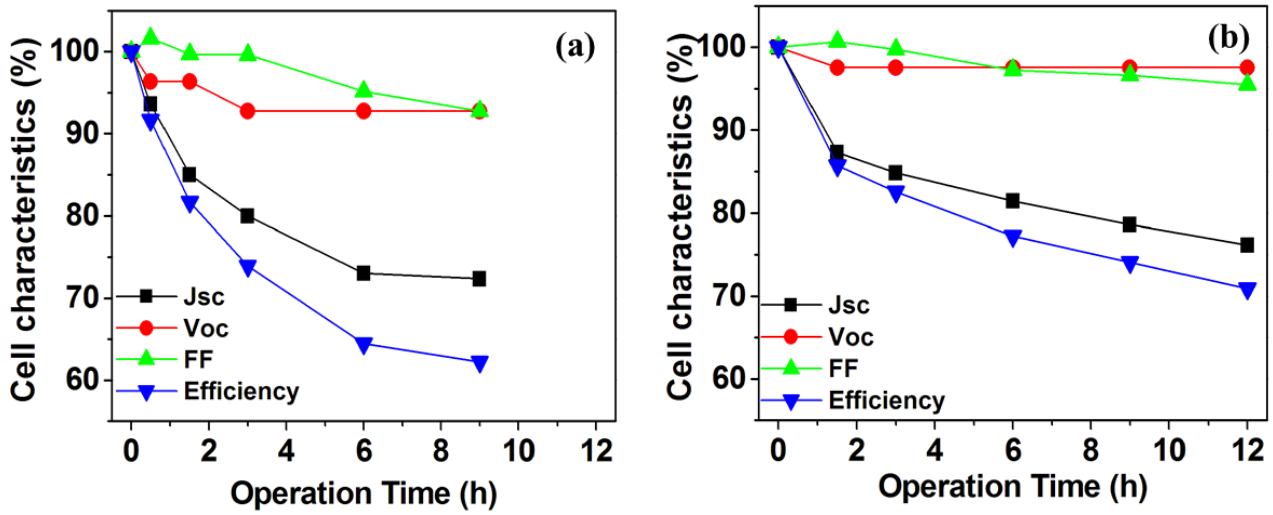

Fig. 5.3. Cell characteristics, normalized by their initial values, as a function of illumination time under 100 mW/cm^2 light illumination, of the OSCs fabricated utilizing (a) P3HT and (b) $C6PcH_2$.

On the other hand, the $C6PcH_2$:[60]PCBM BHJ OSCs in the structure of ITO/MoO_x/BHJ/Al were fabricated and the photovoltaic performances and stability of devices were measured under the similar ambient conditions. It exhibited that the stability of the devices fabricated using $C6PcH_2$ was higher than that of the devices fabricated using P3HT. In particular, the PCEs of the devices fabricated using $C6PcH_2$ remained at about 71% after 12 h illumination, as shown in Fig. 5.3(b). Herein, the initial PCEs of the BHJ OSCs utilizing $C6PcH_2$ were estimated to be 1.89% with a J_{sc} of 5.28 mA/cm^2, a V_{oc} of 0.81 V, and a *FF* of 0.44.

Furthermore, the device lifetime was evaluated under various conditions, such as air or nitrogen atmosphere, without illumination by a solar simulator, as shown in Fig. 5.4. The device lifetime was totally improved by utilizing $C6PcH_2$ in the simple structure of ITO/MoO_x/BHJ/Al without the any ambient-condition dependence.

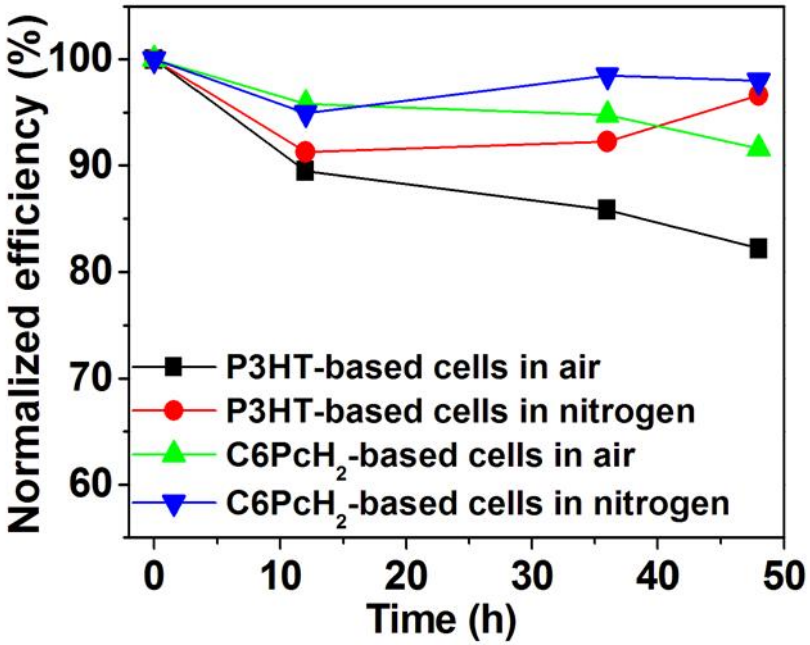

Fig. 5.4. Normalized efficiency as a function of time of the $C6PcH_2$:[60]PCBM BHJ OSCs and P3HT:[60]PCBM BHJ OSCs, stored in a dark environment.

5.4 Mechanism of degradation of BHJ OSCs utilizing $C6PcH_2$

To investigate the degradation mechanism of BHJ OSCs fabricated utilizing $C6PcH_2$, the active layers were spin-cast from the $C6PcH_2$:[60]PCBM blend solutions onto glass substrates and then illuminated by the solar simulator. The properties of the solar-simulator illuminated thin films were characterized from the viewpoints of the XRD patterns, XPS spectra, and absorption spectra.

Figure 5.5 shows the absorption spectra of the $C6PcH_2$:[60]PCBM composite thin films with

and without illumination. It is seen that the absorption spectra of $C6PcH_2$:[60]PCBM composite thin films without illumination exhibited the strong Q-band and B-band at around 700 and 350 nm, respectively. However, after 100 h of illumination in air environment, the absorption peak that originated from the Q band at approximately 700 nm in wavelength disappeared, and the pristine green color of $C6PcH_2$ also disappeared, as shown in Fig. 5.6. On the other hand, the absorption spectra of the $C6PcH_2$:[60]PCBM composited thin films and the pristine green color of $C6PcH_2$ seemed to be unchanged while the thin film was illuminated in vacuum by the solar simulator. It is hypothesized that photooxidation is one of the main mechanisms of the degradation of the devices utilizing $C6PcH_2$.

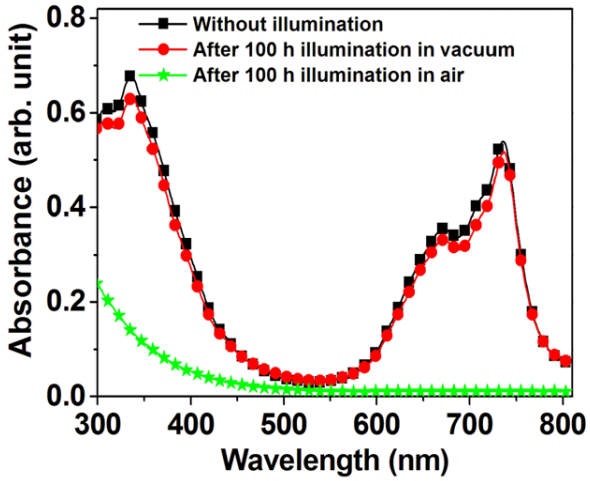

Fig. 5.5. Absorption spectra of the $C6PcH_2$:[60]PCBM composite thin films with and without illumination.

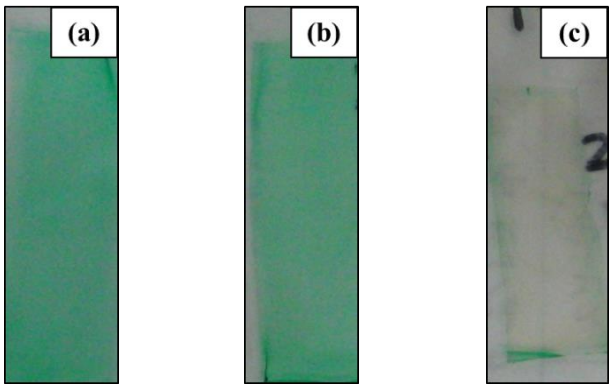

Fig. 5.6. Images of the $C6PcH_2$:[60]PCBM composite thin films (a) before illumination, and after 100 hour illumination in (b) vacuum and (c) air.

Figure 5.7 shows the XRD patterns of the $C6PcH_2$:[60]PCBM composite thin films with and without illumination in air environment. The XRD patterns of all composite thin films exhibited only

the reflections in the small angle regions at approximately 5º, corresponding to the intercolumnar distance between the axes of neighboring C6PcH$_2$-discotic columns, D. Moreover, the D was estimated and summarized in Table 5.3. The intercolumnar distance D of hexagonal columns in the C6PcH$_2$:[60]PCBM composite thin film, measured immediately after spin-casting, was estimated to be 17.66 Å. However, after illuminating under solar simulator in air, the distance D was enlarged. In particular, the distances between two columns in the hexagonal structure of the C6PcH$_2$ molecule became 17.95 and 18.03 Å after 50 and 100 h of illumination in air, respectively.

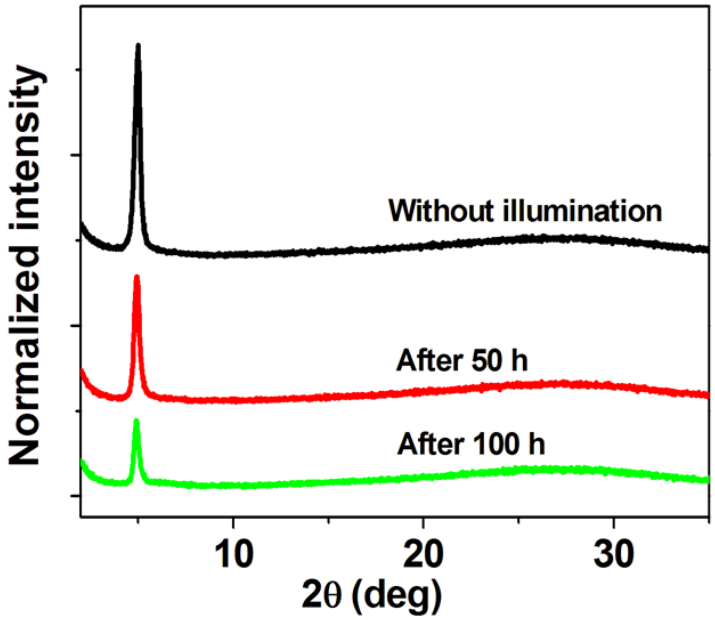

Fig. 5.7. XRD patterns of C6PcH$_2$:[60]PCBM composite thin films with and without illumination in air. All XRD patterns were normalized at 4.88º.

Table 5.3. Intercolumnar distance of the hexagonal columns in the C6PcH$_2$:[60]PCBM composite thin films with and without illumination.

	D (Å)
Origin	17.66
After 50 h	17.95
After 100 h	18.03

The C6PcH$_2$:[60]PCBM composite thin films with and without illumination were characterized by XPS, as shown in Fig. 5.8(a). It exhibited that the N1s core-level spectra consisted of three components of binding energies: 398.9, 400.4, and 402.7 eV. It was reported that the peak at 398.9 eV is associated with twofold-coordinated nitrogens: the two pyrrole aza nitrogens and the four

meso-bridging aza nitrogens, denoted as N2 and N3 in Fig. 5.8(b), respectively [97]. Otherwise, the peak at 400.4 eV is associated with the two threefold-coordinated pyrrole nitrogens bonded to hydrogen atoms in the central ring of the molecule, denoted as N1 in Fig. 5.8(b) [97]. The weak peak at 402.7 eV is due to shake-up transitions [98]. Obviously, after the illumination period, the ratio of the intensity at 398.9 eV to that at 400.4 eV rapidly decreased. This meant that the bonds of nitrogen atoms at N3 and N2 with neighboring carbons were broken, or the $C6PcH_2$ rings were opened. Furthermore, the increase in the concentrations of oxygen atoms in the $C6PcH_2$ and [60]PCBM composite thin films with illumination in air (Table 5.4) also must be the evidence of the photochemical reaction between oxygen atoms and organic active layer materials.

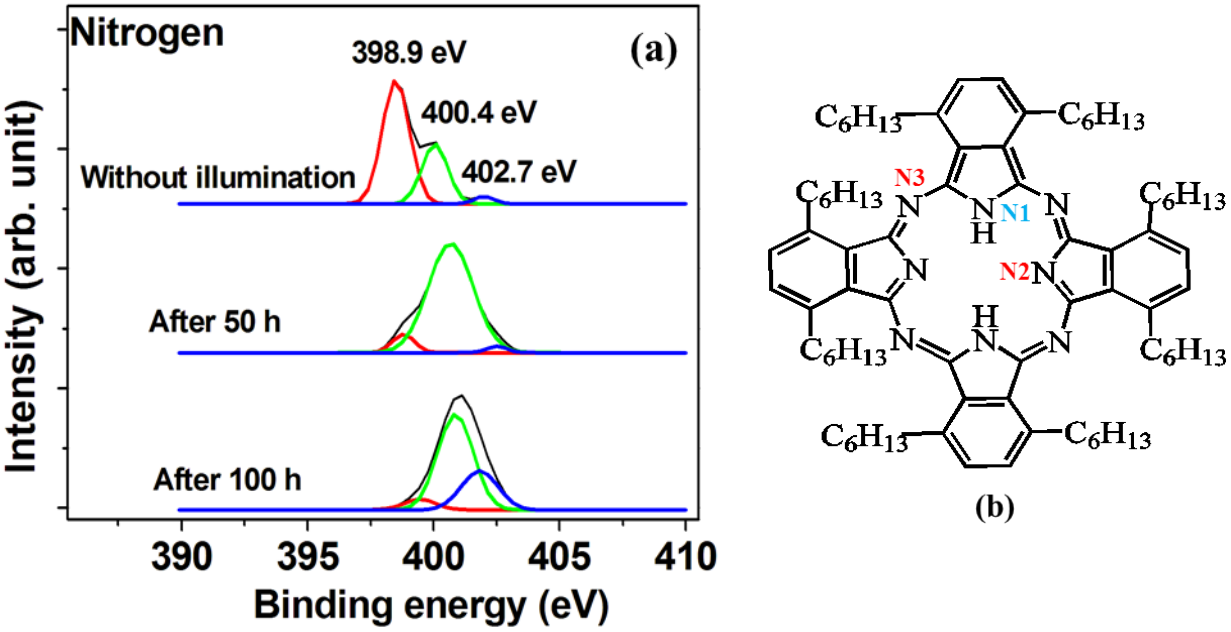

Fig. 5.8. (a) XPS spectra of $C6PcH_2$:[60]PCBM composite thin films with and without illumination in air and (b) Molecular structure of $C6PcH_2$.

Table 5.4. Concentration of oxygen atoms (%) in the $C6PcH_2$:[60]PCBM composite thin films with and without illumination.

	No etching	3s etching	6s etching
Origin	0.59	0	0
After 50 h	18.49	3.26	2.40
After 100 h	27.21	14.08	9.58

5.5 Effects of counter electrodes and buffer layers at top of cell on stability

The stability of OSCs, however, depends not only on the photooxidation of the organic BHJ materials, but also on the oxidation of metal at counterelectrodes and the reaction between the metal and the organic material. In the terms of OSCs, Al with a low work function is commonly deposited as a top electrode by thermal evaporation and plays an important role in efficient electron extraction. However, during thermal evaporation processes, the hot metal atoms might react with oxygen species remaining in the vacuum chamber and diffuse into the organic layers, which would affect the OSC lifetime [99, 100]. Herein, the effects of the counter electrodes and buffer layers at the top of cells on the stability of C6PcH$_2$:[60]PCBM BHJ OSCs were studied.

Figure 5.9 shows the EQE spectra and *J-V* characteristics of the C6PcH$_2$:[60]PCBM BHJ OSCs with the various counter electrodes under AM 1.5G illumination at an intensity of 100 mW/cm^2. The cell characteristics for all devices are summarized in Table 5.5. The EQE of all C6PcH$_2$:[60]PCBM BHJ OSCs exhibited the strong peaks at the Q-band and B-band of the C6PcH$_2$. However, the EQE of the devices utilizing the Ca/Al counter electrodes was lower than that of the devices utilizing Ag or Al counter electrodes. As a result of EQE, the J_{sc} decreased to be 6.5 mA/cm^2 after adding Ca between the active layers and Al counter electrodes. On the other hand, a slight variation of the V_{oc} being only 40 mV was observed when changing the work function of the negative electrode from 4.8 (Ag) to 2.9 eV (Ca).

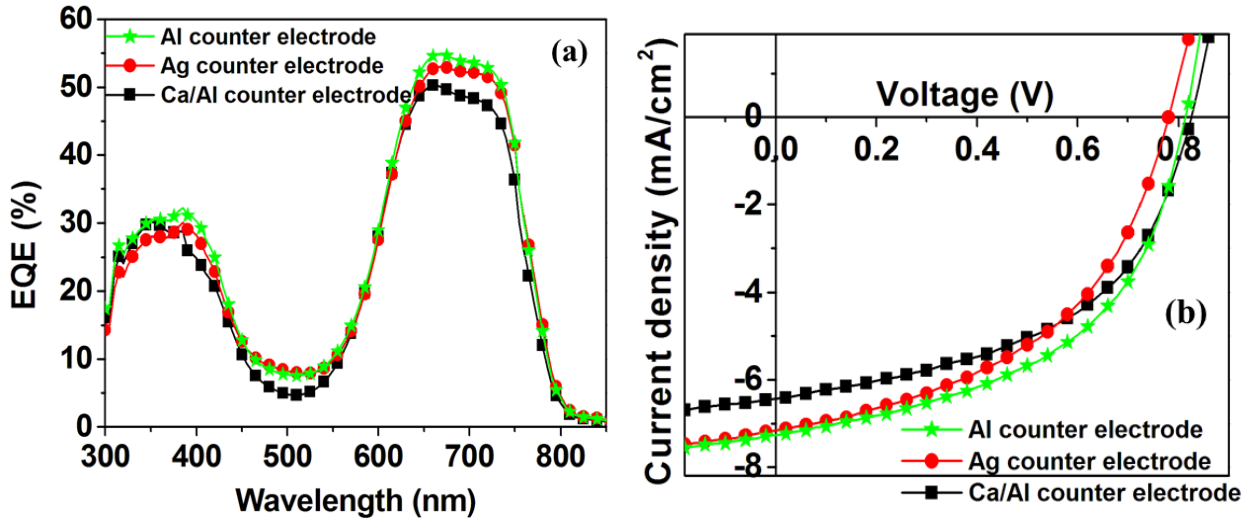

Fig. 5.9. (a) EQE spectra and (b) J-V characteristics of the C6PcH$_2$:[60]PCBM BHJ OSCs with various counter electrodes.

Table 5.5. Cell characteristics of C6PcH$_2$:[60]PCBM BHJ OSCs with various counter electrodes, measured under 100 mW/cm^2 light illumination.

Counter electrode	V_{oc} (V)	J_{sc} (mA/cm^2)	*FF*	Efficiency (%)
Al	0.81	7.3	0.51	2.7
Ag	0.79	7.2	0.47	2.7
Ca/Al	0.83	6.5	0.51	3.0

Figure 5.10 shows the efficiency of the C6PcH$_2$:[60]PCBM BHJ OSCs with various counterelectrodes as a function of the duration of continuous illumination by the solar simulator. Note that each value is normalized by their initial values.

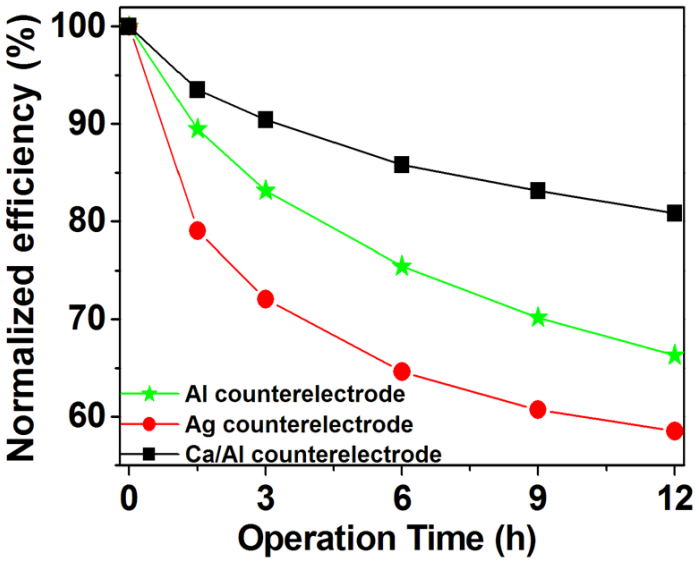

Fig. 5.10. Normalized efficiency as a function of illumination time under 100 mW/cm^2 light illumination in air, of the C6PcH$_2$:[60]PCBM BHJ OSCs with the various counter electrodes.

One found that a decrease of approximately 34% in the PCEs of the Al-based device was improved to a 19% loss in PCE upon the insertion of Ca. Utilizing Ag electrodes instead of Al electrodes, otherwise, resulted in the degradation of approximately 42% in the PCE after 12 h of illumination in air. It was assumed that the oxidized layers, which were unexpectedly created during thermal evaporation, prevent the diffusion of metal electrodes into the organic active layers and hence affect the OSC lifetime. During thermal evaporation processes, the hot metal atoms might react with oxygen species remaining in the vacuum chamber and create the oxidized metal/organic interfacial area. For the Ca electrode, which oxidizes more easily, the oxidized Ca/organic interfacial

layers were probably thicker than the oxidized Al/organic interfacial layers; hence, the cells with Ca counterelectrodes were more stable than those with Al counterelectrodes. In contrast, because of the high resistance of Ag to oxidation, the oxidized Ag/organic interfacial layers were probably thinner than the oxidized Al/organic interfacial layers; hence, the cells with Ag counterelectrodes were markedly degraded. It was considered that these oxidized layers could improve the stability of the devices. On the other hand, the oxidized Ca/organic interfacial layers probably resulted in the relatively low J_{sc} of the C6PcH$_2$:[60]PCBM BHJ OSCs utilizing Ca/Al counter electrodes, as described above.

LiF, reported widely to be an ideal electron injection layer with many advantages, such as ohmic-like behavior at the cathode interface and protection of the organic layer from hot Al atoms, was introduced to improve the device performance [96, 101]. The EQE spectra and J-V characteristics of the C6PcH$_2$:[60]PCBM BHJ OSCs with the LiF and/or C_{60} buffer layers at the top under AM 1.5G illumination at an intensity of 100 mW/cm^2 are shown in Fig. 5.11. The cell characteristics for all devices are summarized in Table 5.6.

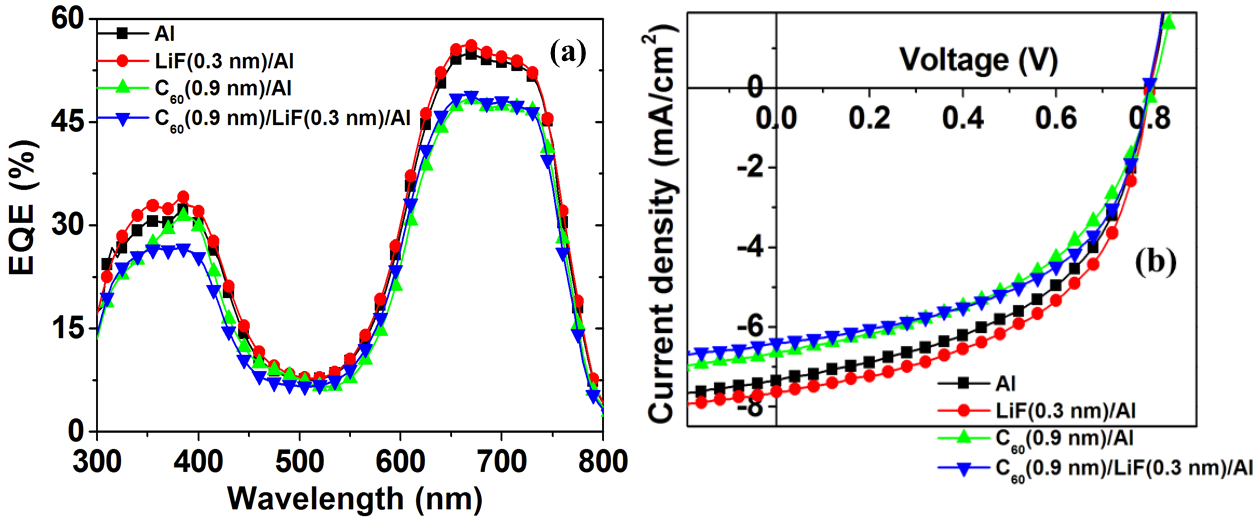

Fig. 5.11. (a) EQE spectra and (b) *J-V* characteristics of the C6PcH$_2$:[60]PCBM BHJ OSCs with various buffer layers at the top of cells.

Table 5.6. Cell characteristics of $C6PcH_2$:[60]PCBM BHJ OSCs with various buffer layers at the top of cells, measured under 100 mW/cm^2 light illumination.

	V_{oc} (V)	J_{sc} (mA/cm^2)	*FF*	Efficiency (%)
Al	0.80	7.4	0.51	3.0
LiF(0.3 nm)/Al	0.80	7.6	0.52	3.2
LiF(0.5 nm)/Al	0.79	7.4	0.53	3.1
LiF(0.7 nm)/Al	0.81	7.4	0.51	3.1
LiF(0.9 nm)/Al	0.80	7.4	0.48	2.8
C_{60}(0.9 nm)/Al	0.81	6.6	0.48	2.6
C_{60}(0.3 nm)/ LiF(0.3 nm)/Al	0.79	7.7	0.50	3.1
C_{60}(0.9 nm)/ LiF(0.3 nm)/Al	0.79	6.4	0.53	2.7

One found that increases in J_{sc} and *FF* were observed for the $C6PcH_2$-based devices upon the insertion of a thin layer of LiF between the organic layer and the Al electrode. In particular, by introducing a 0.3-nm-thick LiF layer, the *FF* increased from 0.51 to 0.53. Together with J_{sc} of 7.63 mA/cm^2, the PCE was calculated to be 3.2%. Even though the variations of the *FF* and PCE of devices with LiF were slight, this finding indicated that LiF lowered the effective work function of Al as well as provides ohmic-like behavior at the cathode interface.

However, after 12 h of illumination in air, the decrease of approximately 34% in the PCE of the devices with a pristine Al electrode was reduced to a 43% loss in the PCE upon the insertion of the LiF layer, as shown in Fig. 5.12. The degradation of the devices utilizing the LiF buffer layers at the top was totally opposite to the stability improvement of the P3HT-based device with inserted LiF [96]. For the clear understanding of the interaction between LiF and active layers, 0.9-nm-thick C_{60} films have been introduced between LiF and the $C6PcH_2$:[60]PCBM active layers. It exhibited that the decrease of approximately 43% in the PCE was improved to a 20% loss in the PCE upon the insertion of the C_{60} layer. On the other hand, the $C6PcH_2$:[60]PCBM BHJ OSCs with the 0.3-nm-thick C_{60} layer showed the relatively low J_{sc} and the PCE of 7.71 mA/cm^2 and 3.09%, respectively, as summarized in Table 5.6. It was suggested that the diffusion of LiF inside the active layer, which causes the degradation of the OSC lifetime, exists; however, the C_{60} layer plays the important role of a blocking layer that prevents the diffusion of metal atoms into the active layer, and therefore, reinforces stability.

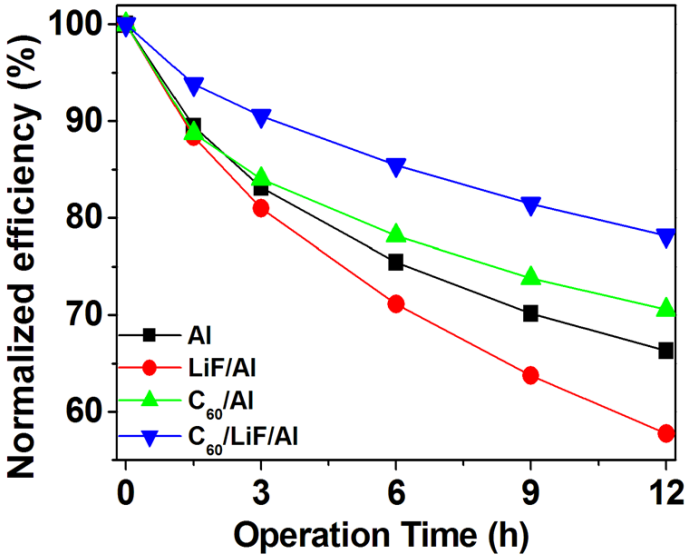

Fig. 5.12. Normalized efficiency as a function of illumination time under 100 mW/cm^2 light illumination in air, of the C6PcH$_2$:[60]PCBM BHJ OSCs with the various buffer layers at the top of cells.

5.6 Conclusions

The high stability as well as the mechanism of degradation of C6PcH$_2$:[60]PCBM BHJ OSCs was reported. The mesogenic phthalocyanine derivative C6PcH$_2$-based BHJ-OSCs showed a higher stability than the cells with the conventional donor material P3HT. By studying the C6PcH$_2$:[60]PCBM composite thin films with and without illumination in various environments, it was clarified that the chemical bonds of two pyrrole aza nitrogens as well as the four mesobridging aza nitrogens with neighboring carbons in the C6PcH$_2$ molecules were broken after illumination by the solar simulator. Photooxidation of active layers could be detected from the increase in oxygen concentration in C6PcH$_2$ and [60]PCBM composite thin films as well as from the disappearance of absorbance at the Q band of C6PcH$_2$. To improve the stability, various buffer layers were introduced between the counter electrode and the active layer. Obviously, the C$_{60}$ thin film and oxidized layer of the counter electrode increased the device lifetime.

Chapter 6

Conclusions

In this dissertation, a series of experiments were conducted in an aim to investigate and improve the photovoltaic performance of the BHJ OSCs utilizing the octaalkylphthalocyanine derivatives with the donor and acceptor phase separation. The PCEs of the BHJ OSCs utilizing $C6PcH_2$ were improved to 4.2% with the optimum separation of donor and acceptor phases, and the optical and electronic properties, structures, and stability of the BHJ materials were also characterized. We summarized the important achievements from each chapter as follows.

In chapter 2, the effects of processing additives on the nanoscale phase separation, crystallization, and photovoltaic performance of the BHJ OSCs utilized discotic $C6PcH_2$ mixed with [60]PCBM were studied. By incorporating processing additives to a volume of a few percent, the separation of donor and acceptor phases in $C6PcH_2$:PCBM thin films, which was discussed by taking the Davydov splitting at the Q-band of the absorbance spectra and the surface nanomorphology into consideration, was improved. It was proposed that the separation of donor and acceptor phases was promoted due to the higher boiling point of the processing additives, compared with that of the primary solvents and the different solubility of [60]PCBM and $C6PcH_2$ in processing additives. Furthermore, the crystallization of discotic $C6PcH_2$ in hexagonal structures has been improved by using processing additives. It was suggested that the improved crystallization was probably due to increases in the solubility of $C6PcH_2$ in processing additives.

Although more efforts should be made to understand the roles of primary solvents as well processing additives on the improvement of the photovoltaic properties of the BHJ OSCs utilized discotic $C6PcH_2$ mixed with [60]PCBM, the nanoscale phase separation and the crystallization of the BHJ materials were clearly optimized and the performance of the BHJ OSCs was markedly improved by utilizing various processing additives mixed with the different primary solvents. In particular, by adding 0.2% v/v of Brom to the solution containing BHJ blends in trichloroethylene, the EQE at the Q-band was improved to 57%, and the PCE increased to 4.2%, with a J_{sc} of 9.7 mA/cm^2, a V_{oc} of 0.76 V, and an *FF* of 0.56.

In chapter 3, the roles of fullerene derivatives in the photovoltaic properties of the BHJ OSCs utilizing $C6PcH_2$ were studied. By replacing the C_{60} moiety of [60]PCBM with the asymmetric C_{70}, the absorption of composite thin films at around 500 nm increased, the EQE of the solar cells at

around 500 nm was improved from 8% to 24%, and J_{sc} increased to 10.2 mA/cm^2. On the other hand, a high V_{oc} of 0.96 V was attained using Bis[60]PCBM with a higher LUMO level. Moreover, the blend ratio dependence of the photovoltaic properties in BHJ OSCs utilizing C6PcH$_2$ mixed with [70]PCBM was reported. With increasing the volume fraction of [70]PCBM, the J_{sc} was improved to 10.6 mA/cm^2 due to enlarging the donor and acceptor interfacial areas. On the other hand, when the [70]PCBM volume fraction was higher than 33%, the *FF* was reduced owning to deteriorating crystallization of discotic C6PcH$_2$ molecules with hexagonal structures.

In chapter 4, the strong dependences of optical and electronic properties, structures, and photovoltaic performance of BHJ OSCs utilizing CnPcH$_2$ mixed [70]PCBM on the length of alkyl substituents were studied. By decreasing the length of alkyl substituents, stacking of the discotic CnPcH$_2$ columns was probably changed from 2-D rectangular lattices to pseudohexagonal structures, and Davydov splitting at the Q-band of CnPcH$_2$ absorbance spectra decreased. As a result, the short-akyl-substituent CnPcH$_2$ (C5PcH$_2$ and C6PcH$_2$) exhibited the deeper HOMO energy levels and the balance of hole and electron mobility.

In chapter 5, the high stability as well as the mechanism of degradation of C6PcH$_2$:[60]PCBM BHJ OSCs was reported. The mesogenic phthalocyanine derivative C6PcH$_2$-based BHJ-OSCs showed a higher stability than the cells with the conventional donor material P3HT. By studying the C6PcH$_2$:[60]PCBM composite thin films with and without illumination in various environments, it was clarified that the chemical bonds of two pyrrole aza nitrogens as well as the four mesobridging aza nitrogens with neighboring carbons in the C6PcH$_2$ molecules were broken after illumination by the solar simulator. Photooxidation of active layers could be detected from the increase in oxygen concentration in C6PcH$_2$ and [60]PCBM composite thin films as well as from the disappearance of absorbance at the Q band of C6PcH$_2$. To improve the stability, various buffer layers were introduced between the counter electrode and the active layer. Obviously, the C_{60} thin film and oxidized layer of the counter electrode increased the device lifetime.

All the described results suggested that the CnPcH$_2$ is one potential donor for BHJ OSCs and the high photovoltaic performances of BHJ OSCs utilizing CnPcH$_2$ are expected. To improve the PCEs of the CnPcH$_2$-based BHJ OSCs, the FFs, which exhibited the low values of 0.58, must be investigated and promoted by adding the various buffer layers at the top of cells. Furthermore, the thermal annealing must be concerned when the alignment of dicostic CnPcH$_2$ molecules in the hexagonal structures were strongly dependent on the temperatures.

Acknowledgement

Although it is only my name that appears on the front cover of this dissertation, this writing would not have been possible without the contribution of many people to whom I owe my sincere gratitude.

First and foremost, I must thank to my supervisor Professor Masanori Ozaki for accepting me in the laboratory and introducing me to organic solar cells. I have truly enjoyed studying this field with the fascinating materials synthesized in his Lab. I also thank Associate Professor Akihiko Fujii for his guidance and helpful advice as I proceeded with my research. This project would have been much harder without his advices. He is true masters of his crafts.

I would like to extend my gratitude to all the Professors at the Division of Electrical, Electronic and Information Engineering at Osaka University. I especially appreciate Professor Yutaka Ohmori and Associate Professor Akihiko Fujii for reviewing this dissertation. I also deeply appreciate Professor Toshimichi Ito, Professor Yusuke Mori, Professor Mitsuhiro Katayama, Professor Toshiaki Suhara, Professor Masahiko Kondow, and Professor Tetsuya Yagi, for serving on my dissertation committee.

I thank to Dr. Toshiya Kamikado and Dr. Yo Shimizu for synthesizing the mesogenic phthalocyanine used to perform the studies discussed in this dissertation. I deeply appreciate Dr. Toshiya Kamikado for taking the time to discuss about the properties of the materials provided. I would not have been able to understand the observed crystallization of mesogenic phthalocyanine if we did not have that time of discussion.

I thank also both present and former personnel of Ozaki laboratory, especially my group members working on solar cells: Mr. Tetsuya Masuda, Mr. Kaoru Fukumura, Mr. Wilzuard Yonan, Mr. Jaeki Kim, Mr. Yasuhiro Ogawa, Mr. Tetsuro Hori, Mr. Takayuki Kumagai, Mr. Hoekyeong Kim, Mr. Takayaki Matsui, Mr. Takuya Higashi, Mr. Junji Kobashi, Mr. Yo Inoue, Mr. Kenji Tagashira, Mr. Takashi Saito, Mr. Hiroki Tone, Mr. Shohei Nakano, Mr. Sun Hwan Lee, Mr. Hitoshi Fukui, Mr. Keita Asakura, Mr. Shigehiro Ikehara, Mr. Masashi Ohmori, Mr. Mitsuyoshi Katayama, Mr. Taishi Kumada, Mr. Yusuke Gotoh, Mr. Uno Takashi, Mr. Yuto kawata, Mr. Koichi Watanabe, Mr. Anucha Knokanok, Mr. Ha Van Truc and Mr. Ramananarivo Mihary Fiderana. It has been a pleasure working with you and I really enjoyed the times we had together. I deeply appreciate Mr. Jaeki Kim and Shuhei Yabu for kindly supports to help me deal with the language-misunderstanding induced troubles during living in Japan.

This work was made possible through the generous support of Grants-in-Aid for Scientific

Research from the Ministry of Education, Culture, Sports, Science and Technology, Japan, and the Advanced Low Carbon Technology Research and Development Program from the Japan Science and Technology Agency (JST-ALCA).

Finally, I am most grateful to my family for all their support and love. I never would have gotten to this point without the love and support of my dad Quang Uy, my mom Khuy, my brother Quang Dong, my wife Mai, and my daughter Binh An. I love you all and will never be able to repay you for all that you have given me.

References

[1] S. Morita, A. A. Zakhidov, and K. Yoshino, "Doping effect of buckminsterfullerene in conducting polymer: change of absorption spectrum and quenching of luminescence", Solid State Commun., **82**, 249-252 (1992).

[2] N. S. Sariciftci, L. Smilowitz, A. J. Heeger, and F. Wudl, "Photoinduced electron transfer from a conducting polymer to buckminsterfullerene", Science, **258**, 1474-1476 (1992).

[3] K. Yoshino, X. H. Yin, S. Morita, T. Kawai, and A. A. Zakhidov, "Enhanced photoconductivity of C_{60} doped poly(2-alkylthiophene)", Solid State Commun., **85**, 85-88 (1993).

[4] G. Yu, J. Gao, J. C. Hummelen, F. Wudl, and A. J. Heeger, "Polymer photovoltaic cells: enhanced efficiencies via a network of internal donor-acceptor heterojunctions", Science, **270**, 1789-1791 (1995).

[5] Y. Sun, G. C.Welch, W. L. Leong, C. J. Takacs, G. C. Bazan, and A. J. Heeger, "Solution-processed small-molecule solar cells with 6.7% efficiency", Nat. Mater., **11,** 44-48 (2012).

[6] R. F. Service, "Outlook brightens for plastic solar cells", Science **332**, 293-293 (2011).

[7] B. C. Thompson and J. M. J. Fréchet, "Polymer-Fullerene Composite Solar Cells", Angew. Chem. Int. Ed., **47**, 58-77 (2008).

[8] M. O' Neill and S. M. Kelly, "Liquid crystals for charge transport, luminescence, and photonics", Adv. Mater., **15**, 1135-1146 (2003).

[9] Y. Miyake, Y. Shiraiwa, K. Okada, H. Monobe, T. Hori, N. Yamasaki, H. Yoshida, M. J. Cook, A. Fujii, M. Ozaki, and Y. Shimizu, "High carrier mobility up to 1.4 $cm^2V^{-1}s^{-1}$ in non-peripheral phthalocyanine", Appl. Phys. Express, **4**, 021604-1-021604-3 (2011).

[10] T. Hori, Y. Miyake, N. Yamasaki, H. Yoshida, A. Fujii, Y. Shimizu, and M. Ozaki, "Solution processable organic solar cell based on bulk heterojunction utilizing phthalocyanine derivative", Appl. Phys. Express, **3**, 101602-1-101602-2 (2010).

[11] M. A. Green, "Solar cells: Operating principles, technology and system applications" Kensington: The University of New South Wales (1998).

[12] S. S. Hegedus and A. Luque, "Status, trends, challenges, and the bright future of solar electricity from photovoltaics", in A. Luque and S. S. Hegedus (Eds.), Handbook of Photovoltaic Science and Engineering (pp. 1-43). Hoboken, NJ: John Wiley & Sons (2003).

[13] M. A. Green, K. Emery, Y. Hishikawa, and W. Warta, "Solar cell efficiency tables (version

42)", Prog. Photovoltaics, **21**, 827-837 (2013).

[14] M. A. Green, "Thin-film solar cells: Review of materials, technologies and commercial status", J. Mater. Sci.: Mater. Electron., **18**, S15-S19 (2007).

[15] C. W. Tang, "Two-layer organic photovoltaic cell", Appl. Phys. Lett., **48** 183-185 (1986).

[16] M. Hiramoto, H. Fujiwara, and M. Yokoyama, "Three-layered organic solar cell with a photoactive interlayer of codeposited pigments", Appl. Phys. Lett., **58**, 1062-1064 (1991).

[17] J. J. M. Halls, C. A. Walsh, N. C. Greenham, E. A. Marseglia, R. H. Friend, S. C. Moratti, and A. B. Holmes,"Efficient photodiodes from interpenetrating polymer networks", Nature, **376**, 498-500 (1995)

[18] G. Yu and A. J. Heeger. "Charge separation and photovoltaic conversion in polymer composites with internal donor/acceptor heterojunctions", J. Appl. Phys., ***78***, 4510-4515 (1995).

[19] W. Ma, C. Yang, X. Gong, K. Lee, and A. J. Heeger, "Thermally stable, efficient polymer solar cells with nanoscale control of the interpenetrating network morphology", Adv. Funct. Mater., **15**, 1617-1622 (2005).

[20] G. Li, V. Shrotriya, J. Huang, Y. Yao, T. Moriarty, K. Emery, and Y. Yang, "High-efficiency solution processable polymer photovoltaic cells by self-organization of polymer blends", Nat. Mater., **4**, 864-868 (2005).

[21] J. Peet, J. Y. Kim, N. E. Coates, W. L. Ma, D. Moses, A. J. Heeger, and G. C. Bazan, "Efficiency enhancement in low-bandgap polymer solar cells by processing with alkane dithiols", Nat. Mater., **6,** 497-500 (2007).

[22] S. E. Shaheen, R. Radspinner, N. Peyghambarian, and G. E. Jabbour, "Fabrication of bulk heterojunction plastic solar cells by screen printing", Appl. Phys. Lett., **79**, 2996-2998 (2001).

[23] [23] C. N. Hoth, S. A. Choulis, P. Schilinsky, and C. J. Brabec, "High photovoltaic performance of inkjet-printed polymer:fullerene blends", Adv. Mater., **19**, 3973-3978 (2007).

[24] P. Kopola, T. Aernouts, S. Guillerez, H. Jin, M. Tuomikoski, A. Maaninen, and J. Hast, "High efficient plastic solar cells fabricated with a high-throughput gravure printing method", Sol. Energy Mater. Sol. Cells, **94**, 1673-1680 (2010).

[25] S.-S. Kim, S.-I. Na, J. Jo, G. Tae, and D.-Y. Kim, "Efficient polymer solar cells fabricated by simple brush painting", Adv. Mater., **19**, 4410-4415 (2007).

[26] F. C. Krebs, T. Tromholt, and M. Jørgensen, "Upscaling of polymer solar cell fabrication using full roll-to-roll processing", Nanoscale, **2**, 873-886 (2010).

[27] R. F. Pierret, "Semiconductor device fundamentals", New York: Addison-Wesley Publishing

Company, Inc (1996).

[28] F. H. Moser and A. L. Thomas, "The Phthalocyanines" (Vol. I and II), CRC: Boca Raton (1983).

[29] P. J. Gregory, "Steamrollers sports cars and security: phthalocyanine progress through the ages", J. Porphyrins Phthalocyanines, **3**, 468-476, (1999).

[30] C. C. Leznoff and A. B. P.Lever, "Phthalocyanines: properties and applications" (Vol. 1-4), VCH: New York.

[31] N. B. McKeown, "Phthalocyanine Materials: Synthesis, Structure and function", Cambridge University Press: Cambridge, (1998).

[32] R. M. Christie, "Colour and constitution relationships in organic pigments. Part 5: The influence of solvents, the central metal atom and substituents on the electronic spectra of phthalocyanines", Dyes and Pigments, **27**, 35-43 (1995).

[33] M. J. Cook, A. N. Dunn, S. D. Howe, A. J. Thomson, and K. J. Harrison, "Octa-alkoxy phthalocyanine and naphthalocyan ine derivatives: dyes with Q-band absorption in the far red or near infrared", Chem. Soc. Perk. T., **1**, 2453-2458 (1988).

[34] N. Kobayashi, S. Nakajima, and T. Osa, "Spectroscopic comparison of tetra-tert-butylated tetraazaporphyrin, phthalocyanine, naphthalocyanine and anthracocyanine cobalt complexes", Inorg. Chim. Acta, **210**, 131-133 (1993).

[35] J. C. Mailocq, C. Giannotti, P. Maillard, and M. Momenteau, " Energy transfer in "covalently linked" and "face-to-face" bisporphyrins", Chem. Phys. Lett., **112**, 87-93 (1984).

[36] G. Cao, D. Qin, J. Cao, M. Guan, Y. Zeng, and J. Li, "Improved performance in organic light emitting diodes with a mixed electron donor-acceptor film involved in hole injection", J. Appl. Phys., **101**, 124507-01-124507-04 (2007).

[37] J. Bartelmess, B. Ballesteros, G. De La Torre, D. Kiessling, S. Campidelli, M. Prato, T. Torres, and D. M. Guldi, "Phthalocyanine-Pyrene Conjugates: A Powerful Approach toward Carbon Nanotube Solar Cells", J. Am. Chem. Soc., **132**, 16202-16211 (2010).

[38] M. J. Cook, "Properties of some alkyl substituted phthalocyanines and related macrocycles", Chem. Rec. **2**, 225-236 (2002).

[39] D. Wohrle and D. Meissner, "Organic solar cell", Adv. Mater., **3**, 129-138 (1991).

[40] J. G. Xue, S. Uchida, B. P. Ran, and S. R. Forrest, "4.2% efficient organic photovoltaic cells with low series resistances", Appl. Phys. Lett., **84**, 3013-3015 (2004).

[41] J. G. Xue, S. Uchida, B. P. Ran, and S. R. Forrest, "Asymmetric tandem organic photovoltaic cells with hybrid planar-mixed molecular heterojunctions", Appl. Phys. Lett., **85**, 5757-5759

(2004).

[42] Y. Kinoshita, T. Hasobe, and H. Murata, “Control of open-circuit voltage in organic photovoltaic cells by inserting an ultra-thin metal-phthalocyanine layer”, Appl. Phys. Lett., **91**, 083518-1-083518-3 (2007).

[43] X. Jiang, J. Dai,; H. Wang, Y. Geng, and D. Yan, “Organic photovoltaic cells using hexadecafluorophthalocyaninatocopper (F16CuPc) as electron acceptor material”, Chem. Phys. Lett., **446**, 329-332 (2007).

[44] M. Y. Chan, S. L. Lai, M. K. Fung, C. S. Lee, and S. T. Lee, “Doping-induced efficiency enhancement in organic photovoltaic devices”, Appl. Phys. Lett., **90**, 023504-1-023504-1 (2007).

[45] P. W. M. Blom, V. D. Mihailetchi, L. J. A. Koster, and D. E. Markov, “Device physics of polymer: fullerene bulk heterojunction solar cell”, Adv. Mater., **19**, 1551-1566 (2007).

[46] H. Hoppe and N. S. Sariciftci, “Morphology of polymer/fullerene bulk heterojunction solar cells”, J. Mater. Chem., **16**, 45-61 (2006).

[47] S. S. V. Bavel, M. Barenklau, G. D. With, H. Hoppe, and J. Loos, “P3HT/PCBM bulk heterojunction solar cells: impact of blend composition and 3D morphology on device performance”, Adv. Funct. Mater., **20** 1458-1463 (2010).

[48] F. Padinger, R. S. Rittberger, and N. S. Sariciftci, “Effects of postproduction treatment on plastic solar cell”, Adv. Funct. Mater., **13**, 85-88 (2003).

[49] J. J. Dittmer, E. A. Marseglia, and R. H. Friend, “Electron trapping in Dye/polymer blend photovoltaic cells”, Adv. Mater., **12**, 1270-1274 (2000).

[50] N. Camaioni, G. Ridolfi, G. C. Miceli, G. Possamai, and M. Maggini, “The effects of a mild thermal treatment on the performance of poly(3-alkylthiophene)/fullerene solar cells”, Adv. Mater., **14**, 1735-1738 (2002).

[51] M. Ohmori, H. Fukui, Q.-D. Dao, T. Kumada, A. Fujii, Y. Shimizu, and M. Ozaki, “Annealing Effect in Bulk Heterojunction Organic Solar Cells Utilizing Liquid Crystalline Phthalocyanine”, to be published to Jpn. J. Appl. Phys.

[52] J. K. Lee, W. L. Ma, C. J. Brabec, J. Yuen, J. S. Moon, J. Y. Kim, K. Lee, G. C. Bazan, and A. J. Heeger, “Processing additives for improved efficiency from bulk heterojunction solar cells”, J. Am. Chem. Soc., **130**, 3619-3623 (2008).

[53] J. Peet, C. Soci, R. C. Coffin, T. Q. Nguyen, A. Mikhailovsky, D. Moses, and G. C. Bazan, “Method for increasing the photoconductive response in conjugated polymer/fullerene composites”, Appl. Phys. Lett., **89**, 252105-1-252105-3 (2006).

[54] Y. Yao, J. Hou, Z. Xu, G. Li, and Y. Yang, “Effects of solvent mixtures on the nanoscale phase separation in polymer solar cells”, Adv. Funct. Mater., **18**, 1783–1789 (2008).

[55] J. C. Swarts, E. H. G. Langner, N. Krokeide-Hove, and M. J. Cook, “Synthesis and electrochemical characterisation of some long chain 1,4,8,11,15,18,22,25-octa-alkylated metal-free and zinc phthalocyanines possessing discotic liquid crystalline properties”, J. Mater. Chem., **11**, 434-443 (2001).

[56] S. Tai and N. Hayashi, “Strong aggregation properties of novel naphthalocyanines”, J. CHEM. SOC. PERKIN TRANS., **2** 1275-1279 (1991).

[57] M. Katayose, S. Tai, K. Kamijima, H. Hagiwara, and N. Hayashi, “Novel silicon naphthalocyanines: synthesis and molecular arrangement in thin films”, J. CHEM. SOC. PERKIN TRANS., **2**, 403-409 (1992).

[58] S. M. Critchley, M. R. Willis, M. J. Cook, J. McMurdo, Y. Maruyama, “Deposition of ordered phthalocyanine films by spin coating”, J. MATER. CHEM., **2**, 157-159 (1992).

[59] P. Day and R. J. P. Williams, “Spectra and photoconduction of phthalocyanine complexes (I)”, J. Chem. Phys., **37**, 567-570 (1962).

[60] D. P. Craig and P. C. Hobbins, “The polarized spectrum of anthracene. part I. the assignment of the intense short wave-length system”, J. Chem. Soc., 539-548 (1955).

[61] Y. K. Kim, S. Cook, S. M. Tuladhar, S. A. Choulis, J. Nelson, J. R. Durrant, D. D. C. Bradley, M. Giles, I. Mcculloch, C.-S. HA, and M. Ree, “A strong regioregularity effect in self-organizing conjugated polymer films and high-efficiency polythiophene:fullerene solar cells”, Nat. Mater., **5**, (197-2003) 2006.

[62] M. R.-Reyes, K. K. Kim, and D. L. Carrolla, “High-efficiency photovoltaic devices based on annealed poly(3-hexylthiophene) and 1-(3-methoxycarbonyl)-propyl-1- phenyl- (6 , 6) C 61 blends”, Appl. Phys. Lett., **87**, 083506-1-083506-3 (2005).

[63] S. M. Bayliss, S. Heutz, G. Rumbles, and T.S. Jones, “Thin film properties and surface morphology of metal free phthalocyanine films grown by organic molecular beam deposition”, Phys. Chem. Chem. Phys., **1** 3673-3676 (1999).

[64] K. Fukumura, T. Hori, T. Masuda, Q.-D. Dao, A. Fujii, Y. Shimizu, and M. Ozaki, “Solvent Effects on Solution-Processable Bulk Heterojunction Organic Solar Cells Utilizing 1,4,8,11,15,18,22,25-Octahexylphthalocyanine”, Jpn. J. Appl. Phys., **52**, 05DB02-01-05DB02-05 (2013).

[65] J. Wiedersich, J. Perlich, S. V. Roth, and P. M.-Buschbaum, “Solvent-induced morphology in polymer-based systems for organic photovoltaics”, Adv. Funct. Mater., **21**, 3382–3391 (2011).

[66] Q.-D. Dao, T. Hori, K. Fukumura, T. Masuda, T. Kamikado, A. Fujii, Y. Shimizu, and M. Ozaki, "Efficiency enhancement in mesogenic - phthalocyanine - based solar cells with processing additives", Appl. Phys. Lett., **101**, 263301-01-263301-03 (2012).

[67] Q.-D. Dao, T. Hori, K. Fukumura, T. Masuda, T. Kamikado, A. Fujii, Y. Shimizu, and M. Ozaki, "Effects of processing additives on nanoscale phase Separation, crystallization and photovoltaic performance of solar cells based on mesogenic phthalocyanine", Org. Electron., **14**, 2628-2634 (2013).

[68] [68] M. M. Wienk, J. M. Kroon, W. J. H. Verhees, J. Knol, J. C. Hummelen, P. A. V. Hal, and R. A. J. Janssen," Efficient methano[70]fullerene/MDMO-PPV bulk heterojunction photovoltaic cells", Angew. Chem. Int. Ed., **42**, 3371-3375 (2003)

[69] J. W. Arbogast and C. S. Foote, "Photophysical properties of C_{70}" J. Am. Chem. Soc., **113**, 8886-8889 (1991).

[70] Q.-D. Dao, H. Fukui, S. H. Lee, M. Ohmori, T. Kumada, A. Fujii, Y. Shimizu, and M. Ozaki, "Improvement of photovoltaic performance of octahexylphthalocyanine-based bulk-heterojunction solar cells using various fullerene derivatives", Trans. Mat. Res. Soc. Japan, **38[3]** 463-466 (2013).

[71] T. Masuda, T. Hori, K. Fukumura, T. Hayashi, Dao Q. D., H. Yoshida, A. Fujii, Y. Shimizu, and M. Ozaki, "Acceptor material dependence of photovoltaic properties in bulk heterojunction organic thin film solar cell utilizing soluble octahexylphthalocyanine", IEEJ Trans. EIS, **132**, (2012)1727.

[72] V. D. Mihailetchi, P. W. M. Blom, J. C. Hummelen, and M. T Rispens, "Cathode dependence of the open-circuit voltage of polymer:fullerene bulk heterojunction solar cells", J. Appl. Phys., **94**, 6849-6854 (2003).

[73] S. Yamato, A. Orimo, H. Ohkita, H. Benten, and S. Ito, "Molecular Understanding of the Open-Circuit Voltage of Polymer: Fullerene Solar Cells", Adv. Energy Mater., **2**, 229-237, (2012).

[74] M. Lenes, G. A. H. Wetzelaer, F. B. Kooistra, S. C. Veenstra, J. C. Hummelen and P. W. M. Blom: "Fullerene bisadducts for enhanced open-circuit voltages and efficiencies in polymer solar cells", Adv. Mater., **20**, 2116-2119 (2008).

[75] J. J. M. Halls, J. Cornil, D. A. dos Santos, R. Silbey, D.-H. Hwang, A. B. Holmes, J. L. Bredas, and R. H. Friend, "Charge- and energy-transfer processes at polymer/polymer interfaces: A joint experimental and theoretical study", Phys. Rev. B, **60**, 5721-5727 (1999).

[76] H. Iino and J. Hanna, "Ambipolar charge carrier transport in liquid crystals", Opto-Electron.

Rev., 2005, 13, 295.

[77] Y. Shimizu, K. Oikawa, K. Nakayama, and D. Guillond, “Mesophase semiconductors in field effect transistors”, J. Mater. Chem., **17**, 4223–4229 (2007)

[78] D. Adam, P. Schuhmacher, J. Simmerer, L. Haussling, K. Siemensmeyer, K. H. Etzbach, H. Ringsdorf and D. Haarer, ”Fast photoconduction in the highly ordered columnar phase of a discotic liquid crystal”, Nature, **371**, 141-143 (1994).

[79] H. Bassler, “Charge Transport in Disordered Organic Photoconductors”, Phys. Status Solidi B, **175**, 15-56, (1993).

[80] H. Iino, Y. Takayashiki, J. Hanna, and R. J. Bushby, “Fast ambipolar carrier transport and easy homeotropic alignment in a metal-free phthalocyanine derivative”, Jpn. J. Appl. Phys., **44**, L1310-L1312 (2005).

[81] H. Iino, J. Hanna, R. J. Bushby, B. Movaghar, B. J. Whitaker, and M. J. Cook, “Very high time-of-flight mobility in the columnar phases of a discotic liquid crystal”, Appl. Phys. Lett., **87**, 132102-01-132102-03 (2005).

[82] P. Weber, D. Guillon, and A. Skoulios, “Hexagonal columnar mesophases from phthalocyanine upright and tilted intracolumnar molecular stacking, herringbone and rotationally disordered columnar packing”, Liq. Cryst., **9**, 369-382 (1991).

[83] A. S. Cherodian,; A. N. Davies, R. M. Richardson, M. J. Cook, N. B. McKeown, A. J. Thomson, J. Feijoo, and G. Ungar, “Mesogenic behaviour of some 1,4,8,11,15,18,22,25-Octaalkylphthalocyanine”, Mol. Cryst. Liq. Cryst., **196**, 103-114 (1991)

[84] Q.-D. Dao, T. Saito, S. Nakano, H. Fukui, T. Kamikado, A. Fujii, Y. Shimizu, and M. Ozaki, “Alkyl Substituent Length Dependence of Octaalkylphthalocyanine Bulk Heterojunction Solar Cells”, Appl. Phys. Express, **6**, 122301-01-122301-04 (2013).

[85] A. Kumar, H.-H. Liao, and Y. Yang, “Hole mobility in optimized organic photovoltaic blend films obtained using extraction current transients”, Org. Electron. **10**, (2009) 1615-1620.

[86] C.J. Brabec, N.S. Sariciftci, and J.C. Hummelen, “Plastic solar cells”, Adv. Funct. Mater., **11**, 15-26 (2001).

[87] H. Spanggaard and F.C. Krebs, “A brief history of the development of organic and polymeric photovoltaics”, Sol. Energy Mater. Sol. Cells, **83**, 125-146 (2004).

[88] K.M. Coakley and M.D. McGehee, “Conjugated polymer photovoltaic cells”, Chem. Mater., **16**, 4533-4542 (2004).

[89] S. Gunes, H. Neugebauer, and N.S. Sariciftci, “Conjugated polymer-based organic solar cells”, Chem. Rev., **107**, 1324-1338 (2007).

[90] C. Winder and N.S. Sariciftci, “Low bandgap polymers for photon harvesting in bulk heterojunction solar cells”, J. Mater. Chem., 14, 1077-1086 (2004).

[91] E. Bundgaard and F.C. Krebs, “Low band gap polymers for organic photovoltaics”, Sol. Energy Mater. Sol. Cells, **91**, 954-985 (2007).

[92] B.P. Rand, J. Genoe, P. Heremans, and J. Poortmans, “Solar cells utilizing small molecular weight organic semiconductors”, Prog. Photovolt. Res. Appl., **15**, 659-676 (2007).

[93] M. Jorgensen, K. Norrman, and F. C. Krebs, “Stability/degradation of polymer solar cells”, Sol. Energy Mater. Sol. Cells, **92**, 686-714 (2008)

[94] C. J. Brabec, “Organic photovoltaics:technology and market”, Sol. Energy Mater. Sol. Cells, **83**, 273-292 (2004).

[95] P. Qin, G. Fang, Q. He, N. Sun, X. Fan, Q. Zheng, F. Chen, J. Wan, and X. Zhao, “Nitrogen doped amorphous chromium oxide: Stability improvement and application for the hole-transporting layer of organic solar cells”, Sol. Energy Mater. Sol. Cells, **95**, 1005-1010 (2011).

[96] K. Kawano and C. Adachi, “Reduced initial degradation of bulk heterojunction organic solar cells by incorporation of stacked fullerene and lithium fluoride interlayers”, Appl. Phys. Lett., **96**, 053307-01-053307-03 (2010).

[97] Y. Alfredsson, B. Brena, K. Nilson, J. Ahlund, L. Kjeldgaard, M. Nyberg, Y. Luo, N. Martensson, A. Sandell, C. Puglia, and H. Siegbahn, “Electronic structure of a vapor-deposited metal-free phthalocyanine thin film”, J. Chem. Phys., **122**, 214723-1-214723-6 (2005).

[98] Y. Niwa, H. Kobayashi, and T. Tsuchiya, “X-ray photoelectron spectroscopy of tetraphenylporphin and phthalocyanine”, J. Chem. Phys., **60**, 799-807 (1974).

[99] C. Y. Nam, D. Su, and C. T. Black, “High-performance air-processed polymer–fullerene bulk heterojunction solar cells”, Adv. Funct. Mater., **19**, 3552-3559 (2009).

[100] M. Logdlund and J. L. Bredas, “Theoretical studies of the interaction between aluminum and poly(p-phenylenevinylene) and derivatives”, J. Chem. Phys., **101**, 4357-4364 (1994).

[101] C. J. Brabec, S. E. Shaheen, C. Winder, N. S. Sariciftci, and P. Denk, “Effect of LiF/metal electrodes on the performance of plastic solar cells”, Appl. Phys. Lett., **80**, 1288-01-1288-02 (2002).

Achievement

I. Publications

1. T. Masuda, T. Hori, K. Fukumura, T. Hayashi, **Q.-D. Dao**, H. Yoshida, A. Fujii, Y. Shimizu, and M. Ozaki, "Acceptor material dependence of photovoltaic properties in bulk heterojunction organic thin film solar cell utilizing soluble octahexylphthalocyanine", IEEJ Trans. EIS, **132**, 1727-1732 (2012).
2. T. Masuda, T. Hori, K. Fukumura, Y. Miyake, **Q.-D. Dao**, T. Hayashi, T. Kamikado, H. Yoshida, A. Fujii, Y. Shimizu, and M. Ozaki, "Photovoltaic properties of 1,4,8,11,15,18,22,25-octaalkylphthalocyanine doped polymer bulk heterojunction solar cells", Jpn. J. Appl. Phys., **51**, 02BK15-1-02BK15-4 (2012).
3. **Q.-D. Dao**, T. Hori, K. Fukumura, T. Masuda, T. Kamikado, A. Fujii, Y. Shimizu, and M. Ozaki, "Efficiency enhancement in mesogenic - phthalocyanine - based solar cells with processing additives", Appl. Phys. Lett., **101**, 263301-01-263301-03 (2012).
4. **Q.-D. Dao**, T. Hori, T. Masuda, K. Fukumura, T. Kamikado, F. Nekelson, A. Fujii, Y. Shimizu, and M. Ozaki, "Mechanism of degradation and improvement of stability on mesogenic-phthalocyanine-based bulk heterojunction solar cell", Jpn. J. Appl. Phys., **52**, 012301-1-012301-5 (2013).
5. K. Fukumura, T. Hori, T. Masuda, **Q.-D. Dao**, A. Fujii, Y. Shimizu, and M. Ozaki, "Solvent Effects on Solution-Processable Bulk Heterojunction Organic Solar Cells Utilizing 1,4,8,11,15,18,22,25-Octahexylphthalocyanine", Jpn. J. Appl. Phys., **52**, 05DB02-1-05DB02-5 (2013).
6. **Q.-D. Dao**, H. Fukui, S. H. Lee, M. Ohmori, T. Kumada, A. Fujii, Y. Shimizu, and M. Ozaki, "Improvement of photovoltaic performance of octahexylphthalocyanine-based bulk-heterojunction solar cells using various fullerene derivatives", Trans. Mat. Res. Soc. Japan, **38[3]**, 463-466 (2013).
7. **Q.-D. Dao**, Tetsuro Hori, Kaoru Fukumura, Tetsuya Masuda, Toshiya Kamikado, Akihiko Fujii, Yo Shimizu, Masanori Ozaki, "Effects of processing additives on nanoscale phase Separation, crystallization and photovoltaic performance of solar cells based on mesogenic phthalocyanine", Org. Electron., **14**, 2628-2634 (2013).
8. **Q.-D. Dao**, Takashi Saito, Shohei Nakano, Hitoshi Fukui, Toshiya Kamikado, Akihiko Fujii,

Yo Shimizu, and Masanori Ozaki, "Alkyl Substituent Length Dependence of Octaalkylphthalocyanine Bulk Heterojunction Solar Cells", Appl. Phys. Express, **6**, 122301-01-122301-04 (2013).

9. **Q.-D. Dao**, T. Kumada, H. Fukui, M. Ohmori, A. Fujii, Y. Shimizu and M. Ozaki, "Blend Ratio Dependence of Photovoltaic properties in Octahexylphthalocyanine-based Small Molecule Solar Cell", **To be published in Jpn. J. Appl. Phys.**.
10. M. Ohmori, H. Fukui, **Q.-D. Dao**, T. Kumada, A. Fujii, Y. Shimizu, and M. Ozaki, "Annealing Effect in Bulk Heterojunction Organic Solar Cells Utilizing Liquid Crystalline Phthalocyanine", **To be published in Jpn. J. Appl. Phys.**.
11. H. Fukui, S. Nakano, T. Uno, **Q.-D. Dao**, T. Saito, A. Fujii, Y. Shimizu, and M. Ozaki, "Miscibility in Binary Blends of Non-Peripheral Alkylphthalocyanines and Their Application for Bulk-Heterojunction Solar Cells", **To be published in Org. Electron.**.

II. International Conferences

1. J. Sakamoto, S. Tominaga, T. Hori, **Q.-D. Dao**, T. Masuda, K. Fukumura, T. Hayashi, H. Yoshida, A. Fujii, Y. Shimizu, and M. Ozaki, "Solution processable organic solar cell based on bulk heterojunction utilizing phthalocyanine and fullerene" 6th Photonics Center Symposium "Nanophotonics in Asia 2011", Shima Kanko Hotel The Classic, Shima, Mie, Japan, September 20-21, 2011.
2. T. Masuda, T. Hori, N. Fukuoka, **Q.-D. Dao**, T. Hayashi, T. Kamikado, H. Yoshida, A. Fujii, Y. Shimizu, and M. Ozaki, "Doping Effects of Liquid Crystalline Phthalocyanine in Bulk Heterojunction Polymer Solar Cells", 2011 International Conference on Solid State Devices and Materials (SSDM 2011), Aichi Industry & Labor Center, Nagoya, Aichi, Japan, September 28-30, 2011.
3. T. Hori, T. Masuda, N. Fukuoka, Y. Miyake, **Q.-D. Dao**, T. Hayashi, T. Kamikado, H. Yoshida, A. Fujii, Y. Shimizu, and M. Ozaki, "Doping Effects of 1,4,8,11,15,18,22,25-Octahexylphthalocyaninein Bulk Heterojunction Polymer Solar Cells", International Symposium on Functional π-Electron Systems, Beijing Friendship Hotel, Beijing, China, October 13-17, 2011.
4. M. Ozaki, T. Hori, T. Masuda, T. Hayashi, **Q.-D. Dao**, Y. Miyake, H. Yoshida, A. Fujii, and Y. Shimizu, "High Ambipolar Carrier Mobility of Discotic Mesogenic Molecules and Its Application for Solar Cells", International Symposium on Functional π-Electron Systems (FPi-10), Beijing Friendship Hotel, Beijing, China, October 13-17, 2011 (Oral).

5. A. Fujii, T. Hori, T. Masuda, **Q.-D. Dao**, T. Hayashi, H. Yoshida, Y. Shimizu, and M. Ozaki, "Bulk Hetero-Junction Solar Cells Utilizing Liquid Crystalline Phthalocyanine Derivatives", 2011 Materials Research Society Fall Meeting (2011 MRS Fall Meeting), Hynes Convention Center, Boston, MA, USA, November 28-December 2, 2011 (Oral).
6. A. Fujii, T. Hori, A. Semba, J. Sakamoto, Y. Inoue, W. Yonan, J. Kim, **Q.-D. Dao**, Y. Ogawa, T. Masuda, T. Hayashi, H. Kubo, H. Yoshida, F. Ishikawa, K. Morita, M. Abe, M. Ozaki, J. Sakai, H. Rahmat, W. Feng, M. Shkunov, and Y. Shimizu, "Photovoltaic Properties in Interpenetrating Heterojunction Organic Solar Cells Utilizing Metal Oxide Charge Transport Buffer Layers", 3rdGlobal COE International Symposium Electronic Devices Innovation (EDIS2011), Senri Life Science Center, Toyonaka, Osaka, Japan, December 16-17, 2011.
7. A. Fujii, K. Fukumura, T. Hori, **Q.-D. Dao**, T. Masuda, T. Hayashi, H. Yoshida, F. Nekelson, Y. Shimizu, and M. Ozaki, "Organic Thin-Film Solar Cells Utilizing Discotic Liquid Crystalline Phthalocyanine", 2012 Taiwan-Japan Nanophotonics and Plasmonic Metamaterials Workshop, National Taiwan University, Taipei, Taiwan, January 11-12, 2012 (Oral).
8. K. Fukumura, T. Hori, T. Masuda, **Q.-D. Dao**, T. Hayashi, T. Kamikado, F. Nekelson, H. Yoshida, A. Fujii, Y. Shimizu, and M. Ozaki, "Photovoltaic Properties of Organic Solar Cells Utilizing Liquid Crystalline Phthalocyanine Derivative and Its Application for Tandem Solar Cell", 2012 Taiwan-Japan Nanophotonics and Plasmonic Metamaterials Workshop, National Taiwan University, Taipei, Taiwan, January11-12, 2012.
9. **Q.-D. Dao**, T. Hori, T. Masuda, K. Fukumura, T. Hayashi, T. Kamikado, F. Nekelson, H. Yoshida, A. Fujii, Y. Shimuzu, and M. Ozaki, "Mesogenic phthalocyanine derivative based organic solar cell" International symposium on nanophotonics 2012, Beijing, China, 12-14, Feb. 2012.
10. T. Hori, T. Masuda, K. Fukumura, **Q.-D. Dao**, T. Hayashi, T. Kamikado, F. Nekelson, H. Yoshida, A. Fujii, Y. Shimizu, and M. Ozaki, "Non-Peripheral Octaalkylphthalocyanine Doping Effects In Popymer Bulk Heterojunction Solar Cells", International Conference on Science and Technology of Synthetic Metals (ICSM2012), The Hyatt Regency Atlanta, Atlanta, Georgia, USA, July 8-13, 2012.
11. **Q.-D. Dao**, T. Hori, T. Masuda, K. Fukumura, T. Hayashi, T. Kamikado, F. Nekelson, H. Yoshida, A. Fujii, Y. Shimuzu, and M. Ozaki, "High stability of mesogenic phthalocyanine based bulk heterojunction solar cells" International conference on science and technology of synthetic metals (ICSM). Atlanta, Georgia, America 8-13, July, 2012.
12. A. Fujii, T. Hori, **Q.-D. Dao**, T. Masuda, K. Fukumura, T. Hayashi, H. Yoshida, F. Nekelson,

Y. Shimizu, and M. Ozaki, "Solution-Processable Bulk Hetero-Junction Solar Cells Utilizing Discotic Liquid Crystalline Phthalocyanine" International Conference on Science and Technology of Synthetic Metals (ICSM2012), The Hyatt Regency Atlanta, Atlanta, Georgia, USA, July 8-13, 2012.

13. K. Fukumura, T. Hori, T. Masuda, **Q.-D. Dao**, T. Hayashi, T. Kamikado, F. Nekelson, H. Yoshida, A. Fujii, Y. Shimizu, and M. Ozaki, "Solvent Effects on Fabrication of Soluble Phthalocyanine Derivative Thin Films and Its Applications to Organic Solar Cell", The 2012 International Conference on Flexible and Printed Electronics (ICFPE2012), Yasuda Auditorium, Hongo Campus, The University of Tokyo, Tokyo, Japan, September 6-8, 2012.
14. K. Fukumura, T. Hori, T. Masuda, **Q.-D. Dao**, T. Kamikado, H. Yoshida, A. Fujii, Y. Shimizu, and M. Ozaki, "Solvent Dependence on Photovoltaic Properties of Bulk Heterojunction Organic Solar Cells Utilizing Soluble Phthalocyanine Derivative", Asia Student Photonics Conference 2012, Photonics Center, Osaka University, Osaka, Japan, September 15-16, 2012.
15. K. Fukumura, T. Hori, T. Masuda, **Q.-D. Dao**, T. Kamikado, H. Yoshida, A. Fujii, Y. Shimizu, and M. Ozaki, "Small Molecule Bulk Heterojunction Organic Solar Cells Based on Liquid Crystalline Phthalocyanine", Seventh Photonics Center Symposium "Nanophotonics in Asia 2012", Kanazawa Excel Hotel Tokyu, Ishikawa, Japan, September 18-19, 2012.
16. **Q.-D. Dao**, T. Hori, T. Masuda, K. Fukumura, T. Hayashi, T. Kamikado, F. Nekelson, H. Yoshida, A. Fujii, Y. Shimuzu, and M. Ozaki, "Effects of Counter Electrodes on Stability of Phthalocyanine Based Bulk Heterojunction Solar Cell", IUMRS-International conference on electronic materials (IUMRS-ICEM 2012) 23-28., Sep.2012, Yokohama, Japan (Oral).
17. **Q.-D. Dao**, T. Hori, T. Masuda, K. Fukumura, T. Hayashi, T. Kamikado, H. Yoshida, A. Fujii, Y. Shimuzu, and M. Ozaki, "High efficient solution processable bulk heterojunction solar cells based on mesogenic phthalocyanine", The 6th international workshop on Advanced materials science and nanotechnology (IWAMSN 2012) Halong, Vietnam 30, Oct. - 02, Nov. 2012 (Oral).
18. **Q.-D. Dao**, T. Hori, T. Masuda, K. Fukumura, T. Hayashi, T. Kamikado, A. Fujii, Y. Shimuzu, and M. Ozaki, "Effects of Processing-additive Solvents on Photovoltaic Efficiency of Mesogenic-phthalocyanine Solar Cells", 7th international conference on molecular electronics and bioelectronics (M&BE7) Fukuoka, Japan 17-19. Mar., 2013. (**Outstanding Student Poster Award**)
19. **Q.-D. Dao**, H. Fukui, S. H. Lee, M. Ohmori, T. Kumada, A. Fujii, Y. Shimizu, and M. Ozaki, "Improvement of Photovoltaic Performance of Octahexylphthalocyanine Based Bulk

Heterojunction Solar Cells Using Processing Additives", JSAP-MRS Joint Symposia, Doshisha University, Japan, 16-20. Sep., 2013.

III. Domestic Conferences

1. **Q.-D. Dao**, T. Hori, T. Masuda, K. Fukumura, T. Kamikado, A. Fujii, Y. Shimuzu, and M. Ozaki, "Stability of Mesogenic-Phthalocyanine-Based Bulk Heterojunction Solar Cell", 応用物理学会春季学術講演会, Kanagawa institute of technology, 27-30. Mar., 2013.
2. **Q.-D. Dao**, T. Hori, T. Masuda, K. Fukumura, T. Kamikado, A. Fujii, Y. Shimuzu, and M. Ozaki, "Effects of Solvent Mixtures on Nanoscale Phase Separation and Photovoltaic Efficiency of Mesogenic - Phthalocyanine - Based Bulk Heterojunction Solar Cell", 応用物理学会春季学術講演会, Kanagawa institute of technology, 27-30. Mar., 2013.
3. **Q.-D. Dao**, M. Ohmori, T. Kumada, A. Fujii, Y. Shimizu, and M. Ozaki, "Efficiency Enhancement in Mesogenic-Phthalocyanine-Based Bulk Heterojunction Solar Cell By Using Solvent Mixtures", 応用物理学会秋季学術講演会, Doshisha University, Japan, 16-20. Sep., 2013 (Oral).
4. **Q.-D. Dao**, H. Fukui, S. Nakano, T. Kumada. T. Kamikado, A. Fujii, Y. Shimizu, and M. Ozaki, "Dependence of Photovoltaic Performance of Mesogenic-Phthalocyanine-Based Bulk Heterojunction Solar Cell on Alkyl Substituent Length", 応用物理学会秋季学術講演会, Doshisha University, Japan, 16-20. Sep., 2013 (Oral).